

**UCLA**

**UCLA Electronic Theses and Dissertations**

**Title**

High Efficiency Electron-Laser Interactions in Tapered Helical Undulators

**Permalink**

<https://escholarship.org/uc/item/4hf028sr>

**Author**

Duris, Joseph

**Publication Date**

2015

Peer reviewed|Thesis/dissertation

UNIVERSITY OF CALIFORNIA

Los Angeles

**High Efficiency Electron-Laser Interactions in  
Tapered Helical Undulators**

A dissertation submitted in partial satisfaction  
of the requirements for the degree  
Doctor of Philosophy in Physics

by

**Joseph Patrick Duris**

2015

© Copyright by  
Joseph Patrick Duris  
2015

ABSTRACT OF THE DISSERTATION

# High Efficiency Electron-Laser Interactions in Tapered Helical Undulators

by

**Joseph Patrick Duris**

Doctor of Philosophy in Physics

University of California, Los Angeles, 2015

Professor Pietro Musumeci, Chair

Efficient coupling of relativistic electron beams with high power radiation lies at the heart of advanced accelerator and light source research and development. The inverse free electron laser is a stable accelerator capable of harnessing very high intensity laser electric fields to efficiently transfer large powers from lasers to electron beams.

In this dissertation, we first present the theoretical framework to describe the interaction, and then apply our improved understanding of the IFEL to the design and numerical study of meter-long, GeV IFELs for compact light sources. The central experimental work of the dissertation is the UCLA BNL helical inverse free electron laser experiment at the Accelerator Test Facility in Brookhaven National Laboratory, which used a strongly tapered 54 cm long, helical, permanent magnet undulator and a several hundred GW CO<sub>2</sub> laser to accelerate electrons from 52 to 106 MeV, setting new records for inverse free electron laser energy gain (54 MeV) and average accelerating gradient (100 MeV/m). The undulator design and fabrication as well as experimental diagnostics are presented. In order to improve the stability and quality of the accelerated electron beam, we redesigned the undulator for a slightly reduced output energy by modifying the magnet gap throughout the undulator, and we used this modified undulator to demonstrated

capture of  $>25\%$  of the injected beam without prebunching.

In the study of heavily loaded GeV inverse free electron lasers, we show that a majority of the power may be transferred from a laser to the accelerated electron beam. Reversing the process to decelerate high power electron beams, a mechanism we refer to as tapering enhanced stimulated superradiant amplification, offers a clear path to high power light sources. We present studies of radiation production for a wide range of wavelengths (10  $\mu\text{m}$ , 13 nm, and 0.3 nm) using this method and discuss the design for a deceleration experiment using the same undulator used for acceleration in this experiment. By accounting for the evolving radiation field in the design of the undulator tapering, a large fraction of energy may be transferred between the electrons and laser, enabling compact, high-current GeV accelerators and various wavelength light-sources of unprecedented peak powers.

The dissertation of Joseph Patrick Duris is approved.

Robert N Candler

James Rosenzweig

Pietro Musumeci, Committee Chair

University of California, Los Angeles

2015

*For my parents ...*

# TABLE OF CONTENTS

<b>1</b>	<b>Introduction</b>	<b>1</b>
1.1	Inverse free electron laser acceleration	2
1.2	Outline of this dissertation	7
<b>2</b>	<b>IFEL theory</b>	<b>9</b>
2.1	Transverse dynamics	10
2.1.1	Betatron motion	12
2.1.2	Transverse emittance	15
2.2	Accelerator equations	16
2.2.1	Ponderomotive acceleration	17
2.2.2	Ponderomotive phase evolution	19
2.2.3	Acceleration with a Gaussian laser	21
2.3	Longitudinal dynamics	23
2.3.1	Regions of stability	24
2.3.2	Capture estimates for a uniform current beam	27
2.3.3	Synchrotron oscillations and bunching	28
2.4	Undulator tapering design	32
2.5	Resonant phase variation for optimal tapering	34
2.5.1	Constant bucket size tapering	35
2.6	Diffraction effects	37
<b>3</b>	<b>Numerical studies</b>	<b>40</b>
3.1	Meter-long GeV accelerator	41

3.2	Taper design . . . . .	43
3.3	1D simulations with constant resonant phase . . . . .	48
3.3.1	Capture estimates . . . . .	48
3.3.2	Prebunching to improve capture . . . . .	51
3.4	1D simulations with constant action tapering . . . . .	52
3.4.1	Adiabatic capture: low initial energy . . . . .	55
3.4.2	Adiabatic capture: undulator field ramp . . . . .	56
3.4.3	Adiabatic capture: laser field ramp . . . . .	59
3.5	Beam loading . . . . .	62
<b>4</b>	<b>Experimental design and setup . . . . .</b>	<b>69</b>
4.1	Design parameters . . . . .	70
4.2	Tapered helical undulator . . . . .	73
4.2.1	High gradient taper design . . . . .	73
4.2.2	High capture taper design . . . . .	75
4.2.3	Mechanical design . . . . .	77
4.2.4	Construction . . . . .	81
4.2.5	Magnetic field modeling . . . . .	84
4.2.6	Geometrical measurements and initial tune . . . . .	86
4.2.7	1D field measurement setup . . . . .	87
4.2.8	Undulator tuning . . . . .	89
4.2.9	3D magnetic field scans . . . . .	91
4.3	Expected performance . . . . .	94
4.3.1	High gradient taper design tolerances . . . . .	98
4.3.2	Performance estimates for high capture taper . . . . .	101

4.4	Prebuncher design for better trapping . . . . .	102
4.5	ATF Linac and electron beam tune . . . . .	108
4.6	Energy spectrometer . . . . .	110
4.7	CO <sub>2</sub> laser . . . . .	113
4.7.1	Laser transport . . . . .	113
4.7.2	Laser focusing . . . . .	116
4.7.3	Temporal laser pulse diagnostics . . . . .	119
4.7.4	Laser energy measurements . . . . .	122
<b>5</b>	<b>Experimental results . . . . .</b>	<b>125</b>
5.1	Synchronization . . . . .	125
5.2	Polarization . . . . .	130
5.2.1	Elliptical IFEL acceleration . . . . .	130
5.2.2	Polarization scan . . . . .	132
5.3	High gradient acceleration . . . . .	134
5.4	High capture acceleration . . . . .	139
5.5	Emittance measurement . . . . .	143
<b>6</b>	<b>Tapering enhanced stimulated superradiant amplification . . . . .</b>	<b>146</b>
6.1	Low gain regime . . . . .	148
6.2	Low gain TESSA experiment at ATF . . . . .	149
6.2.1	Experimental design . . . . .	150
6.2.2	Simulations . . . . .	154
6.2.3	Experimental outlook . . . . .	154
6.3	High gain regime . . . . .	156

6.4	High power EUV light source . . . . .	159
6.5	X-ray FEL afterburner . . . . .	161
6.5.1	Sideband suppression . . . . .	163
<b>7</b>	<b>Conclusions . . . . .</b>	<b>165</b>
<b>A</b>	<b>Laser accelerator energy fluctuations . . . . .</b>	<b>168</b>
<b>B</b>	<b>IFEL simulation tools . . . . .</b>	<b>172</b>
<b>C</b>	<b>Laser induced emittance growth . . . . .</b>	<b>175</b>
	<b>References . . . . .</b>	<b>180</b>

## LIST OF FIGURES

1.1	IFEL force diagram . . . . .	6
2.1	IFEL Hamiltonian cross sections . . . . .	25
2.2	Ponderomotive bucket width and area . . . . .	28
2.3	Diagram illustrating synchrotron rotations and bunching . . . . .	30
2.4	Adiabatic capture diagram . . . . .	31
2.5	IFEL gradient optimization for Gaussian beam focusing parameters	38
3.1	The average accelerating gradient and final energy of tapering solutions for different initial energies are shown together. . . . .	46
3.2	Undulator parameters for a GeV IFEL accelerator with constant $-\pi/4$ resonant phase . . . . .	47
3.3	Simulations for a GeV IFEL with constant $-\pi/4$ resonant phase .	50
3.4	Simulations for various GeV IFEL accelerators with constant actions	53
3.5	Constant bucket area undulator tapers vs input energy for initial resonant phase $\psi_{r,0} = 0$ and vs different initial resonant phases for initial resonant energy 100 MeV . . . . .	55
3.6	Undulator taper design for an accelerator with $B_r$ assisted mildly diabatic capture. . . . .	57
3.7	Phase space evolution for the residual magnetization tapering assisted capture and acceleration . . . . .	58
3.8	Undulator taper design for an accelerator with slippage assisted mildly diabatic capture . . . . .	61
3.9	Phase space evolution for the slippage assisted capture and acceleration . . . . .	62

3.10	Output e-beam and laser parameters versus input peak current for an uncompensated undulator. . . . .	64
3.11	Output e-beam and laser parameters versus input peak current for a changing laser power compensated undulator taper design. . . .	65
3.12	A dense electron beam erodes a hole in the laser intensity as it transfers power. . . . .	66
3.13	Output e-beam and laser parameters versus input e-beam rms spot size, scaling the emittance to keep the divergence constant, for an standard, uncompensated undulator taper design. . . . .	67
4.1	The Rubicon design tapering is the solution of the tapering equations and the design parameters listed in Table 4.1. . . . .	74
4.2	The undulator parameters and dynamical quantities for the high capture taper design . . . . .	77
4.3	Engineering model of the partially assembled undulator body. . .	79
4.4	Engineering model of the undulator rails with magnets. . . . .	79
4.5	Engineering model of the undulator magnet holders and tuning plates assembly. . . . .	80
4.6	Magnet model with dimensions in mm. . . . .	81
4.7	Undulator geometry for the Radia model. . . . .	85
4.8	Geometrical measurements determining the initial magnet tune .	88
4.9	Undulator field scan setup. . . . .	88
4.10	A cross sectional view of the undulator showing gap adjustment .	90
4.11	Measured transverse magnetic fields and calculated transverse trajectories (assuming a constant 50 MeV energy) for the high gradient undulator tune . . . . .	90

4.12	Transverse scan of the vertical component of the magnetic field measured at a peak within the undulator. . . . .	91
4.13	Design and measured peak values of the final tuned field, and positions of the saddle points measured with the 3D field scan . . . .	92
4.14	Measured and Radia field maps for the first 5 peaks. . . . .	93
4.15	IFEL output phase space and electron spectrum for 500 GW peak laser power. . . . .	96
4.16	Fraction of accelerated particles vs position of waist relative to the undulator's midpoint . . . . .	100
4.17	High capture simulation with 18 TW/cm <sup>2</sup> focal intensity laser. . .	101
4.18	Maximum particle energy and fraction of beam with energy greater than 90 MeV as a function of input laser focal intensity . . . . .	102
4.19	Two views of the prebuncher module . . . . .	104
4.20	3D simulations of the average magnetic field felt by the particles and the transverse position of the beam as it traverses through the buncher and helical undulator without laser . . . . .	106
4.21	Longitudinal phase space shown at positions just after the prebuncher and accelerator . . . . .	107
4.22	Laser peak power sensitivity scans show the fraction of injected electrons accelerated to full power, the mean energy of the accelerated fraction of electrons, and the rms energy spread . . . . .	107
4.23	3D model of the beam line with quadrupoles and undulator installed. . . . .	109
4.24	Twiss parameters for the experiment and estimated beta functions at various beam position monitors along the beam line . . . . .	110
4.25	Spectrometer layout and optics. . . . .	111

4.26	Shown above are the magnet field calibration and spectrometer energy calibration. . . . .	112
4.27	Diagnostics near the experiment for monitoring the pulse energy and transverse profile. . . . .	114
4.28	Laser pulse energy calibration and transverse profile monitoring. . . . .	115
4.29	Clear apertures, laser waist, and peak laser fluence along the beam-line for various laser focal properties . . . . .	116
4.30	Lens to waist focal distance vs thin lens designed focal length . . . . .	117
4.31	Waist scan showing the $1/e$ spot size evolution with the undulator midpoint at the origin. . . . .	118
4.32	Measured spectra for two amplified shots at different laser energies. . . . .	120
4.33	Fit bandwidth is plotted versus output pulse energy. . . . .	121
4.34	Streak camera images for two different shots. . . . .	122
4.35	Measured laser energy from the high gradient run measured near the main amplifier and from the high capture run measured in the experimental hall . . . . .	123
4.36	Localized damage to the final focusing lens and NaCl vacuum window acquired during the first, high capture run . . . . .	123
5.1	Oscilloscope showing signals from the strip line and photo diode . . . . .	126
5.2	Plot showing the Ge transmission and IFEL acceleration data versus laser delay. . . . .	127
5.3	Plots IFEL acceleration metrics (max and min energy changes) versus laser delay as well as corresponding acceleration vs laser energy correlation plots. . . . .	128

5.4	Polarization scan showing charge accelerated above 70 MeV versus quarter waveplate orientation. . . . .	132
5.5	Transverse scan showing the maximum normalized laser intensity estimator for the laser at different transverse positions and a binormal fit with the measured laser waist at the undulator's entrance. . . . .	136
5.6	Maximum measured and simulated output energy versus peak focal intensity . . . . .	137
5.7	Raw spectrometer images and calibrated spectrum with simulation for a shot without laser and one with the highest energy . . . . .	138
5.8	IFEL performance versus input electron energy. . . . .	139
5.9	Plot showing the spectra of all IFEL shots for one day during the high capture run. . . . .	140
5.10	Histogram of the energy of the peak charge density of the accelerated beam. . . . .	141
5.11	Raw electron spectrometer images for various shots and calibrated electron spectra for the first two shots for the high capture IFEL configuration . . . . .	142
5.12	Fits to electron beam rms widths for a section of beamline with a 6 m drift between two quadrupole triplets. . . . .	144
5.13	Quadrupole scans showing measured emittance and simulated emittance evolution for a matched and unmatched beam . . . . .	145
6.1	Schematic showing an implementation of a tapering enhanced stimulated superradiant amplifier . . . . .	147
6.2	Diagram of the beamline setup for the IFEL decelerator project at ATF. . . . .	151

6.3	Undulator design parameters for the low gain TESSA experiment at ATF . . . . .	153
6.4	Radiation power growth along the undulator . . . . .	154
6.5	The e-beam longitudinal phase space is shown at the exit of the undulator . . . . .	155
6.6	The transverse radiation profile is shown at the exit of the undulator	155
6.7	Results of GITS optimizations for a 1 GeV, 4 kA, prebunched e-beam lasing at 13.5 nm with a seed power of 5 GW from an upstream FEL . . . . .	160
6.8	GITS simulations for the case of an x-ray FEL afterburner with a 14.35 GeV, 4 kA unbunched electron beam and 5 MW seed laser with 3 Å wavelength. . . . .	163
C.1	Laser heater model and GPT simulations for three different beam waists: 100, 200, and 400 μm. . . . .	178

## LIST OF TABLES

3.1	GeV IFEL design parameters . . . . .	45
3.2	Injection thresholds for entrance positioned laser waist . . . . .	48
4.1	Experimental design parameters . . . . .	70
4.2	High gradient run undulator parameters . . . . .	74
4.3	High capture run experimental design parameters . . . . .	76
4.4	Undulator period lengths . . . . .	84
4.5	High gradient run simulation parameters . . . . .	95
4.6	High gradient run simulation results . . . . .	97
4.7	High gradient run parameter tolerances . . . . .	98
4.8	Laser waist scan results . . . . .	119
6.1	IFEL decelerator design parameters . . . . .	152
6.2	EUV and x-ray GITS simulation parameters . . . . .	161
A.1	Laser accelerator stability characteristics . . . . .	170
B.1	Capabilities of various IFEL simulation tools . . . . .	172

## ACKNOWLEDGMENTS

I owe a debt of gratitude to many people who helped me along the way up to this point.

First I would like to thank my adviser Pietro Musumeci who enthusiastically brought me in his group and provided me a chance to start working on projects and presenting at conferences at a time when I was considering leaving physics. Despite my mistakes (sometimes expensive), he has continued to entrust me with new projects and responsibilities to expand my horizons and has been a constant source of inspiration for new ideas.

I want to thank Prof. Rainer Wallny for his support in my first few years of grad school, especially during the month or two leading up to the comprehensive exam and for his support during my transition from high energy to accelerator physics.

None of the experimental work could have been done without the undulator which was designed by Pietro and Renkai, drawn up in SolidWorks by Mark Westfall, and parts made by the UCLA Physics Machine Shop. Harry Lockart in particular was an endless source of mechanical knowledge. Nor could our experiments have succeeded without the continued excellent work by all at ATF: Igor, Vitaly, Mikhail Fedurin, Mikhail Polyanskiy, Karl, Christina, Marcus, Paul, and Bob.

Much of the experimental work detailed in this dissertation was supported by DOE grant DE-FG02-92ER40693 and Defense Threat Reduction Agency award HDTRA1-10-1-0073.

I must also thank everyone at PBPL for all the helpful and interesting discussions and all the lunches, dinners, bbqs, and volleyball and bowling meetups. Josh McNeur first invited me to a PBPL bbq a year before I joined. Gerard Andonian and Gabe Marcus taught me a lot about Elegant and Genesis. Finn helped me

with undulators. Ago helped me understand FELs. Yusuke helped me learn the ropes at ATF and always had a spare when I broke something. Evan Threlkeld helped me tremendously with the undulator construction and later made the CAD designs for the prebuncher. Nick Sudar built and tuned the prebuncher and helped with the prebunched IFEL runs at ATF. Mark Westfall and Mike Liu introduced me to canyoneering in the San Gabriel Mountains. Oliver Williams made the lab's keggerator and rented the house in West Hampton for our many trips to BNL so that we didn't have to live in hotels for weeks at a time. I enjoyed many regular games of StarCraft 2 at the office with Cheyne, Josh Moody, Gabe, Gerard, Hoss, Andy Yakub, Andy Knyazik, Evan, Sean, and Long Ho and many games of foosball with Hoss, Long, Sean, Pietro, Gerard, Egor, Emma, Nick, Claudio, David, Ryan, Ivan, Sam, Schiller, and Oliver. I also have to thank Kristin, Brendan, Emma, Hoss, the many substitutes who lead our PBPL bowling team "Our talents lie elsewhere" to first place at the Bay Shore Lanes' Monday Night Fun Bowl league.

Finally, I would like to thank my friends and family for all the adventures and parties and scheduling them, when they could, around my frequent absences for experiments and conferences during the past several years.

## VITA

- 2006 Regents Scholar, University of California, Irvine
- 2007 RISE Fellowship, DAAD, Bonn, Germany
- 2008 B.S. in Physics (summa cum laude), UC Irvine
- 2008–2010 Graduate Student Researcher under Rainer Wallny, UCLA
- 2010 M.S. in Physics, University of California, Los Angeles
- 2012 Outstanding Teaching Assistant Award, Department of Physics and Astronomy, University of California, Los Angeles
- 2010–2015 Graduate Student Researcher under Pietro Musumeci, UCLA Particle Beam Physics Laboratory

## PUBLICATIONS

D. Asner, et al., The RD42 Collaboration, “Diamond pixel modules.” *NIM A*, 636, 1, S125-S129 (2011)

J. Duris, P. Musumeci, and R. K. Li. “Inverse free electron laser accelerator for advanced light sources.” *Phys. Rev. ST Accel. Beams* 15, 061301 (2012)

J. Duris, et al. “High energy gain inverse free electron laser experiment using a helical undulator.” In *Proc. AAC Workshop*, Austin, TX (2012)

J. Duris, R. K. Li, P. Musumeci, and E. Threlkeld, “Undulator commissioning for a high-energy-gain inverse free electron laser experiment.” In *Proc. I. Particle Accelerator Conf.*, New Orleans, LA, WEPPP036 (2012)

J. Duris, et al., “High capture low energy spread inverse free electron laser accelerator.” In *Proc. NA Part. Accel. Conf.*, Pasadena, CA, TUPMA16 (2013)

J. Duris, et al. “Helical inverse free electron laser accelerator for efficient production of high quality electron beams.” In *Proc. AAC Workshop*, San Jose, CA (2014).

J. Duris, et al. “High-quality electron beams from a helical inverse free-electron laser accelerator.” *Nat. Comm.* 5, 4928 (2014)

N. Sudar, P. Musumeci, and J. Duris. “IFEL driven mode locked free electron laser.” *J Phys B At Mol Opt Phys* 47, 234007 (2014)

N. Sudar, J. Duris, and P. Musumeci. “IFEL driven micro-electro-mechanical system free electron laser.” In *Proc. FEL Conf.*, Basel, CH, TUP045 (2014)

J. Duris, and P. Musumeci. “High efficiency lasing with a strongly tapered undulator.” In *Proc. FEL Conf.*, Basel, Switzerland, TUP042 (2014)

P. Musumeci, J. Duris, and A. Murokh. “Tapering enhanced stimulated superradiant amplification.” US Patent application number 61/982623 (2015)

J. Duris, A. Murokh, and P. Musumeci. “Tapering enhanced stimulated superradiant amplification.” *New J. Phys.*, 17, 063036 (2015)

# CHAPTER 1

## Introduction

Particle accelerators have enabled a myriad of scientific discoveries and provided tools for industry, medicine, and defense [1]. Scientific applications in particular have driven the advancement of accelerators to produce higher energies and currents, leading to  $10^4$  measurements of the properties of particle interactions upon which the standard model of physics was built according to the Particle Data Group [2].

Modern particle colliders employ accelerators built using radio frequency (RF) power sources [3, 4, 5, 6], however despite their successes, RF accelerators are cost limited as their sizes scale rapidly with energy. For linacs, field emission limits accelerating gradients to a fixed amount (typically around 50-100 MV/m) so that both energy output and power input scale with length. Rings circumvent this problem by periodically accelerating at modest gradients while bending the particles in a closed circle, yet the synchrotron radiation resulting from the particles' centripetal acceleration increases as the fourth power of the particle's Lorentz factor divided by the square of the ring's radius. Consequently, ever larger rings are required for increased particle energies to keep power requirements reasonable.

Although synchrotron radiation has hindered the synchrotron ring approach to high energies, it has become a useful tool in its own right [7], leading to the creation of third generation light sources based on undulators, periodic magnet arrays specially designed to produce synchrotron radiation at specific wavelengths. Later it was discovered that by allowing the radiation to modulate the electrons'

energies, the electrons begin to bunch, creating a temporal coherence which stimulates more radiation production in an unstable feedback loop [8]. This forms the basis of the free electron laser (FEL) interaction [9, 10] which is among the most efficient mechanisms of transferring energy from a relativistic electron beam to a radiation pulse, and as such forms the physical basis of the revolutionary successes of fourth generation coherent x-ray light sources [11, 12]. Coupling between transverse electromagnetic waves and relativistic electron motion is made possible in the FEL by the presence of the undulator magnetic field which bends the electron trajectories, enabling the energy exchange. Synchronous energy transfer is achieved if the electrons' oscillations fall behind laser wave fronts by an integer number of wavelengths for each undulation period (resonant condition). In FELs, the electrons on average lose energy to the electromagnetic wave as they propagate through the undulator field, resulting in a growing radiation field amplitude.

## 1.1 Inverse free electron laser acceleration

The same mechanism can be employed in reverse to enable laser-driven acceleration of particles by extracting energy from a high power laser to accelerate a relativistic electron beam at high gradients [13]. In order to achieve large energy gains in this case, the IFEL/FEL resonant condition can be maintained over meter-scale distances by appropriately tapering the undulator magnetic field and period. Since the wavelengths of the drive lasers are much shorter than those of RF power sources, electromagnetic energy may be focused to much smaller spot sizes with vastly larger electric fields over long distances without requiring a waveguide. Furthermore higher peak power can be achieved as laser pulse lengths can be in the ps and fs regime; consequently, gradients available in an IFEL accelerator may exceed GeV/m with current laser and undulator technologies.

The IFEL accelerator was initially considered for high energy physics colliders.

At that time, it was calculated that synchrotron losses in an IFEL accelerator significantly reduce accelerating gradients for energies approaching 100 GeV, limiting practically obtainable energies to a couple hundred GeV in 1 km [14]. Despite this limitation, IFEL remains a promising candidate for meter-scale, GeV-class accelerators [15, 16, 17] which could reduce costs for advanced light sources such as compact soft x-ray FELs and the production of  $\gamma$ -rays by inverse Compton scattering [18]. In the first part of this dissertation, we discuss methods for capturing and optimally accelerating an electron beam and then apply these to the conceptual design of a meter-long GeV IFEL accelerator.

Compared to other advanced accelerator schemes, the IFEL enjoys unique advantages. It does not require any medium (plasma or dielectric) or boundaries close to the interaction, allowing for efficient coupling as the energy from the laser is directly transferred into electron kinetic energy rather than dissipating in a medium. As a far-field vacuum acceleration scheme, nearly plane wave electromagnetic radiation can be used to accelerate particles, removing all issues related to small transverse acceptance or strong focusing in optical frequency or plasma-based accelerating structures. The transverse beam size can therefore be relatively large (many laser wavelengths across) which, in addition to the absence of nearby structures, strongly mitigates collective effects such as space charge or wake fields [19].

Furthermore the IFEL has an advantage in terms of achievable gradient for a given laser intensity. The rate of change in energy for an IFEL is proportional to the product of the laser and undulator normalized vector potential amplitudes defined as the momentum carried by each field divided by the product of the particle's mass and speed of light  $mc$  and given by  $K_1 = eA_1/mc = eE_1/kmc^2$  and  $K = eA_w/mc = eB_w/k_w mc$  where  $E_1$  and  $B_w$  are the laser electric and undulator magnetic field amplitudes, and  $k$  and  $k_w$  are the laser and undulator wavenumbers. In all of this thesis we will make the assumption that  $K_1 \ll K$

which is typical for existing IFELs due to the large difference of the undulator and laser wavenumbers. Since the undulator parameter  $K$  can be easily made larger than unity using few-cm long periods and 0.5 T-level fields, impressive gradients can be sustained even at non-relativistic laser intensities. To draw a comparison, laser wake field accelerators (LWFA) present a characteristic dependence of the accelerating wave amplitude as  $K_1^2$  and have only demonstrated significant energy gain with relativistic (i.e.  $K_1 > 1$ ) laser intensities [20].

One limit to using high power lasers to drive acceleration is that laser intensity fluctuations cause output energy fluctuations. For example, LWFA's characteristic output energy of  $\gamma_f \sim K_1^2/n_0$  is modulated by both laser intensity  $I_0$  and plasma density  $n_0$  fluctuations as  $\delta\gamma_f/\gamma_f = \sqrt{(\delta I_0/I_0)^2 + (\delta n_0/n_0)^2}$ . Consequentially, typical shot to shot variations in output parameters for laser wake field accelerators are 1-5% for energy, 1-10% for relative energy spread, and 5-50% for charge [21]. On the other hand since the IFEL's phase space evolution is determined by a static undulator field, its resonant energy output is constant. At worst if injected slightly off resonance, the beam's energy may vary within the IFEL's relative resonant energy bandwidth, which is proportional to  $\sqrt{K_1 K}$  and typically at most a few percent (see Equation 2.35). As discussed, this quantity may even be made much smaller by simultaneously reducing the coupling and resonant phase to zero to adiabatically release the beam from the IFEL interaction. The IFEL may be designed to accommodate laser parameter tolerances in order to accelerate any desired fraction of input beam to a fixed final energy, producing beams with relative energy spreads also scaling by the resonant energy bandwidth. With controllable output characteristics and modest sensitivities to input parameter fluctuations, the IFEL is the most stable laser accelerator capable of significant energy gain for relativistic electron beams.

To give a historical context for the current work, we review previous high energy IFEL experiments. The first experimental demonstration, the IFELA ex-

periment at Columbia, staged an FEL producing 5 MW of 1.6 mm radiation and a 37.5 cm bifilar helical undulator with magnetic field of 400 G and period tapered from 1.8 to 2.25 cm to accelerate electrons from 750 keV to  $\sim 1$  MeV with an average gradient of 700 keV/m [22]. Interestingly in the same paper reporting the results of IFELA, the authors then proposed an experiment with similar parameters to our current work. The BNL STELLA2 experiment [23] staged a microbuncher and gap-tapered, planar undulator with a 45 MeV electron beam and  $\sim 2$  TW/cm<sup>2</sup> CO<sub>2</sub> laser to produce narrow-energy electron beams with energy gains up to 9 MeV and fraction captured up to 80%. This experiment took advantage of one of the characteristics of the IFEL output beam to be composed by a sequence of microbunches phase-locked to the drive laser frequency. The UCLA Neptune IFEL experiment [24] achieved 20 MeV energy gain and 70 MeV/m accelerating gradient with a period and magnetic field tapered undulator and strongly focused 400 GW CO<sub>2</sub> laser and 14.5 MeV input electron beam and demonstrated for the first time higher harmonic IFEL interaction [25]. This was the first IFEL designed to operate in the diffraction dominated regime whereby the laser field strength changes significantly within the accelerator [26]. Our work in this dissertation was designed with the same principles but in a helical geometry and at a higher initial energy to demonstrate improved IFEL performance of 54 MeV gain and 100 MeV/m average accelerating gradient. A more recent IFEL accelerator, the LLNL-UCLA IFEL at Lawrence Livermore National Lab, set a new record of 150 MeV/m by utilizing a commercially available multi-TW Ti:Sa laser and 70 MeV electron beam with the same undulator used in the Neptune IFEL experiment [27].

IFEL accelerators typically have used planar undulators to couple electronic motion to laser fields. In this geometry, the electron velocity component parallel to the laser electric field is periodically reduced to zero, effectively halting the energy transfer twice per period as illustrated in Figure 1.1. Employing a helical

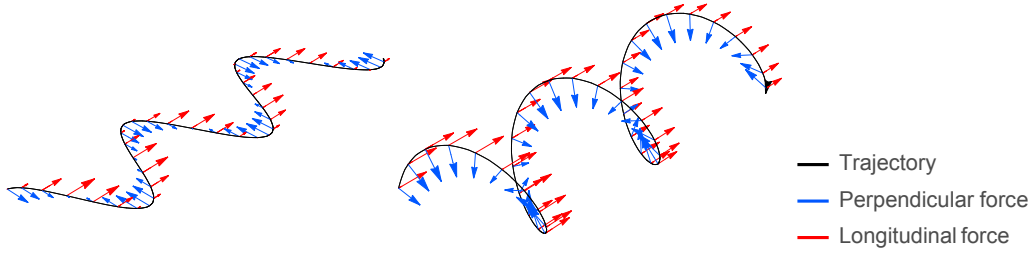


Figure 1.1: Diagrams show the transverse and longitudinal (scaled by a large factor for representation purposes) net forces along a resonant electrons trajectory for a planar (left) and helical (right) IFEL. The acceleration remains continuous in a helical IFEL since the electron continues to move transversely whereas for a planar IFEL, the acceleration is reduced to zero at the turning points of the particle motion where the transverse velocity is zero.

undulator magnetic field induces a helical motion for the electrons which provides continuous energy transfer with a circularly polarized laser of the same handedness. To quantify, the IFEL coupling strength is proportional to the Bessel factor  $JJ = J_0(G) - J_1(G)$  with  $G \equiv K^2/4(1 + K^2)$ . For planar undulators, this term approaches unity for small  $K$  and approximately 0.7 for large  $K$ , while for helical undulators,  $JJ = 2$ , more than doubling the gradient.

The experimental work described in this dissertation, the UCLA-BNL IFEL collaboration at ATF, was conceived to improve accelerating gradients through the use of the first strongly period- and field-tapered helical undulator which much of this work went into the design and construction of. The experiment was executed in a series of subsequently improved runs. Performance initially suffered when the experimental laser Rayleigh range had to be increased by 300% from design due to some experimental constraints, causing the entire beam to completely lose resonance before full acceleration; however, the undulator was rebuilt to accommodate this, leading to full acceleration of nearly 30% of the beam. A benefit of a longer Rayleigh range was a larger tolerance for spatial overlap. In our experiment as in the Neptune and LLNL IFEL experiments, a

sizable fraction of electrons detrapped near the laser waist. We analyze the effect of e-beam sizes and trajectories which become comparable to the laser waist in Chapter 3 and offer guidance for choosing a minimum laser waist. Construction of a prebuncher more recently enabled full acceleration of over half the electron beam, leading to plans for putting this accelerator to work driving a Compton scattering source; however as this work is ongoing, it will only be partially discussed in this thesis.

The principles and methods developed for the IFEL may be useful when applied to the task of decelerating an electron beam. In this case, energy is transferred from the electrons to radiation. Whereas an FEL may convert only a small fraction  $\rho \sim 0.001$  of the electron energy into radiation, an IFEL decelerator may transfer  $>50\%$  of the energy if properly designed. In fact, reversing the same undulator from our experiment should nearly halve the energy of a 400 A, 65 MeV electron beam with a 100 GW seed laser this year, generating 12 GW in a single 54 cm pass. The final chapter of this dissertation presents our work analyzing this mode of operation, which we call tapering enhanced stimulated superradiant amplification or TESSA for short. By combining TESSA with a high rep-rate superconducting linac, it would be possible to create high peak and average power lasers for EUV lithography, single molecule imaging, or driving other advanced accelerators.

## 1.2 Outline of this dissertation

The work in this tome is presented as follows. In the following chapter, the IFEL particle dynamics are analyzed within a classical framework, and methods are developed for designing undulators which maximize acceleration for any desired fraction of an input beam. Chapter 3 first shows the results of numerical studies of applying these design methods to the example of a meter long GeV IFEL acceler-

ator and later presents an investigation into the effects of transverse dynamics on the accelerator's performance. The [fourth](#) and [fifth](#) chapters report the setup and results, respectively, of the UCLA-BNL helical IFEL accelerator experiment at the Accelerator Test Facility. In [Chapter 6](#), the application of IFEL to deceleration is explored, leading to a method of efficient radiation production called TESSA or tapering enhanced stimulated superradiant amplification. Finally, conclusions and an outlook for the future of IFEL acceleration is reported in [Chapter 7](#).

## CHAPTER 2

### IFEL theory

In this chapter, we describe the IFEL particle dynamics closely following the classical framework utilized in [14] and [28]. We first examine the undulator induced particle motion which dominates the transverse dynamics, calculating the trajectory of the beam centroid as well as the evolution of the beam rms spot size and emittance. The transverse motion is then combined with laser fields to calculate the evolution of the longitudinal motion and produce the accelerator equations. We assume here that the radiation power does not evolve—the so called, frozen field regime—which is a good approximation so long as the intensity absorbed by the beam is a negligible fraction of the laser intensity. The analysis of the situation where this approximation no longer holds requires numerical methods and is left to the following chapter of this dissertation.

In the second part of the chapter, we study the conditions for resonant interaction starting from the accelerator equations and define the resonant particle energy and phase. An analysis of the deviations from resonance leads to the concept of the accelerating bucket and synchrotron oscillations of particles within that bucket. We use the geometry of the bucket to estimate the accelerator acceptance and derive a prescription for varying the resonant phase to keep the bucket area constant throughout the interaction. We then use the accelerator equations to derive the undulator tapering equations, taking into account the evolution of the Gaussian mode laser's phase evolution. Finally we investigate how to choose the laser focal parameters to maximize acceleration while maintaining full beam

capture.

The work in this dissertation focuses exclusively on the helical IFEL interaction so we explicitly use a helical undulator vector potential in these derivations. The results may be adapted for use with planar IFELs by replacing  $K$  and  $K_l$  with their rms values for their planar counterparts and replacing each instance of  $K_l K$  with  $K_l K (J_0(G) - J_1(G))$ , where  $G \equiv K^2/4(1 + K^2)$ , to account for the reduced coupling in the planar case. A good derivation of the planar IFEL dynamics in the diffraction dominated regime including higher harmonic interactions may be found in [26].

Note that here in this chapter, we only discuss the effects of a circularly polarized Gaussian laser on the helical IFEL dynamics in anticipation of experimental results to be shown in a [later chapter](#). On the other hand, others have examined interactions using higher-order Gaussian modes which have yielded some surprisingly useful results. Using higher order Laguerre-Gaussian modes with nonzero orbital angular momentum enables harmonic resonances as shown in [29]. [30] analyzes an interesting case of coupling electrons with a plane polarized TEM<sub>10</sub> in a planar undulator to create an optical deflector. While not strictly related to IFEL acceleration, these techniques attest to the versatility of coupling electrons to radiation in an undulator and may be of interest to the reader.

## 2.1 Transverse dynamics

Consider a free electron with energy  $\gamma mc^2$  copropagating in an electromagnetic field. The Hamiltonian for the system is given by the particle energy.

$$H = \sqrt{(\vec{p} - q\vec{A})^2 c^2 + m^2 c^4} + q\phi \quad (2.1)$$

Here, the mass, charge, and canonical momentum of the electron is  $m$ ,  $q$ , and  $\vec{p}$

while  $\phi$  and  $\vec{A}$  denote the electromagnetic scalar and vector potentials. In an IFEL, the vector potential is supplied by the undulator and laser while the externally applied electrostatic potential is zero. Near the axis, the helical undulator vector potential is approximately given by

$$\vec{A}_u = \frac{B}{k_u} \left( \hat{x} \left( \left[ 1 + \frac{k_u^2}{8} (3y^2 + x^2) \right] \cos \psi_u - \frac{k_u^2}{4} xy \sin \psi_u \right) + \hat{y} \left( \left[ 1 + \frac{k_u^2}{8} (3x^2 + y^2) \right] \sin \psi_u - \frac{k_u^2}{4} xy \cos \psi_u \right) \right) \quad (2.2a)$$

$$\psi_u = \int_0^z k_u dz' \quad (2.2b)$$

The terms second order in the transverse coordinates of the first equation are responsible for transverse focusing. We will return to this subject shortly, but in the meantime, we will drop terms higher than first order in the transverse coordinates since they do not affect the beam trajectory as the deviations of particles from the axis are small compared to the undulator period. Since the wavenumber  $k_u$  is a function of the longitudinal position  $z$ , the phase  $\psi_u$  is the integral over the changing wavenumber as shown in Equation 2.2b. With the definition of the normalized undulator vector potential amplitude  $K \equiv |q|B/mck_u$ , we have

$$\vec{A}_u = \frac{mcK}{|q|} (\hat{x} \cos \psi_u + \hat{y} \sin \psi_u) \quad (2.3)$$

The evolution of the canonical momentum is determined by the gradient of the Hamiltonian taken with respect to the canonical coordinates; however, the absence of the transverse coordinates in the Hamiltonian implies that the transverse canonical momentum is conserved. Before entering the undulator and before interacting with the laser, the canonical momentum is equal to the initial mechanical momenta  $\vec{p} = \gamma m \vec{x}_0$ .

The temporal evolution of the particle coordinates can be found by taking the

partial derivative of  $H$  with respect to the canonical momenta. For the spatial coordinates, we have

$$\frac{d\vec{x}}{dt} = \frac{\partial H}{\partial \vec{p}} = \frac{\vec{p} - q(\vec{A}_u + \vec{A}_l)}{\gamma m} \quad (2.4)$$

As mentioned in the introduction where we discuss IFEL's dependence on laser intensity, the momentum  $qA_l$  carried by the laser field is typically much less than  $mc$  for IFELs. On the other hand, the momentum carried by the undulator field  $qA_u$  tends to be of order  $mc$ . In other words,  $A_l \ll A_u$  and, the laser does not significantly affect the trajectory of the electrons and can be ignored in Equation 2.4. Thus to a good approximation, the velocity can be approximated by Equation 2.5.

$$\dot{x} = \dot{x}_0 - \text{sgn}(q) \frac{cK}{\gamma} \cos \psi_u \quad (2.5a)$$

$$\dot{y} = \dot{y}_0 - \text{sgn}(q) \frac{cK}{\gamma} \sin \psi_u \quad (2.5b)$$

Dots denote derivatives with respect to time. The integral of the velocity yields the trajectory which may be kept on axis by finely tuning the magnetic field. As a result, the beam travels along a helical trajectory with a tangential velocity of  $\dot{x}_\perp = cK/\gamma$ , radius of  $r = K/\gamma k_u$ , and a pitch of  $\lambda_u$ .

### 2.1.1 Betatron motion

As a second order approximation, we include the off-axis terms in Equation 2.2. The variation of the momentum is determined by the variation of the Hamiltonian with respect to the particle coordinates.

$$\frac{dp_i}{dt} = -\frac{\partial H}{\partial x_i} = q \frac{\vec{p} - q\vec{A}}{\gamma m} \cdot \frac{\partial \vec{A}}{\partial x_i} = q \frac{d\vec{x}}{dt} \cdot \frac{\partial \vec{A}}{\partial x_i} \quad (2.6)$$

The last step makes use of Equation 2.4. We use the index  $i$  for the two transverse coordinates. In order to determine the particle coordinate evolution, we take a time derivative of Equation 2.4 and substitute the above Equation 2.6 for  $\dot{\vec{p}}$ . The result is

$$\frac{d^2 x_i}{dt^2} = \frac{q}{\gamma m} \left( \frac{d\vec{x}}{dt} \cdot \frac{\partial \vec{A}}{\partial x_i} - \left( \frac{d\vec{x}}{dt} \cdot \vec{\nabla} \right) \cdot A_{u,i} \right) \quad (2.7)$$

The convective derivative in the last term describes the potential sampled by the particle as it moves in space and is simply equal to the total time derivative since the field has no explicit time dependence.

We now look for a solution which is the sum of the first order motion and a slow solution  $\vec{x} = \vec{x}_1 + \vec{x}_2$ , where  $\vec{x}_1$  is the solution to the on-axis fields given in Equation 2.5. We will make two approximations here. First, we assume that the relative change in  $\gamma$  on the velocity in Equation 2.7 is small. This is exact in the case of no acceleration and a reasonable approximation over distances short compared to  $\gamma/(d\gamma/dz)$ . Second, we will assume that the initial transverse velocity  $\dot{\vec{x}}_0$  is small compared to the tangential velocity  $cK/\gamma$  of the undulator induced helical motion. Inserting the  $\vec{x} = \vec{x}_1 + \vec{x}_2$  into Equation 2.7 and averaging over the relatively fast transverse oscillations induced by the undulator leads to two coupled equations for the transverse motion describing the slower betatron oscillations of the electron beam.

$$\begin{aligned} x_2'' - k_u \left( \frac{K}{\gamma} \right)^2 y_2' + \frac{1}{2} k_u^2 \left( \frac{K}{\gamma} \right)^2 x_2 &= 0 \\ y_2'' + k_u \left( \frac{K}{\gamma} \right)^2 x_2' + \frac{1}{2} k_u^2 \left( \frac{K}{\gamma} \right)^2 y_2 &= 0 \end{aligned} \quad (2.8)$$

We use the approximation that  $dz \approx cdt$  and use primes to denote derivatives with respect to  $z$ . The effect is a restoring force on the electrons symmetric in  $x$  and  $y$  and a solenoid force which couples the two transverse planes. We can solve

this system of equations by multiplying the second by the imaginary unit  $i = \sqrt{-1}$ , adding it to the first, and substituting  $\xi \equiv x_2 + iy_2$ . The resulting solutions are elliptical oscillations with spatial frequencies  $k_\beta = \frac{k_u}{2} \left(\frac{K}{\gamma}\right)^2 (1 \pm \sqrt{1 + 2\gamma^2/K^2})$ . Reference [31] studies this motion in detail and shows that the input transverse emittance  $\epsilon_x = \sqrt{\sigma_x^2 \sigma_{x'}^2 - \sigma_{x,x'}^2}$  is conserved after the beam exits the undulator but while in the undulator the horizontal and vertical planes mix.

Typically the particle Lorentz factor is much greater than the undulator parameter  $K$  in IFEL accelerators so to a good approximation, the solenoid effect is ignorable and the spatial frequency becomes simply  $k_\beta = k_u K / \sqrt{2} \gamma$ . The result are betatron oscillations with a wavelength given by  $\lambda_\beta = \sqrt{2} \lambda_u \gamma / K$ —noticeably longer than the undulator period. The undulator is said to be weakly focusing. Electron beams naturally have a distribution of positions and angles causing them to diverge. By properly focusing the beam to diverge at the same rate that the undulator focuses, a constant spot size may be achieved (i.e. transverse matching).

The spot size evolution can be related to the external focusing force and the normalized emittance by the envelope equation  $\sigma_x'' = \epsilon_x^2 / \sigma_x^3 - \langle xx'' \rangle / \sigma_x$  [32]. Multiplying Equation 2.8 (ignoring solenoid coupling terms) by the position and averaging yields an expression for  $\langle xx'' \rangle$  which can be substituted into the relation for  $\sigma_x''$  to yield the rms envelope equation.

$$\sigma_x'' + \frac{1}{2} \left( \frac{k_u K}{\gamma} \right)^2 \sigma_x = \frac{\epsilon_x^2}{\sigma_x^3} \quad (2.9)$$

The equilibrium spot size can be found by setting  $\sigma_x'' = 0$  and solving for  $\sigma_x$ .

$$\sigma_{x,\text{equilib}} = \sqrt{\frac{\epsilon_x \lambda_\beta}{2\pi}} = \sqrt{\frac{\epsilon_x \lambda_u \gamma}{\sqrt{2}\pi K}} = \sqrt{\frac{\epsilon_{x,n} \lambda_u}{\sqrt{2}\pi K}} \quad (2.10)$$

Here,  $\epsilon_{x,n} \equiv \gamma \epsilon_x$  is the normalized emittance. As we will see in the following sections, acceleration requires changing the undulator parameters, so external focusing may be required to maintain a small spot size. Often, the betatron length

$\beta_{x,\text{equilib}} = \lambda_\beta/2\pi = \lambda_u/\sqrt{2\pi}K$  is a more useful quantity to keep in mind during the early stages of the design of an IFEL since it is independent of emittance.

If the injected beam's transverse spot size is initially larger than the equilibrium spot size, the undulator focusing force in Equation 2.8 will outweigh the emittance pressure leading to betatron oscillations in the spot size. Nevertheless since the restoring force from the undulator focusing is linear, the transverse emittance is preserved.

### 2.1.2 Transverse emittance

We now examine the effect of acceleration on emittance evolution. While deriving the Lorentz force relation for a static vector potential in Equation 2.7, we assumed that  $\gamma$  was constant when taking the time derivative of the velocity in Equation 2.4. Lifting this assumption adds a term  $\frac{1}{\gamma} \frac{d\gamma}{dz} \frac{dx_i}{dt}$  to the left side of Equation 2.7. Using the same analysis of the betatron motion and again ignoring the solenoid terms yields equations for two damped harmonic oscillators.

$$\begin{aligned} x_2'' + \frac{1}{\gamma} \frac{d\gamma}{dz} x_2' + k_\beta^2 x_2 &= 0 \\ y_2'' + \frac{1}{\gamma} \frac{d\gamma}{dz} y_2' + k_\beta^2 y_2 &= 0 \end{aligned} \tag{2.11}$$

Solutions for both planes are damped by a term equal to the square root of the ratio of initial and final energies  $e^{-\frac{1}{2} \int d\gamma/\gamma} = \sqrt{\gamma_0/\gamma}$ . Both the positions and their velocities are damped by this term so the moments of their distributions each decrease by the same factor (e.g.  $\sigma_x = \sigma_{x,0} \sqrt{\gamma_0/\gamma}$ ). Substituting these into the calculation of the emittance yields  $\epsilon_x = \frac{\gamma_0}{\gamma} \sqrt{\sigma_x^2 \sigma_{x'}^2 - \sigma_{x,x'}^2} = \frac{\gamma_0}{\gamma} \epsilon_{x,0}$ . Multiplying both sides by the final energy  $\gamma$  yields  $\gamma \epsilon_x = \gamma_0 \epsilon_{x,0}$ . Thus, the normalized emittance  $\epsilon_{x,n} = \gamma \epsilon_x$  is conserved for each transverse plane.

It is interesting to examine situations that may violate emittance conservation. To spoil emittance, we must introduce terms nonlinear in the coordinate or its

velocity. The betatron wavenumber  $k_\beta$  only depends on the undulator parameters and not on the particle coordinates. In small aperture undulators, the beam may begin to sample the field curvature and these nonlinear forces may stretch the phase space. Another possibility would be if the energy gradient  $d\gamma/dz$  was a function of position. Although we have yet to describe the IFEL acceleration in detail, the laser is what accelerates the electrons. If the electron beam is large enough to sample significant variation in the laser field, different parts of the beam will have different amounts of acceleration and be damped at different rates which could lead to emittance growth. Consequentially, it is important to keep the beam small enough so that particles see the same magnetic and electric fields throughout the acceleration to preserve the normalized transverse emittance.

## 2.2 Accelerator equations

Achieving constant acceleration in an IFEL using a helical undulator necessitates a circularly polarized laser to match the spiraling trajectory of the electrons. The vector potential for a circularly polarized laser can be expressed in Cartesian coordinates as

$$\vec{A}_l = \frac{E_0}{\sqrt{2}ck} u(\vec{x}) (\hat{x} \cos \Phi(\vec{x}, \zeta) - \hat{y} \sin \Phi(\vec{x}, \zeta)) \quad (2.12)$$

Here,  $k = 2\pi/\lambda$  is phase advance per wavelength,  $E_0$  is the peak electric field,  $u(\vec{x})$  is a form factor modifying the peak electric field in space, and the phase of the electric field is  $\Phi(\vec{x}, \zeta)$  with  $\zeta = kz - \omega t$ . For the case of a plane wave traveling in vacuum,  $u(\vec{x}) = 1$  and  $\Phi(\vec{x}, \zeta) = \zeta$ . It is important to express parameters in terms of measurable quantities to keep things grounded in reality and connect them to experiments. The peak field is related to the intensity by the relation  $E_0 = \sqrt{2Z_0 I_0}$ , where  $Z_0$  is the impedance of free space and  $I_0$  is the laser intensity. With the definition of  $K_l \equiv |q|E_0/kmc^2$ , the vector potential becomes

$$\vec{A}_l = \frac{mcK_l}{|q|} u(\vec{x}) (\hat{x} \cos \Phi(\vec{x}, \zeta) - \hat{y} \sin \Phi(\vec{x}, \zeta)) \quad (2.13)$$

The transverse motion is modified slightly by the action of the laser.

$$\dot{x} = \dot{x}_0 - \text{sgn}(q) \frac{cK}{\gamma} \cos \psi_u - \text{sgn}(q) \frac{cK_l}{\gamma} \cos \Phi(\vec{x}, \zeta) \quad (2.14a)$$

$$\dot{y} = \dot{y}_0 - \text{sgn}(q) \frac{cK}{\gamma} \sin \psi_u + \text{sgn}(q) \frac{cK_l}{\gamma} \sin \Phi(\vec{x}, \zeta) \quad (2.14b)$$

Assuming  $K_l$  is small compared to  $K$ , the action of the laser on the transverse motion is a small quiver on top of the larger initial drift and undulator induced oscillations.

### 2.2.1 Ponderomotive acceleration

Turning to the longitudinal dynamics, the energy evolution of an electron in the combined undulator and laser fields is described by the scalar product of the velocity and electric field, calculated by the time derivative of the vector potential. The laser induced quiver velocity does not contribute significantly to the energy evolution since we have assumed that  $K_l \ll 1$ .

$$\begin{aligned} \frac{d\gamma}{dt} &= -\frac{q}{mc^2} \dot{\vec{x}} \cdot \frac{\partial \vec{A}}{\partial t} \\ &= \frac{q}{|q|} \frac{\omega}{c} K_l u(\vec{x}) \left( \left( \dot{x}_0 - \frac{q}{|q|} \frac{cK}{\gamma} \cos \psi_u \right) \sin \Phi + \left( \dot{y}_0 - \frac{q}{|q|} \frac{cK}{\gamma} \sin \psi_u \right) \cos \Phi \right) \end{aligned} \quad (2.15)$$

The change in energy is the integral of the energy gradient. Terms proportional to the initial velocity  $\dot{\vec{x}}_0$  have phases of  $\Phi(\vec{x}, \zeta)$  with phase velocities nearly equal to the speed of light. Since massive particles cannot travel at the speed of light, these terms quickly vary and therefore average to zero. Terms proportional to  $K$  have the product of two sinusoidal components, leading to a beat-wave with

phase given by Equation 2.17 which is simply the sum of the undulator and laser phases.

$$\begin{aligned} \frac{d\gamma}{dz} &= -\frac{kK_l K}{\gamma} u(\vec{x}) \sin \psi \\ \Rightarrow \frac{d\gamma^2}{dz} &= -2kK_l K u(\vec{x}) \sin \psi \end{aligned} \quad (2.16)$$

$$\psi = \psi_u + \Phi(\vec{x}, \zeta) \quad (2.17)$$

In Equation 2.16, we've made the standard approximation  $dz = cdt$  which is appropriate for ultrarelativistic beams and collected factors of  $\gamma$  on one side to show its evolution explicitly. For the case of a freely propagating plane wave laser in vacuum where  $u = 1$  and  $\Phi = k(z - ct)$ , these equations become

$$\frac{d\gamma^2}{dz} = -2kK_l K \sin \psi \quad (2.18)$$

$$\psi = (k_u + k)z - ckt \quad (2.19)$$

An interesting point is that the acceleration does not depend on the sign of the charge of the particle. This allows electrons and positrons to be accelerated with the same IFEL accelerator. The appearance of the sign of the charge in the velocity (Equation 2.5) shows that the handedness of the trajectory is determined by the charge of the particles. Space charge forces oppose synchrotron oscillations responsible for microbunching within the undulator (this will become apparent in the following section) so large current and low laser seed power may lead to repulsion of electrons, breaking up the beam and halting the acceleration. One way to overcome this limitation is to superimpose electrons and positrons to mitigate space charge effects so long as the transverse sizes of the beams are larger than the radius of oscillations.

## 2.2.2 Ponderomotive phase evolution

We now turn our attention to the evolution of the ponderomotive phase. The phase velocity is calculated by taking the time derivative of the ponderomotive phase in Equation 2.17.

$$\frac{d\psi}{dt} = k_u \dot{z} \left( 1 + \frac{1}{k_u} \frac{d\Phi}{dz} \right) + \frac{\partial\Phi}{\partial t} \quad (2.20)$$

The longitudinal velocity  $\dot{z}$  may be calculated from the energy and transverse velocity in Equation 2.14.

$$\frac{\dot{z}^2}{c^2} = 1 - \frac{1 + K^2 + K_l^2 - 2KK_l \cos \psi}{\gamma^2} - \frac{1}{c^2} (\dot{x}_0^2 + \dot{y}_0^2) + \frac{K}{c\gamma} (\dot{x}_0 \sin \psi_u + \dot{y}_0 \cos \psi_u) \quad (2.21)$$

The undulator induced oscillations dominate the phase evolution, yet the laser induced quiver should not be ignored here. For ultra relativistic beams where  $\dot{z} \approx c$ , the transverse velocities are nearly equal to an initial angular deviation:  $x'_0 = \dot{x}_0/c$  and  $y'_0 = \dot{y}_0/c$ .

$$\dot{z} \approx c - \frac{c}{2\gamma^2} (1 + K^2 + K_l^2 - 2KK_l \cos \psi + \gamma^2(x_0'^2 + y_0'^2)) \quad (2.22)$$

The angular terms should be made much smaller than  $K^2$  in order to allow the undulator to dominate control over the beam's longitudinal velocity:  $x_0'^2 + y_0'^2 \ll K^2/\gamma^2$ . We have ignored the sinusoidal terms in Equation 2.21 as they average to zero over an undulator period and their magnitudes are small with the requirement we just imposed.

Inserting the longitudinal velocity from Equation 2.22 into the equation for the phase velocity yields an expression for the phase evolution in terms of the undulator and particle parameters.

$$\frac{1}{k_u} \frac{d\psi}{dz} = \frac{1}{k_u \dot{z}} \frac{d\psi}{dt} = 1 + \frac{1}{k_u} \frac{\partial \Phi}{\partial z} + \frac{1}{ck_u} \frac{\partial \Phi}{\partial t} \left( 1 - \frac{1 + K^2 + K_l^2 - 2KK_l \cos \psi + \gamma^2(x_0'^2 + y_0'^2)}{2\gamma^2} \right)^{-1} \quad (2.23)$$

For the case of a freely propagating plane wave laser in vacuum where  $u = 1$  and  $\Phi = k(z - ct)$  and with the reasonable assumption that  $1 + K^2 \ll 2\gamma^2$ , we obtain the phase evolution relation

$$\frac{d\psi}{dz} = k_u \left( 1 - \frac{k}{2k_u \gamma^2} (1 + K^2 + K_l^2 - 2KK_l \cos \psi + \gamma^2(x_0'^2 + y_0'^2)) \right) \quad (2.24)$$

The energy only appears quadratically in the equations of motion (Equations 2.16 and 2.23 due to the fact that the IFEL is a second order mechanism which requires both undulator and laser fields to achieve acceleration. This is further evident by the appearance of the product of  $K$  and  $K_l$  in the energy equation of motion.

Only particles which do not slip significantly relative to the ponderomotive wave may resonantly exchange energy with the radiation. Ignoring the small effect of the laser quiver induced phase delay and requiring the phase velocity to be zero in Equation 2.24 leads to the energy of a resonant particle for a plane wave laser.

$$\gamma_r^2 = \frac{1 + K^2}{\frac{2\lambda}{\lambda_u} - (x_0'^2 + y_0'^2)} \quad (2.25)$$

It is interesting to note that other than the initial angle of the particle, which may be made zero or very small, this resonant energy depends only on the undulator parameters and wavelength of the driving radiation. Viewed in this way, the undulator's main function is to delay the electrons so that they stay at the same laser phase front on average. Without this delay, the laser would wash over

the particles with little residual effect on their energy as the sinusoidal variation in the field averages to zero.

While the freely propagating laser's phase evolution is predetermined by choice of focusing optics and the electromagnetic wave equation, the undulator may be designed with variable parameters to control the evolution of the particle's phases. As the electrons' energies change according to Equation 2.16, they begin to slip relative to the ponderomotive wave. In order to continue to maintain resonance, the undulator parameters may then be changed to account for the changing energy of the beam.

### 2.2.3 Acceleration with a Gaussian laser

Often laser modes approximate that of a Gaussian laser so we recast the accelerator equations with it using the following definitions:  $u = \frac{w_0}{w(z)}e^{-r^2/w^2(z)}$  and  $\Phi = kz - \omega t - kr^2/2R(z) + \phi_g$ . Here,  $\zeta = kz - \omega t$ , the waist is  $w(z) = w_0\sqrt{1 + M^4(z - z_w)^2/z_r^2}$ ,  $w_0$  is the beam's minimum waist size,  $z_w$  is the position of the waist, and  $z_r$  is the Rayleigh range of the mode. This set of parameters is degenerate and connected by the relation  $z_r\lambda = \pi w_0^2$ . The factor  $M^2$  is conventionally used to describe the approximate diffraction of a laser with multiple higher order transverse modes and takes on values  $\geq 1$ .

The exponential term in  $u$  describes the transverse amplitude of the Gaussian mode as it propagates. The electron beam should be well within one waist  $w_0$  of the axis in order to experience a relatively homogeneous field strength during acceleration. In fact, just straying off axis by  $w_0/3$  reduces the field by 10%. This should be considered when calculating the gradient of helical undulators since for planar undulators, the electrons spend more time near the axis where they gain the most momenta.

The first term in  $\Phi$  describes the forward propagation of the radiation phase

fronts. The second term describes the off-axis phase variation.  $R(z) = z_r^2/(z - z_w) + z - z_w$  is the radius of curvature of phase fronts along the direction of propagation and tends to be large near the waist so that the phase fronts are relatively flat. The final term is the Gouy phase shift  $\phi_g = \arctan(z - z_w)/z_r$  which corrects for the fact that as the beam narrows to a waist, the longitudinal wavenumber changes according to the dispersion relation  $k_z = \sqrt{k^2 - k_\perp^2}$  where  $k_\perp$  is the transverse wave vector [32]. Putting this all together, we get:

$$\vec{A}_l = \frac{mcK_l}{q} \frac{w_0}{w(z)} e^{-r^2/w^2(z)} \left( \hat{x} \cos\left(k\zeta - \frac{kr^2}{2R(z)} + \phi_g\right) - \hat{y} \sin\left(k\zeta - \frac{kr^2}{2R(z)} + \phi_g\right) \right) \quad (2.26)$$

Inserting this into the accelerator equations yields equations for the ponderomotive gradient and phase.

$$\frac{d\gamma}{dt} = -\frac{ckK_lK}{\gamma} \frac{w_0}{w(z)} e^{-r^2/w^2(z)} \sin \psi \quad (2.27)$$

$$\psi = kz - \omega t - \frac{kr^2}{2R} + \phi_g + \psi_u \quad (2.28)$$

The appearance of the scaled radial coordinate  $r/w(z)$  in the ponderomotive gradient confirms our assertion that nearly uniform acceleration requires the entire beam to be well within the laser waist  $w(z)$  throughout the interaction. The ponderomotive phase variation for a Gaussian beam is found by taking the derivative of the ponderomotive phase above and substituting the longitudinal velocity (Equation 2.22).

$$\begin{aligned} \frac{d\psi}{dz} = & k_u - \frac{kr^2}{2R(z)^2} \left( 1 - \frac{z_r^2}{(z - z_w)^2} \right) + \frac{w_0^2}{z_r w(z)^2} \\ & + \frac{k}{2\gamma^2} (1 + K^2 + K_l^2 - 2KK_l \cos \psi + \gamma^2(x'^2 + y'^2)) \end{aligned} \quad (2.29)$$

Again, we made here the approximation that the Lorentz factor is much larger than unity and that the initial angle is small. Requiring a stationary phase leads to the resonant energy.

$$\gamma_r^2 = \frac{1 + K^2}{\frac{2k_u}{k} + \frac{r^2}{R(z)^2} \left(1 - \frac{z_r^2}{(z-z_w)^2}\right) + \frac{2w_0^2}{kz_r w(z)^2} - x_0'^2 - y_0'^2} \quad (2.30)$$

Terms in the denominator may be made small with sufficiently relaxed focusing so that the radius of curvature of the phase fronts does not change quickly. With sufficiently relaxed focusing so that the phase fronts appear flat, Equations 2.28, 2.29, and 2.30 become approximately equal to their plane wave counterparts described in Section 2.2.2.

### 2.3 Longitudinal dynamics

So far the analysis of the longitudinal motion has been limited to single particle dynamics whereas a beam is a collection of a large number of particles. The ponderomotive gradient (see Equation 2.16) is proportional to  $-\sin \psi$ , and the phase of the resonant particle is constant. For acceleration (negative phases), particles with phases lagging behind the stationary phase of the resonant particle experience a larger accelerating gradient helping them to catch up. On the other hand, particles leading the resonant particle are pushed less by the ponderomotive wave so that they fall back towards the resonant particle. This restoring force leads to oscillations about the phase of the resonant particle or resonant phase  $\psi_r$ , and these periodic variations of the particles about their equilibrium phase and energy are referred to as synchrotron oscillations.

It is advantageous to keep the beam near the peak of the ponderomotive wave at phase  $\psi = -\pi/2$  for increased acceleration. On the other hand, if particles lagging behind the resonant particle pass too far behind the peak of the accelerat-

ing wave, they may be pushed less than the resonant particle, never able to catch up to the rest of the beam and lost from the near resonant interaction. A useful accelerator must be able to accelerate a significant fraction of the electrons so the longitudinal dynamics must be considered carefully.

We begin the analysis similarly to that of [28] and use the plane wave laser approximation for the accelerator equations in order to simplify the discussion of the dynamics in this section. The considerations in this section can then be extended to the case of a Gaussian laser as done in the previous section. Since we are interested in the behavior of particles whose energy approximately satisfies the resonance condition, we first introduce a new variable describing the energy deviation from the resonance to examine the deviations from resonance and use these to write down a Hamiltonian describing the longitudinal phase space. We will use this to describe particle trapping and then turn to examine synchrotron oscillations about the resonant point. After discussing synchrotron oscillations near resonance, we will show how to take advantage of these dynamics to manipulate the entire beam phase space and control the acceleration. Finally, we discuss methods for preventing unnecessary phase space dilution in the accelerator by properly preparing the beam's phase space to fit within the accelerator's acceptance.

### 2.3.1 Regions of stability

To analyze the dynamics in longitudinal phase space, let us first approximate the equations of motion for particles with small detuning or relative deviations from the resonant energy  $\eta \equiv \gamma/\gamma_r - 1$ . Relating this to the energy  $\gamma^2 = \gamma_r^2(1 + \eta)^2$  and taking a derivative yields a relation for the energy detuning.

$$\frac{d\eta}{dz} \approx \frac{1}{2\gamma_r^2} \left( \frac{d\gamma^2}{dz} - \frac{d\gamma_r^2}{dz} \right) \quad (2.31)$$

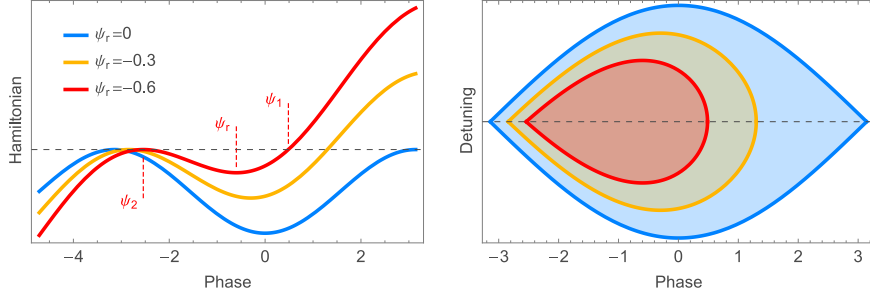


Figure 2.1: The ponderomotive potential ( $H$  evaluated for  $\eta = 0$ ) is shown on the left for various resonant phases, while the bound regions (shaded) for each of these resonant phases are depicted on the right. The units on the vertical axes are arbitrarily scaled.

With this approximation, the equations of motion 2.18 and 2.24 are approximated by Equation 2.32 below.

$$\frac{d\eta}{dz} \approx -\frac{kK_l K}{\gamma_r^2} (\sin \psi - \sin \psi_r) \quad (2.32a)$$

$$\frac{d\psi}{dz} \approx 2k_u \eta \quad (2.32b)$$

These approximate equations of motion are derivable from the following Hamiltonian.

$$H = ck_u \left( \eta^2 - \frac{2K_l K}{1 + K^2} (\cos \psi + \psi \sin \psi_r) \right) \quad (2.33)$$

Particles follow trajectories with constant value of the Hamiltonian. Most of these trajectories are unbounded, lead to large phases, and could be viewed as scattering states. On the other hand, there are regions of phase space near resonance with bound, oscillatory trajectories.

For a given resonant phase  $\psi_r$ , these stable regions of longitudinal phase space or ponderomotive buckets each contain a local minimum of the Hamiltonian. The minima are the so called stable resonant points with energy  $\gamma_r$  (no detuning or

$\eta = 0$ ) and phase  $\psi_r + 2\pi n$  where  $n$  is an integer. Particles within the stable accelerating buckets rotate about the resonant points, and can remain trapped during the acceleration as long as the approximation of constant Hamiltonian motion is valid, that is as long as ponderomotive coupling strength  $K_l K / (1 + K^2)$  and resonant phase  $\psi_r$  do not vary appreciably within a synchrotron oscillation.

Let's turn our attention to the bucket and examine its properties. One edge of the bucket has a saddle point which we can find by zeroing the simplified equations of motion in Equation 2.32. Zeroing the phase velocity yields  $\eta = 0$  whereas requiring  $d\eta/dt = 0$  leads to the equation  $\sin \psi = \sin \psi_r$ . The trivial solution  $\psi = \psi_r$  is the resonant point and a stable minimum of the potential. Another solution, given in Equation 2.34, is the phase of the saddle point.

$$\psi_2 = \pi \operatorname{sgn} \psi_r - \psi_r \quad (2.34)$$

The boundary of the bucket has the same value of the Hamiltonian as the saddle point. Requiring that the Hamiltonian be at most equal to its value at the saddle point yields an expression for a contour defining this region of phase space.

$$\eta_{\text{sep}}^2 \leq \frac{2K_l K}{1 + K^2} (\cos \psi + \cos \psi_r + (\psi + \psi_r - \pi \operatorname{sgn} \psi_r) \sin \psi_r) \quad (2.35)$$

The curve in longitudinal phase space bounding this region is a separatrix since bound and scattering state particles may not cross it, causing bound particles to remain trapped. It should be noted at this point that whereas particles cannot cross a stationary separatrix, the separatrix may move since it is determined by the external parameters  $K$ ,  $K_l$ , and  $\psi_r$ . For example as we will see, bound particles detrap if the parameters of the Hamiltonian change too fast.

### 2.3.2 Capture estimates for a uniform current beam

The geometric parameters of the bucket are given by Equation 2.36 and illustrated in Figure 2.2.

$$\Delta\psi = |\psi_2 - \psi_1| : \cos \psi_1 + \psi_1 \sin \psi_r = \cos \psi_2 + \psi_2 \sin \psi_r \quad (2.36)$$

As a first approach to determining the optimal resonant phase for the interaction, we can ask the question: what is the maximum power that we can transfer to an electron beam which is initially uniformly distributed in phase? Usually, the laser intensity used with a IFEL accelerator is sufficiently intense so that the relative energy spread of the injected beam is negligible compared to the bucket height  $\eta_{\text{sep}}$ . In this case, all particles between phases  $\psi_1$  and  $\psi_2$  are trapped within the bucket so long as they are injected at the resonant energy. The fraction of particles trapped is just the relative width of the bucket  $\Delta\psi/2\pi$  as shown in Figure 2.2. The entire beam may be trapped with a resonant phase of zero, but of course the net acceleration would be zero as well; on the other hand, the acceleration gradient is maximized for  $\psi_r = -\pi/2$  but no particles can be trapped there. In order to maximize the power transferred, we could calculate the net acceleration averaged over the bucket width:  $P \propto -\frac{1}{\Delta\psi} \int_{\psi_1}^{\psi_2} d\psi \sin \psi$ . This convolution of bucket width and gradient is proportional to the power delivered to the beam and is shown by the yellow line in the middle plot of Figure 2.2. In this case, the resonant phase which optimally balances the fraction captured with accelerating gradient to maximize power transfer is  $\psi_r \approx -0.69$ .

If the energy spread of the beam is larger than the bucket, then only particles which land within the separatrix, defined by Equation 2.35, are captured. The area of the bucket is given by the integral of the bucket height  $J_b = 2\gamma_r \int_{\psi_1}^{\psi_2} d\psi \eta_{\text{sep}} = 2 f_J \gamma_r \sqrt{2K_l K / (1 + K^2)}$  with the normalized area  $f_J$  given by Equation 2.37. This area is the effective action of a particle trajectory along the separatrix and has

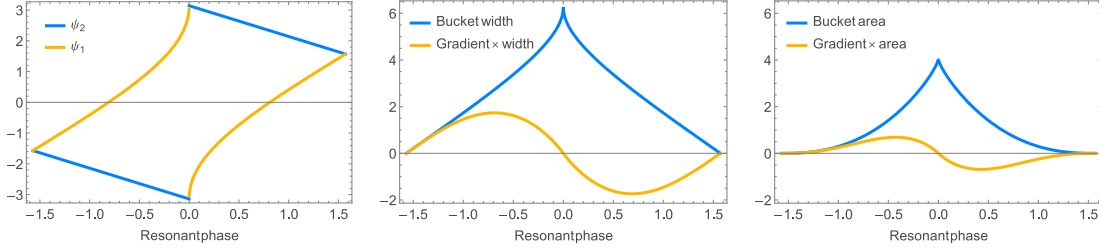


Figure 2.2: Shown as functions of resonant phase are: left, the coordinates  $\psi_1$  and  $\psi_2$  describing the extent of the bucket; middle, the relative bucket width  $\Delta\psi/2\pi$  and its convolution with the normalized gradient,  $-\sin\psi$ ; and right, the relative area of the bucket and convolution with normalized gradient.

units of action times the angular frequency of the ponderomotive wave and divided by the particle's rest energy.

$$f_J = \frac{1}{\sqrt{2}} \int_{\psi_1}^{\psi_2} d\psi \sqrt{\cos\psi + \cos\psi_r + (\psi + \psi_r - \pi \operatorname{sgn}\psi_r) \sin\psi_r} \quad (2.37)$$

The relative power delivered to the beam in this case is the integral of the gradient over the bucket area  $P \propto -\frac{1}{J_0} \gamma_r \int_{\psi_1}^{\psi_2} d\psi \eta_{\text{sep}} \sin\psi$ . Here,  $J_0 = 2\pi$  is the phase space area occupied by the injected beam, assumed to be uniformly distributed in phase and in energy between  $\pm\eta_{\text{sep,max}}$ . In this case at  $\psi_r = 0$ , the maximum fraction captured is  $2/\pi$ . The bucket area and effective power are shown in the right side of Figure 2.2. The resonant phase which maximizes power delivered in this case is close to  $\psi_r \approx -0.43$ . Comparing the results for small energy spread to these results, the former yields about 2.5 times higher delivered power for an optimum choice of resonant phase.

### 2.3.3 Synchrotron oscillations and bunching

The simplified equations of motion given by Equation 2.32 are the standard pendulum equations. Near resonance, the Hamiltonian may be approximated by a

simple harmonic oscillator. Expanding  $\sin \psi$  for small deviations from the resonant phase  $\delta \equiv \psi - \psi_r$  yields the approximation  $\sin \psi - \sin \psi_r \approx \delta \cos \psi_r$ , further simplifying the phase evolution. We will assume that the external parameters are static and that the rate of change in the resonant phase  $\dot{\psi}_r$  is small compared to the phase slippage in a period  $\dot{\psi}_r \ll 2k_u\eta$  and ignorable. The motion of a particle near resonance is then determined by a harmonic oscillator equation in  $\delta$ :  $\delta'' + k_s^2\delta = 0$ . Solutions to this equation oscillate about equilibrium in  $\delta$  and  $\eta$  by this frequency.

$$k_s = 2k_u \sqrt{\frac{K_l K}{1 + K^2} \cos \psi_r} \quad (2.38)$$

When an electron beam with an initially resonant mean energy and uniform phase distribution is injected into the bucket, particles close to resonance rotate in longitudinal phase space at this frequency. After a quarter period of oscillation, a large fraction of the particles within the bucket become bunched at the resonant phase as shown in Figure 2.3. Perfect bunching cannot be achieved in this way since not all particles in the bucket rotate at the same frequency due to the nonlinearities of the pendulum-like potential. Trajectories within the bucket but further from resonance become anharmonic with larger periods of oscillation approaching infinity at the separatrix where two stationary points reside. As a result, maximum particle density is obtained after a propagation distance slightly longer than one quarter synchrotron period in order to give the slower particles time to catch up. At this point in the interaction, the beam is periodically bunched at the laser wavelength with energy spread extending up to nearly the bucket height  $\eta_{\text{sep,max}}$ . An important application of this prebunched beam is external injection into a subsequent IFEL accelerator characterized by an accelerating bucket with a narrower phase spread, allowing a majority of the beam to be accelerated at large gradients.

Prebunching the electron beam in this way leads to an energy spread similar

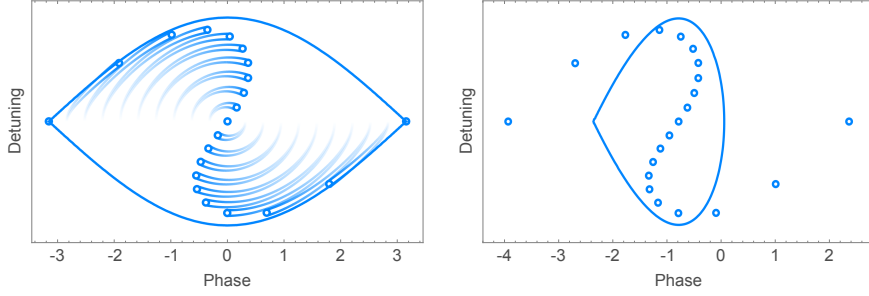


Figure 2.3: Particles bunch in phase as they rotate within the ponderomotive bucket (left). Once bunched, the particles may be injected into an accelerating bucket with narrower phase width (right).

to the ponderomotive bucket height at  $\psi_r = 0$ . The relative height of the bucket decreases as the resonant phase is moved farther from zero so the coupling factor  $\sqrt{2K_t K / (1 + K^2)}$  must be increased if one wants to inject this prebunched beam in an IFEL accelerator. One method to limit the energy spread growth during bunching is to use the IFEL interaction just to modulate the beam and then apply  $R_{56}$  compression. After a short energy modulation section, a drift or chicane is used to continue slipping the detuned particles towards each other without additional energy modulation. The resulting bunched beam has a relatively small energy spread and can be more easily injected to a non-zero resonant phase IFEL accelerator. Repeated application of undulators for energy modulation and chicanes for compression enables bunching of nearly all injected particles with ultra low energy spread growth [33].

Once captured, bound particles continue to rotate at different frequencies. If the initial energy spread of the injected electron beam is small compared to the ponderomotive bucket height, the initially concentrated phase space twists and stretches throughout the bucket so that longitudinal emittance grows. The larger emittance reduces the fraction of particles which can be fit inside subsequent accelerating buckets. This effect is unavoidable in practice but can be largely mitigated by properly matching the input longitudinal phase space and bucket

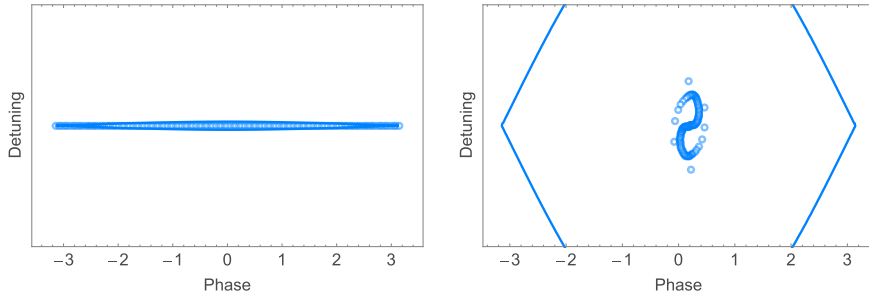


Figure 2.4: Adiabatic capture of particles by ramping up the laser field exponentially. The phase space and separatrix are shown at the entrance (left plot) and exit (right) of the buncher.

geometry. If we adopt this precaution when injecting into the accelerator, a beam may be captured adiabatically with a small resulting emittance growth.

Bunching without increasing the longitudinal emittance of a beam is known as adiabatic bunching. The bunching method of repeated pairs of undulators and chicanes approximately achieves this by periodically turning on the energy gain of the particles. Returning to the standard bunching scheme discussed here first, emittance dilution may also be avoided by first injecting the beam into a bucket with height less than the beam's energy spread so that the bucket is filled and then ramping up the field slowly so that the relative change in bucket height in a synchrotron period is small as in Equation 2.39 [32].

$$\frac{1}{\eta_{\text{sep}}} \frac{d\eta_{\text{sep}}}{dz} \ll k_s \quad (2.39)$$

Ramping up the ponderomotive wave's amplitude in this way as particles drift towards the resonant phase allows particles further from the resonant phase to be given progressively larger kicks in energy, helping them to catch up to particles closer to the resonant phase so that they arrive almost simultaneously. The bucket envelopes more particles as its height expands so the initial separatrix may be made small compared to the beam energy spread. The result is a bunched

beam with negligible phase space dilution as shown in Figure 2.4. While this is a great way to prepare a beam for injection into an accelerating bucket in principle, in practice it requires that the coupling be turned on over many synchrotron periods making such a buncher possibly longer than the accelerator. Furthermore controlling the coupling to turn on as slowly as needed for adiabatic capture to work is not a trivial task as we will see in the following chapter.

## 2.4 Undulator tapering design

The major problem of IFEL design concerns in designing a tapering profile for the undulator parameters that maximize the acceleration while preserving good output beam quality. Various undulator tapering methods have been employed in IFEL experiments to date. The IFELA experiment iteratively designed the undulator taper by hand and checked its performance with simulation [22]. STELLA used a planar undulator with a linear gap taper in order to increase the field [23]. The Neptune IFEL group developed the formalism of the diffraction dominated IFEL to calculate the taper which matches the resonant energy gradient to the ponderomotive gradient which they anticipated varying significantly with their use of a strongly focused laser [26]. We use this latter approach to calculate the variation in the undulator parameters in this section for a given resonant phase.

Equation 2.25 sets a relationship between the resonant energy and undulator parameters, and the variation in these parameters yields a change in the resonant energy.

$$\frac{d\gamma_r^2}{dz} = \frac{k}{2k_u} \left( -\frac{1}{k_u} \frac{dk_u}{dz} (1 + K^2) + \frac{dK^2}{dz} \right) \quad (2.40)$$

A first order approach is to simply vary the undulator parameters by equating this resonant energy gradient to the ponderomotive gradient in Equation 2.16 describing the change in energy of the electrons during the interaction.

$$-\frac{1}{k_u} \frac{dk_u}{dz} (1 + K^2) + \frac{dK^2}{dz} = -4k_u K_l K \sin \psi_r \quad (2.41)$$

The resonant phase  $\psi_r$  here is defined by Equation 2.17 and its relation to the longitudinal dynamics is described in the [previous section](#). When  $\psi_r$  is set to zero, the undulator parameters do not change and no net acceleration occurs. Instead, a sinusoidal modulation is imprinted on the beam which can be used to bunch the beam. The ponderomotive gradient increases along with the resonant phase. While  $\psi_r = -\pi/2$  maximizes acceleration, this happens to be an unstable phase where no particles are able to maintain resonance. Choosing a middle phase as described in the [previous section](#) offers a compromise between trapping and acceleration. In general, it may be desirable to vary the resonant phase along the undulator in order to accommodate the longitudinal particle dynamics. In the [next section](#) we will give a prescription for determining the evolution of the resonant phase along the IFEL.

For a fixed period undulator, the magnetic field amplitude must be changed in order to maintain resonance. In this case,  $dk_u/dz$  in the above equation is zero, and we obtain an equation relating the change in undulator strength to the laser amplitude.

$$\frac{dK}{dz} = -2k_u K_l \sin \psi_r \quad (2.42)$$

In permanent magnet undulators,  $K$  may be changed by varying the gap between magnets to increase the peak field on axis; however, the magnet gap may only be reduced so much before beam scraping or wakefields become an issue. Changing the period as well as the field amplitude offers more flexibility by maintaining a reasonable sized gap between magnets. Solving for  $d\lambda_u/dz$  in the gradient matching Equation 2.41, yields the following equation determining the variation in the period.

$$\frac{d\lambda_u}{dz} = -\frac{8\pi K_l K \sin \psi_r}{1 + K^2 + \lambda_u dK^2/d\lambda_u} \quad (2.43)$$

In practice, an undulator builder equation can be used to describe the relation between the undulator period and on-axis magnetic field strength. One such undulator builder equation for permanent magnet Halbach undulators such as the one used in the design of the Rubicon undulator is given here [34]

$$K = \frac{e\lambda_u}{2\pi mc} 1.8B_r e^{-\pi g/\lambda_u} (1 - e^{-\frac{2\pi Lm}{\lambda_u}}) \quad (2.44)$$

Here  $g$  is the gap between opposing magnet pole faces. Either Equation 2.42 or Equation 2.43, with the latter requiring an undulator builder equation relating  $K$  and  $\lambda_u$  such as Equation 2.44, determines the undulator tapering for a given laser field profile  $K_l$  and resonant phase  $\psi_r$ .

## 2.5 Resonant phase variation for optimal tapering

The tapering equations match the ponderomotive and resonant energy gradients for a given resonant phase, the selection of which we will now discuss. In Section 2.3, we examined the [capture estimates](#) for a constant resonant phase and discussed enhancing the fraction captured at non-zero  $\psi_r$  by [prebunching](#) and then injecting into a bucket at a different resonant phase. This two stage approach is practical and only limited by the longitudinal emittance growth induced during the bunching, which may in principle be made small via [adiabatic bunching](#).

The focus of this section will be to connect the capture and acceleration stages in a continuous way. We first determine the resonant phase variation which preserves the action throughout the acceleration. Next, we discuss the variation of the synchrotron oscillations' amplitudes and present a formula for the resonant phase which accounts for this effect.

### 2.5.1 Constant bucket size tapering

Once the beam phase space has been matched into the accelerating bucket, it is important to keep the area of the bucket constant to avoid detrapping. If the beam was properly matched into the bucket so that it fills it completely, keeping the bucket area constant prevents longitudinal emittance growth. As the particles accelerate, the bucket's dimensions necessarily vary due to changes in the laser and undulator parameters; however, we can shape the bucket with the resonant phase in the tapering equations to maintain a constant phase space density. The resonant phase which maintains constant a bucket area is given by 2.45 which was calculated by equating the area of the bucket at two points.

$$\psi_r = \text{sgn}(\psi_{r,0}) f_J^{-1} \left( \sqrt{\frac{\lambda_{u,0} K_{l,0} K_0}{\lambda_u K_l K}} f_J(\psi_{r,0}) \right) \quad (2.45)$$

Here, the quantities with subscripted zeros are the values at a point with the desired phase space area to maintain constant; ideally, this point is right where a prebunched e-beam is injected into the accelerating bucket. This strategy for choosing the resonant phase reduces phase space dilution, but still requires properly preparing the input longitudinal phase space of the beam in order to maximize acceleration while minimizing longitudinal emittance growth. Prebunching is therefore necessary to optimally utilize the IFEL.

One way to characterize the bunching might be to calculate the rms phase width of the resulting phase density for one ponderomotive wavelength of beam. However since the modulation is periodically imprinted on the e-beam, another useful measure of the degree of bunching is the bunching factor defined as the norm of the average phasor of all particles  $B = |\langle e^{i\psi} \rangle|$ . While not perfect, many bunched beam phase distributions may be reasonably approximated by a normal distribution with the mean and rms widths of the bunched beam in order to make rough calculations of the fraction of particles fitting into a smaller bucket at a

larger resonant phase. If the particle phase density can be approximated with a normal distribution within a bucket with a rms width  $\sigma_\psi$  we can relate the two quantities by

$$B = \int d\psi e^{i\psi} \frac{1}{\sqrt{2\pi}\sigma_\psi} e^{-\frac{\psi^2}{2\sigma_\psi^2}} \quad (2.46)$$

$$\Rightarrow \sigma_\psi = \sqrt{-2 \ln B}$$

Making the good assumption that the initial relative energy spread is less than the bucket height  $\eta_{\text{sep,max}}$ , we could capture 95% of the beam by choosing  $\psi_r$  such that  $\Delta\psi = 4\sigma_\psi$ . Alternatively, it may be more desirable to parametrize the design by the desired fraction captured with respect to the initial bunching factor. In this case, we observe that the fraction captured  $f_c$  is related to the bucket width and e-beam rms phase width by the error function  $f_c = \text{erf}(\Delta\psi/2\sqrt{2}\sigma_\psi)$ . Since  $\Delta\psi$  is a function of  $\psi_r$  (Equation 2.36), we can invert it to determine the initial resonant phase needed to capture a fraction  $f_c$  of the injected beam.

$$\psi_{r,0} = \Delta\psi^{-1} \left( 4\sqrt{-\ln B} \text{erf}^{-1}(f_c) \right) \quad (2.47)$$

Starting from this expression and using Equation 2.45 for calculating the resonant phase and the tapering equations (Equation 2.42 or Equations 2.43 and an undulator builder equation such as Equation 2.44) determines an efficient tapering design for an IFEL accelerator.

It is interesting to note that if an unbunched beam is injected into a bucket with  $\psi_r = 0$  and separatrix equal to the energy spread of the beam, use of Equation 2.45 eliminates the need for bunching altogether. Instead, the beam is simultaneously accelerated and bunched while preserving emittance. These principles will be investigated further when we apply them towards the design of an accelerator in the following chapter.

## 2.6 Diffractive effects

The focusing properties of the drive laser are critical to the design of the undulator as they determine the ponderomotive gradient. Considering the diffraction of a TEM<sub>00</sub> Gaussian laser, a compromise between a high intensity over a short interaction length and a low intensity interaction over a longer length should optimize the electro-optical energy exchange. Maximizing the energy conversion is achieved by maximizing the change in the resonant energy which may be calculated by integrating the ponderomotive gradient along the undulator length.

$$\Delta\gamma_r^2 = - \int_0^{L_u} 2kK_l K \sin(\psi_r) dz \quad (2.48)$$

The normalized laser vector potential for a TEM<sub>00</sub> Gaussian beam is  $K_l \sim 1/\sqrt{z_r(1 + (z - z_w)^2/z_r^2)}$ . By expanding the undulator field strength in a Taylor series  $K = \sum_n K_n z^n$  and assuming a nearly constant  $\psi_r$ , the efficiency is maximized by requiring

$$\frac{d^2}{dz_r dz_w} \sum_n \int_0^{L_u} \frac{K_n z^n dz}{\sqrt{z_r(1 + (z - z_w)^2/z_r^2)}} = 0 \quad (2.49)$$

The integral in Equation 2.49 has more support near regions of large undulator parameter  $K$  so maximal energy exchange is found by focusing the laser such that  $K_l$  is maximal in regions of large  $K$ . A reasonable approximation for the tapering is that  $K$  changes linearly. Figures 2.5a and b shows the energy change for a constant  $K$  undulator and for one with a 600% increase in  $K$  along its length. In the case that  $K$  does not vary along the interaction, the energy exchange is maximized by placing the laser waist there with a Rayleigh range of  $z_r \approx 0.15L_u$ . In general, this is a good starting point to begin the taper calculation. For the linearly tapered undulator, the optimal laser focusing places the waist  $z_w = 0.76L_u$  closer to the undulator's exit with a Rayleigh range of  $z_r \approx 0.10L_u$ , to take

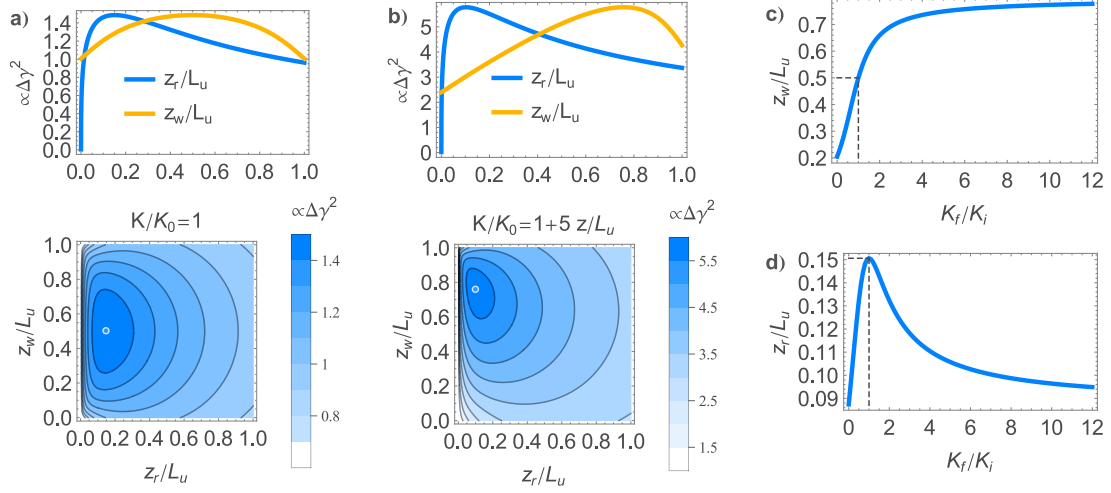


Figure 2.5: The accelerating gradient is maximized with respect to laser waist position and Rayleigh range for the case of a) a constant  $K$  undulator and b) an undulator with linearly increasing  $K$  by a factor of 6. c) and d) show how the optimal waist position and Rayleigh range scale with an undulator with linearly increasing  $K$ . Typically, acceleration requires values of  $K_f/K_0$  greater than unity while deceleration require values less than one.

advantage of the larger  $K$  near the undulator's exit.

The optimal waist position and Rayleigh range for a general undulator with linearly tapered  $K$  are shown in Figures 2.5c and d respectively. For a period tapered undulator which increases  $K$  along with the resonant energy, a ratio of final to initial undulator strengths  $K_f/K_0$  greater than unity means that the electrons are accelerated. For strong acceleration (large  $K_f/K_0$ ), the optimal waist position and Rayleigh range asymptotically approach  $z_w = 0.80L_u$  and  $z_r = 0.087L_u$ . On the other hand for an IFEL decelerator, decreasing the resonant energy decreases  $K$  so the gradient is maximized by focusing the laser near the undulator's entrance. As  $K_f$  approaches zero, the optimal focal parameters go to  $z_w = 0.20L_u$  and  $z_r = 0.087L_u$ .

# CHAPTER 3

## Numerical studies

Whereas the tapering equations discussed in the previous chapter are a good starting point in the conception of an inverse free electron laser accelerator, numerical studies of the particle dynamics are a necessary part of the design process in order to assess the validity of the model used to design the accelerator as well as incorporating physical constraints on input parameters. For example, undulator parameters such as period, field strength, or magnetic gap are constrained by limits in undulator technology or the laser waist, and laser parameters may be constrained by beam line geometry.

In order to examine the validity of some of the design principles in the previous chapter, we first introduce a conceptual design for a meter-long GeV IFEL accelerator. We next use the tapering equations to calculate the undulator parameters and resonant energy for a realistic permanent magnet undulator and consider some variations in the physical undulator parameters (e.g. magnetic gap). Next we assess the performance of the system when designed to accelerate at a constant resonant phase. Recalling the discussion of Section 2.5, we then consider designs using a variable resonant phase. We show that by capturing the beam with little growth in longitudinal emittance, the resonant phase can be increased significantly, and we present a few practical methods by which to achieve this.

Another challenge of designing an IFEL accelerator where numerical methods come handy is the case of heavy beam loading where the electron beam absorbs a significant fraction of the input laser power. We calculate the laser intensity

evolution along the undulator as a function of electron beam peak current and use this to design an undulator taper which accounts for the decreasing laser power.

### 3.1 Meter-long GeV accelerator

The IFEL was once considered as an accelerator for future high energy colliders, but enthusiasm waned when synchrotron losses were calculated to limit the practical produced energies to tens of GeVs [14]. Nevertheless, a compact GeV scale accelerator would be useful for driving modern x-ray light sources such as FELs or Compton scattering light sources. Recalling the FEL resonant energy condition from Equation 2.25, we note that the wavelength of FEL produced radiation is inversely proportional to the square of the electron energy; consequently, there is a clear need for high energy electron beams. Compton scattering similarly benefits since the produced wavelengths have the same energy dependence (the process is very similar to incoherent radiation from undulators with the exception that the static undulator magnetic field is replaced with an oscillating electromagnetic field). In this case, a significant advantage comes from the fact that the high power laser system for the Compton source can be shared and used also to drive the IFEL accelerator. For light source applications, the output beam quality is very important. In particular, the preservation of the input emittance and the control of the final energy spread are IFEL attractive attributes.

Using conventional RF technology, capable of  $\sim 50$  MeV/m average gradients, would require roughly a 20 m long linac and a dozen klystrons to produce GeV electron beams, and even state of the art higher frequency x-band RF sources would still necessitate about 10 m. Applying IFEL acceleration to this task, it is possible to reduce the total accelerator length to about 1 m by replacing all but one of the linac accelerating sections with a meter-long inverse free electron

accelerator.

Most IFEL experiments done to date simply utilized a freely propagating laser wave in vacuum. Optical waveguides or refocusing schemes have been considered as they offer the possibility of maintaining consistently high laser intensity along the entire interaction length [35, 36]; yet while high power laser pulses have recently been guided over meter-scale distances [37, 38, 39], IFEL demonstrations so far have been limited to moderate intensities [40]. Further, waveguides or lenses spoil one of the significant advantages of a far field accelerator: freedom from damage threshold limitations. In terms of design feasibility, high power TiSa laser systems providing multi-TW peak powers are commercially available [41], which are large enough to reach GeV energies in a single IFEL stage, avoiding the complications of cascading multiple accelerating modules or drive laser refocusing.

We start the accelerator design with a rough estimate of the performance for a given set of parameters. Recall that the accelerator performance for nearly constant  $K$  is optimized for  $z_w \approx L_u/2$  and  $z_r \approx 3L_u/20$ . The parameters optimizing the performance of a strongly tapered undulator differ slightly from these, but using them is a good first approximation, yielding a conservative estimate of the performance. Furthermore, the undulator parameter may be estimated as linearly increasing from an initial value of  $K_0$  and having an average value of  $\langle K \rangle$ . Finally, we define here an equivalent power  $P_e = m^2 c^4 / e^2 Z_0 = 693 \text{ MW}$  for ease of calculation. Inserting these into Equation 2.16 for the ponderomotive gradient and integrating over the length of the undulator  $L_u$  yields a conservative estimate for the energy change.

$$\Delta\gamma_r^2 \approx 5.95 \langle K \rangle \sqrt{\frac{P L_u}{P_e \lambda}} \sin \psi_r \quad (3.1)$$

The laser wavelength is 800 nm, and we shall assume that the initial e-beam energy is less than 100 MeV so that the initial undulator parameter is  $K_0 \sim 1.5$ .

Accounting for acceleration, the undulator parameter at 1 GeV is about 10 so the mean is roughly 5.8. Only the average undulator parameter factors in here since the linear term is odd in the integrand and integrates to zero under our reasonable assumption of placing the waist towards the undulator's midpoint. The length of the undulator should be about a meter for compactness and to fit the entire laser (about  $\pi$  times the laser waist) well within the undulator gap of several millimeters at the entrance of the undulator. Finally, the resonant phase maximizing the power delivered to an unbunched injected e-beam is  $\psi_r = 0.69$ . With these parameter estimates, the laser power needed to accelerate electrons to 1 GeV is about 20 TW.

### 3.2 Taper design

The undulator tapering Equation 2.43 along with the undulator builder equation 2.44 and the design parameters listed in Table 3.2 largely determine the undulator tapering. The final input requires the initial electron energy, undulator magnet properties and gap, and resonant phase to determine the final energy and fraction of electrons accelerated to full energy.

As discussed in the previous chapter, the resonant phase which maximizes the power delivered to an unbunched electron beam is  $\psi_r = -0.69$ . At this resonant phase, the gradient is still about 64% of the maximum and 43% of injected electrons should be accelerated to full energy, assuming that the energy spread is negligible. In order to enhance the gradient a bit more in the following discussion, we will use  $\psi_r = -\pi/4$ . The slightly larger relative gradient of 71% comes at the price of a low 38% trapping.

The undulator design parameters used here are similar to those used in successful IFEL experiments. The residual magnetization of each magnet is taken to be 1.22 T which is typical of NdFeB magnets with high intrinsic coercivities.

Magnets with 1.4 T residual fields with slightly lower, yet still robust, coercivities are commercially available for a similar price. Cryogenic praseodymium based undulators with residual magnetization up to 1.7 T have been demonstrated [42, 43]. These could in principle be used to increase the on-axis  $K$  for larger gradients so the designs discussed here are conservative. The length of each magnet  $L_m$  along the radial direction away from the beam axis is reasonably taken to be 2.54 cm.

The requirement for the gap  $g$  is that the clear aperture between opposing magnets is sufficiently large to allow full clearance for the electron beam and the electromagnetic radiation transport. The latter usually results in a more stringent requirement since the geometric electron beam emittance is usually smaller than the equivalent laser beam emittance of  $\lambda/4\pi$  for visible or longer wavelength radiation. This translates to a gap at least  $\pi$  times larger than the Gaussian laser waist  $w(z)$ . The [optimal Rayleigh range](#) is 15 cm for a 1 m long undulator, and the waist at the entrance and exit of the undulator is 680  $\mu\text{m}$  assuming a 800 nm drive laser focused at the undulator's center. The magnet gap should be made at least  $\pi$  times this or 2.1 mm in order to keep the field on axis high while allowing the laser to fully pass the entrance and exit without clipping.

It is instructive to look at the tapering solutions for various input energies to find the injection energy which optimizes energy gain and average accelerating gradient. Figure 3.1 shows the output energy and average accelerating gradient as a function of input energy for the given design parameters. The average accelerating gradient rises sharply near 15 MeV input energy where the resonant undulator period becomes comparable to the magnetic gap of 2.1 mm. This is because the  $e^{-\pi g/\lambda_u}$  term in the undulator builder equation suppresses the on-axis field as the period length approaches that of the gap.

Ultimately, the minimum particle energy that one can accelerate is determined by the minimum undulator period length conceivable. Superconducting undulators with periods as short as 2.42 mm with on-axis fields of  $\sim 0.5 T$  have been

<b>E-beam</b>	
Input energy $\gamma_0$	100 MeV
Energy spread $\sigma_{\gamma,0}/\gamma_0$	0.2%
Transverse emittance $\epsilon_{x,n}$	0.2 $\mu\text{m}$
<b>Laser</b>	
Peak power $P_0$	20 TW
Rayleigh range $z_r$	15 cm
Waist position $z_w$	midpoint
<b>Undulator</b>	
Length $L_u$	1 m
Residual magnetization $B_r$	1.22 T
Magnet thickness (radial) $L_m$	25 mm
Magnet gap $g$	2.1 mm
Resonant phase $\psi_r$	$-\pi/4$

Table 3.1: GeV IFEL design parameters

built [44], but superconducting equipment is expensive to construct and operate. A more practical approach using permanent magnets has lead to 9 mm periods while still producing  $K \sim 1$  [45]. Finally when considering the construction of a permanent magnet undulator, the size of each magnet becomes an issue. Smaller magnets are more likely to saturate and require higher intrinsic coercivities, but higher grades of NdFeB with increasing coercivities are more brittle so a design study is required to assess their feasibility.

For a conservative design study, we choose a starting energy of 100 MeV requiring a 14 mm initial undulator period. The undulator properties for this solution are shown in Figure 3.2. The final IFEL output energy in this case is 1.02 GeV with a 0.92 GV/m average accelerating gradient. The resulting undulator design consists of 26 periods with lengths increasing from 14 mm to 60 mm and  $K$

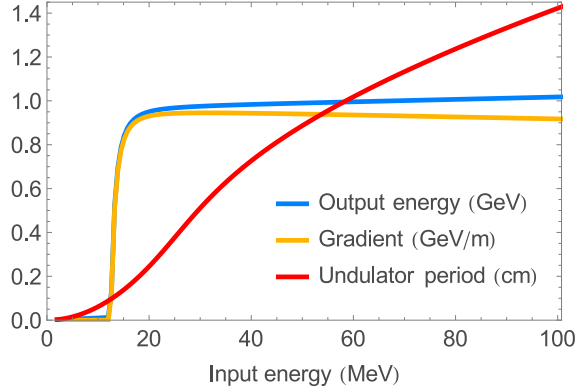


Figure 3.1: The average accelerating gradient and final energy of tapering solutions for different initial energies are shown together.

increasing from 1.8 to 10.3.

It is possible to vary the gap along the undulator proportionally to the laser waist profile instead of keeping it constant. The narrower gap near the minimum laser waist increases the magnetic field amplitude right where the intensity of the laser is largest so a slightly higher final output energy is achieved. In order to account for the gap tapering in the tapering equations, we must modify them slightly.

$$\frac{d\lambda_u}{dz} = -\frac{8\pi K_l K \sin \psi_r + \lambda_u \frac{\partial K^2}{\partial g} \frac{dg}{dz}}{1 + K^2 + \lambda_u \frac{\partial K^2}{\partial \lambda_u}} \quad (3.2)$$

In Figure 3.2 we show the case of a constant 2.1 mm gap and the case where we vary the gap from 2.1 mm at the undulator’s entrance and exit to 0.61 mm in the middle of the undulator at the laser focus. In this case, the output energy and average accelerating gradient increase to 1.04 GeV and 0.94 GeV/m.

Smaller gaps and periods enable lower injection threshold energies. By placing the laser waist at the entrance of the undulator and gap-tapering, the smallest gap coincides with the lowest resonant energy, pushing the threshold for acceleration lower. We positioned the laser waist at the undulator entrance and varied the

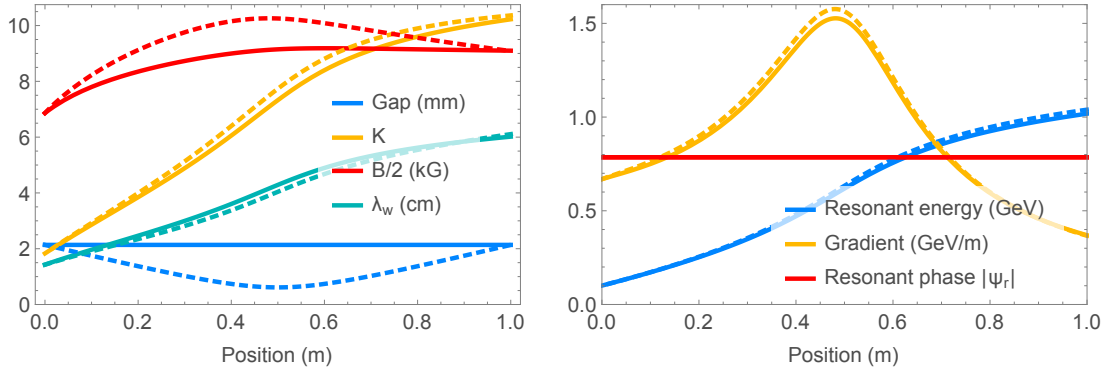


Figure 3.2: The tapering equations were solved for constant and variable gaps, shown as solid and dashed lines. Shown on the left are undulator parameters for the calculated tapers. Quantities associated with the dynamics for each undulator taper are displayed on the right.

input energies to find reasonable injection energy thresholds, defined here as the input energy which returns 90% of the maximum average gradient (for example, the reasonable injection energy threshold for the gradient versus input energy curve of Figure 3.1 is 15 MeV). The undulator length and Rayleigh range was halved for each subsequent scan in order to reduce the gap at the entrance. The results of the scan are summarized in Table 3.2. By reducing the Rayleigh range to 1.7 cm and gap to 220  $\mu\text{m}$ , the input energy may be reduced to 6 MeV. Novel technologies are needed in order to realize this undulator however. The permanent magnet residual field used in these calculations is 1.22 T, yet the undulator period needed is so small (also 220  $\mu\text{m}$ ) that micro-fabrication techniques are needed [46, 47]. Furthermore, the emittance needed to fit the beta-matched beam well within the laser waist at the entrance is 20 nm; alternatively, strong focusing may be used to match the beam size to the laser waist at the entrance.

<b>Input</b>				
Undulator length $L_u$ (cm)	100	50	25	12.5
Rayleigh range $z_r$ (cm)	15	7.5	3.75	1.73
Magnet gap $g$ ( $\mu\text{m}$ )	610	430	310	220
Threshold energy $\gamma_0 mc^2$ (MeV)	10	9	7.5	6
<b>Output</b>				
Output energy $\gamma_f mc^2$ (MeV)	700	530	410	270
Average gradient $\langle d\gamma/dz \rangle mc^2$ (GeV/m)	0.68	1.05	1.55	2.05

Table 3.2: Injection thresholds for entrance positioned laser waist

### 3.3 1D simulations with constant resonant phase

The undulator taper calculation determines the evolution of the dynamical quantities  $\psi_r$  and  $\gamma_r$ , and the properties of the ponderomotive bucket. In order to investigate the longitudinal dynamics, we can solve the 1D equations of motion (Equations 2.16 and 2.23) for an ensemble of particles with the constant gap undulator taper and design parameters listed in Table 3.2. First let's investigate the case of an input e-beam uniformly distributed in phase and normally distributed in energy with a relative energy spread of 0.1%. The resulting longitudinal phase space of the simulated output beam is shown in Figure 3.3. The accelerated bunch is clearly separated from the background and has a mean energy of 1,016 MeV with a relative energy spread of 0.89%.

#### 3.3.1 Capture estimates

Recall that for e-beams with energy spread small compared to the ponderomotive bucket height, the fraction of injected particles trapped within the bucket is expected to be equal to the fractional width of the bucket  $\Delta\psi/2\pi$  given by Equation 2.36. For a resonant phase of  $-\pi/4$ , this yields a prediction of 38%. Solving

the system numerically, we find that the fraction accelerated to full energy is indeed 38%.

While usually not desirable, certain circumstances may require injecting a beam with a large energy spread, comparable to the bucket height. Another estimation made in the previous chapter was that the fraction accelerated of an unbunched beam with energies uniformly distributed between the extremes of the separatrix should be equal to  $|\int_{\psi_1}^{\psi_2} d\psi \eta_{\text{sep}}(\psi)|/2\pi\eta_{\text{sep,max}}$  where  $\eta_{\text{sep,max}} = \eta_{\text{sep}}(\psi_r)$ . For a resonant phase of  $\psi_r = -\pi/4$ , this predicts that merely 27% of the injected beam should be captured. Figure 3.3 shows the results of a simulation for our standard taper but with an injected beam uniformly distributed in phase and energy up to the bucket height  $\eta_{\text{sep}}(-\pi/4) = \pm 0.08$ . The average energy of the accelerated beam is 1,017 MeV, and this time, the energy spread is 1.05%. While only a quarter of the beam initially fits within the ponderomotive bucket, the actual fraction of beam captured is 36%—nearly the same as the low energy spread case.

The discrepancy can be explained by the fact that the bucket height rapidly grows at the entrance of the undulator. Particles to the left of the bucket accelerate and slip right while particles right of the bucket decelerate and slip back left towards the bucket. The resonant phase remains constant so the bucket width is fixed, but if the height of the bucket grows fast enough, particles which have slipped towards the resonant phase become entrained within the bucket and remain trapped. Thus, the IFEL may be a reasonably robust accelerator for e-beam sources with relatively large input energy spread or jitter less than  $\eta_{\text{sep}}(\psi_r)$ . On the other hand when the resonant phase is varied to keep the bucket area constant (see the next section on constant action tapering), the bucket height remains nearly constant, and the fraction captured becomes 26% which agrees well with the 27% capture estimate for large energy spread.

In order to effectively improve the efficiency of the interaction, we must prop-

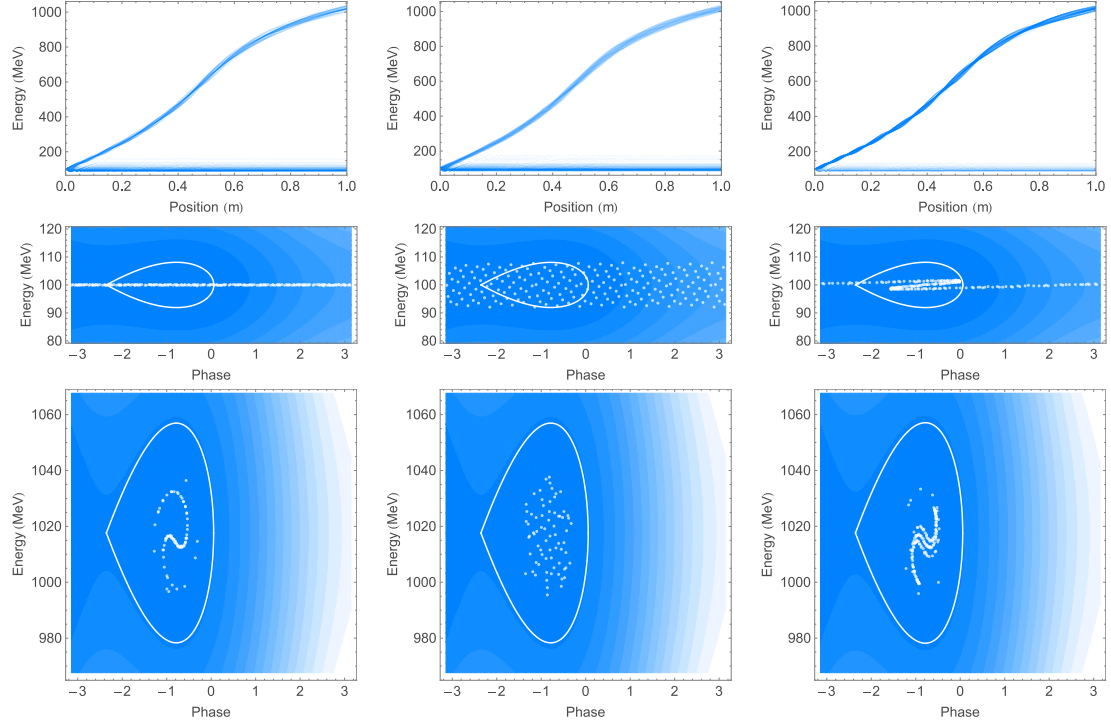


Figure 3.3: The 1D equations of motion were solved for a few example input distributions to assess the longitudinal dynamics of the constant gap solution from the previous section. Columns from right to left differ as follows: left, input beam in uniformly distributed in phase and normally distributed in energy with a relative energy spread 0.001, much smaller than the bucket height; middle, energy distribution is uniform and extends to the extrema of the bucket ( $\Delta\eta = \pm 0.081$ ); and right, the injected beam is prebunched with a bunching factor of 0.54 calculated to fit  $\sim 76\%$  of the beam within the bucket and uniform energy distribution half of the bucket height to represent energy spread from a prebunched beam. The white curves show the separatrix bounding regions of stable acceleration.

erly match the input phase space to the accelerator’s acceptance—that is, the region of phase space where particles are captured and accelerated to full energy.

### 3.3.2 Prebunching to improve capture

In practice, the electron beam phase space can be shaped to match the accelerating bucket by prebunching. Typically, an initially uniform-phase electron beam is injected into a ponderomotive bucket with a resonant phase of zero, acquiring a sinusoidal energy modulation. If left long enough to rotate a quarter synchrotron oscillation, the particles become condensed at zero phase. Stopping the interaction well before a quarter synchrotron oscillation and using the  $R_{56}$  of a magnetic chicane to convert the energy modulation to a density modulation yields a similarly bunched phase space, but with a small final energy spread. A measure of the phase space density is the rms longitudinal emittance, or phase space area occupied by the beam, and is  $\epsilon_{\zeta,\text{rms}} \approx \frac{\lambda}{2\pi} \sqrt{\sigma_{\psi}^2 \sigma_{\eta}^2 - \sigma_{\psi\eta}^2}$  [32]. Note that this is not the full longitudinal emittance of the beam, but the ‘slice’ emittance where the length of a slice is equal to the laser period. All the slices will behave very similarly assuming that the laser pulse and the beam are much longer than a single laser cycle. Multiplying the emittance by the beam mean energy yields the normalized emittance  $\epsilon_{\zeta,n} = \langle \gamma \rangle \epsilon_{\zeta}$ . The rms emittance is a useful quantity to calculate, but the area of phase space it represents holds about 15% of the particles. Assuming an uncorrelated bivariate normal distribution, the area containing a fraction  $f$  of particles is given by  $\epsilon_{\zeta,f} = -2\pi\epsilon_{\zeta,\text{rms}} \ln(1-f)$ ; consequently, the effective area of phase space occupied by 63% of the beam is about  $2\pi$  times the rms emittance. We will exclusively use this area, hereafter referred to as simply the normalized longitudinal emittance  $\epsilon_{\zeta,n}$  defined in Equation 3.3, since it is useful for direct comparisons to the ponderomotive bucket area.

$$\epsilon_{\zeta,n} \equiv \langle \gamma \rangle \lambda \sqrt{\sigma_{\psi}^2 \sigma_{\eta}^2 - \sigma_{\psi\eta}^2} \quad (3.3)$$

Returning to Figure 3.3, we examine the case of injecting a prebunched beam into the accelerating bucket. Approximating the beam's phase distribution as a Gaussian, we may use the Equation 2.47 to estimate that a modest bunching factor of 0.58 is needed to fit 3/4 of the particles within the bucket width  $\Delta\psi(-\pi/4)$ . Realizing this bunching, we may first apply a small (1.5 MeV) amplitude sinusoidal energy modulation with a short undulator section and then apply  $R_{56}$  to maximize the fraction of beam which fits within the initial separatrix when centered on the resonant phase  $\psi_r = -\pi/4$ . The resulting beam has a bunching factor of 0.54 and 76% of the beam is calculated to fit within the initial bucket. In this case, 78% of the particles are accelerated to an average energy of 1015 MeV and 0.75% rms energy spread.

The prebunched beam's normalized longitudinal emittance of 0.91  $\mu\text{m}$  is significantly larger than that of the unbunched low energy spread case of 0.11  $\mu\text{m}$ , but despite the lower phase space density, the bunched particles are well positioned within the separatrix leading to significant capture. Another benefit of concentrating the input phase space towards the middle of the bucket is that since the forces are more approximately linear there, the output emittance of the initially prebunched beam (2.1  $\mu\text{m}$ ) is smaller than that of the unbunched beam (3.0  $\mu\text{m}$ ).

### 3.4 1D simulations with constant action tapering

We owe a certain amount of gratitude for the expanding bucket, yet the fact that it grows as the beam's longitudinal emittance shrinks implies a lot of unoccupied phase space real estate. Instead, we could imagine injecting an unbunched beam at zero resonant phase for full capture and changing the width of the bucket as its height grows to keep its area constant. In this way, the entire unbunched beam may be accelerated. This may be accomplished by varying the resonant phase according to Equation 2.45 as discussed in the previous chapter. Figure 3.4 shows

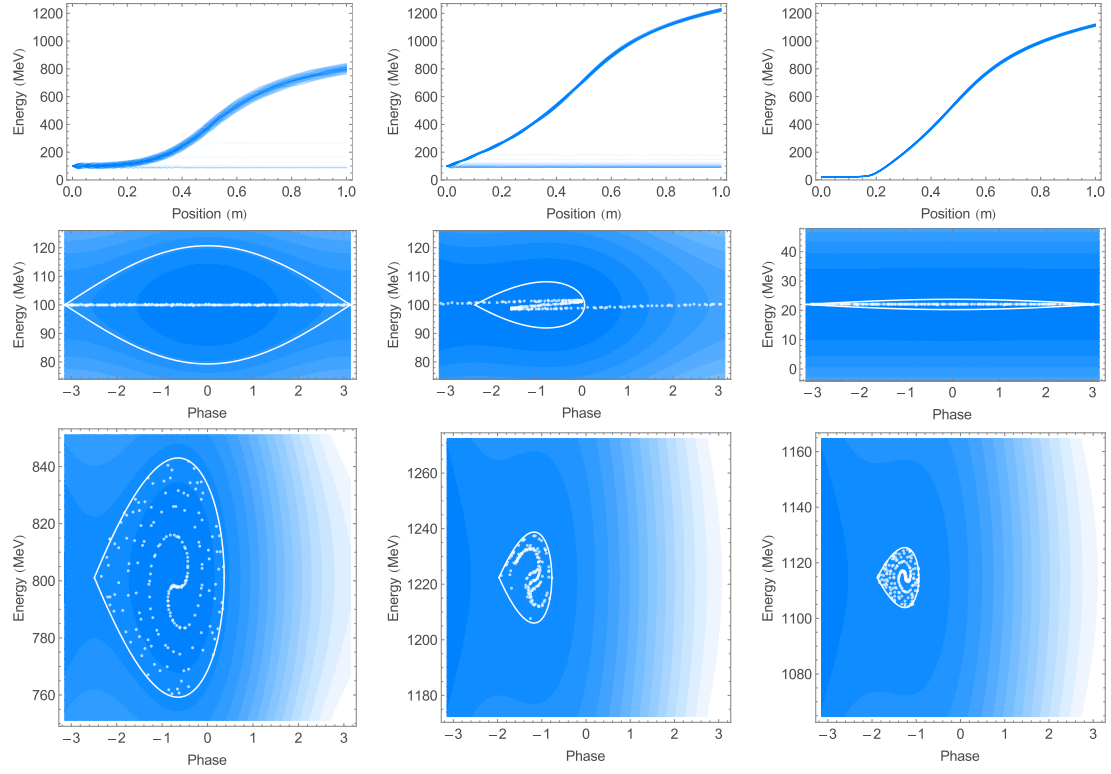


Figure 3.4: 1D simulations for constant 2.1 mm gap undulators conserving bucket action throughout the interaction. Left: Nearly an entire unbunched beam is accelerated to 799 MeV when injected into a bucket with initially zero resonant phase. Middle: 77% of a beam with initial bunching factor 0.825 and energy spread  $|\eta| < 0.04$  is accelerated to 1.22 GeV. Right: The entirety of an unbunched beam injected into a  $\psi_{r,0} = 0$  bucket with initial energy 22 MeV is accelerated to 1.11 GeV.

the results of a simulation for an unbunched beam with 0.1% rms energy spread injected into a bucket initially at  $\psi_{r,0} = 0$ . Virtually the entire beam (>94%) is captured and accelerated to 799 MeV with an output energy spread of 2.4% and bunching factor of 0.82. The large energy spread is due to the fact that in order to capture all of the unbunched beam, we used a large bucket area starting with  $\psi_r = 0$ . Unfortunately, the nonlinear forces within the bucket twist and distort the phase space, resulting in the relatively large energy spread and causing the normalized longitudinal emittance to grow from 0.28 to 18  $\mu\text{m}$ .

We can mitigate phase space dilution in two ways: match the input phase space to the separatrix or the reverse. Returning to Figure 3.4, the middle column shows the results of a simulation with a beam prepared to roughly match the bucket. The input prebunched beam is the same as used in the earlier prebunched example: mean energy of 100 MeV and phase locked to the bucket's center ( $\psi_{r,0} = -\pi/4$ ) with a bunching factor 0.54 estimated via Equation 2.46 to yield 72% capture. Adapting  $\psi_r$  to keep the area of the bucket constant yields a 1,225 MeV beam with 77% of the charge captured and rms energy spread of 0.56%. The initially 0.91  $\mu\text{m}$  normalized emittance beam is only diluted to 2.4  $\mu\text{m}$ . Comparing this with the previous result of injecting the same prebunched beam into a bucket with constant resonant phase  $-\pi/4$ , the normalized emittances of the accelerated beams are almost the same.

Matching the beam's longitudinal phase space into a bucket with a larger initial  $|\psi_{r,0}|$  and then freezing the action offers larger gradients and output energies. The right plot in Figure 3.5 shows the bucket area and output energy for an initial resonant energy of 100 MeV and a range of initial resonant phases. Larger (negative) initial resonant phases lead to smaller buckets which allow the resonant phase to approach closer to  $-\pi/2$  throughout the interaction. An ancillary benefit is that larger accelerating gradients afforded by the tapers with larger  $|\psi_{r,0}|$  relax the laser energy requirement for acceleration by reducing the number of undulator

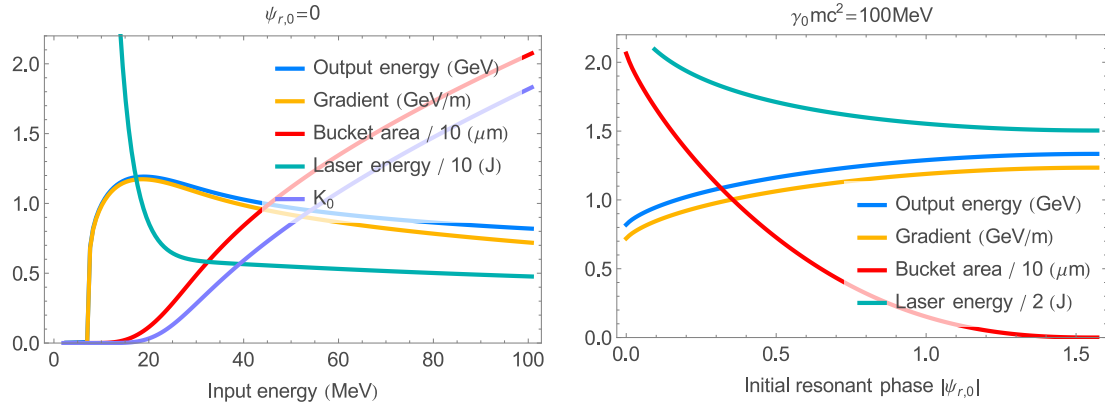


Figure 3.5: Constant bucket area undulator tapers vs input energy for initial resonant phase  $\psi_{r,0} = 0$  (left) and vs different initial resonant phases for initial resonant energy 100 MeV (right). The entire beam is captured for the former while the fraction captured for the latter case with initial bunching factor  $B_0$  is about  $\text{erf}(\Delta\psi(\psi_{r,0})/4\sqrt{-\ln B_0})$ .

periods and slippage length. On the other hand, a small bucket area requires the beam to be bunched without much dilution.

### 3.4.1 Adiabatic capture: low initial energy

Whereas prebunching the beam to fit well into a smaller accelerating bucket is one way to mitigate some longitudinal emittance growth, in practice prebunching with a simple undulator and chicane combination may leave some tails which may not fit into the subsequent accelerating bucket. Adiabatic prebunching with multiple undulator and chicane modules can overcome this problem at the expense of a longer bunching section and more laser slippage. Another way to capture the input electron beam is to initially reduce the bucket height to match an unbunched beam's energy spread and then adiabatically expand it. The height of the bucket scales as  $\eta_{\text{sep}} \propto \sqrt{K_l K / (1 + K^2)}$  so either the undulator or laser field may be manipulated to ramp up the coupling adiabatically.

For small  $K$ , the height of the bucket scales as  $\eta_{\text{sep}} \propto \sqrt{K_l K}$ . In order to decrease the initial  $K$  and therefore the initial bucket height, one solution is to inject at a low enough input resonant energy so that the initial bucket height is only slightly larger than the input electron beam's energy spread. The left plot in Figure 3.5 shows final energies for a variety of tapering solutions with a range of initial energies each holding the bucket area constant throughout the interaction. For lower energies near 20 MeV, the bucket area and  $K$  both approach zero. As a consequence of the small phase space area, the full beam is easily accelerated at large resonant phases to high energies. An exemplary simulation is shown in the right column of Figure 3.4 where a 22 MeV unbunched beam with 0.1% energy spread is injected into the accelerator. Virtually the entire beam (>97% is accelerated to 1.11 GeV with 0.43% energy spread and 28 nm rms bunch length, and the beam's normalized emittance, initially 0.06  $\mu\text{m}$ , is increased to 1.6  $\mu\text{m}$ . Again, achieving resonance with these low initial resonant energies requires novel undulator technologies ( $\sim 3$  mm period) or harmonic interactions. Another limitation is that as the ponderomotive gradient is reduced for very small  $K$ , the number of periods required to accelerate increases, increasing the slippage and therefore laser energy; nevertheless, for the example presented, the laser energy remains a finite (though certainly not cheap) 7 J. This laser energy was estimated by assuming a Gaussian pulse in time with a peak power twice the design and full width at half maximum duration set equal to the slippage.

### 3.4.2 Adiabatic capture: undulator field ramp

Injecting at low energies leads to small values of  $K$  and a small bucket height. One way to achieve resonance at higher energy while keeping a small  $K$  is to increase the period and maintain a small field on axis by enlarging the gap between magnets. Due to restrictions on the applicability of the gap to period ratio, this may not always be achievable (e.g. gaps large compared to the period). On the other hand,

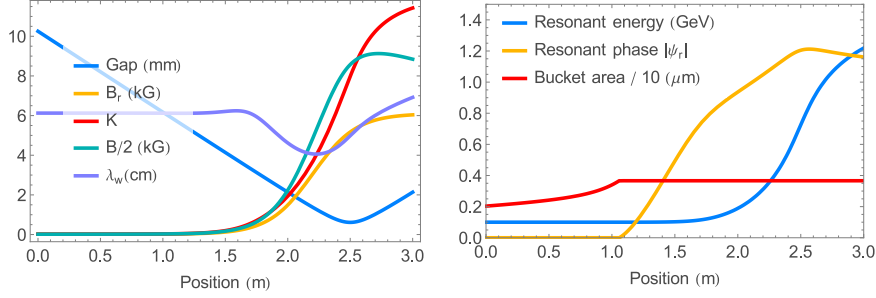


Figure 3.6: Plots showing the design of an accelerator with  $B_r$  assisted mildly diabatic capture. From left to right: normalized laser vector potential along the laser pulse at the laser waist; undulator parameters for the solved taper; and the energy evolution of 200 simulated particles along with quantities describing the dynamics along the interaction.

the magnetization of the magnets may be tailored to decrease the on-axis field independent of magnet gap. We will examine one such example in this subsection.

In order to factor in the effect of tapering the residual field  $B_r$ , we must add a term to the tapering equation as shown below.

$$\frac{d\lambda_u}{dz} = - \frac{8\pi K_l K \sin \psi_r + \lambda_u \left( \frac{\partial K^2}{\partial g} \frac{dg}{dz} + \frac{\partial K^2}{\partial B_r} \frac{dB_r}{dz} \right)}{1 + K^2 + \lambda_u \frac{\partial K^2}{\partial \lambda_u}} \quad (3.4)$$

Figure 3.6 shows the result of an undulator taper with residual magnetization shown in yellow. The expression for the residual magnetization is a sigmoid with an amplitude of 1.22 T and a characteristic length of 55 cm centered 220 cm into the undulator. While not strictly adhering to the adiabatic condition (Equation 2.39), this functional form of the magnets' residual field works reasonably well in a relatively shorter space. In practice, the residual field may be changed in sections along the gap undulator and the gap may be adjusted to compensate. For the first half of the undulator where the fields are less than 1 kG, an electromagnetic undulator may be cheaper and more practical to employ.

The gap of the undulator was chosen to be  $\pi$  times the laser waist  $g = \pi w(z)$

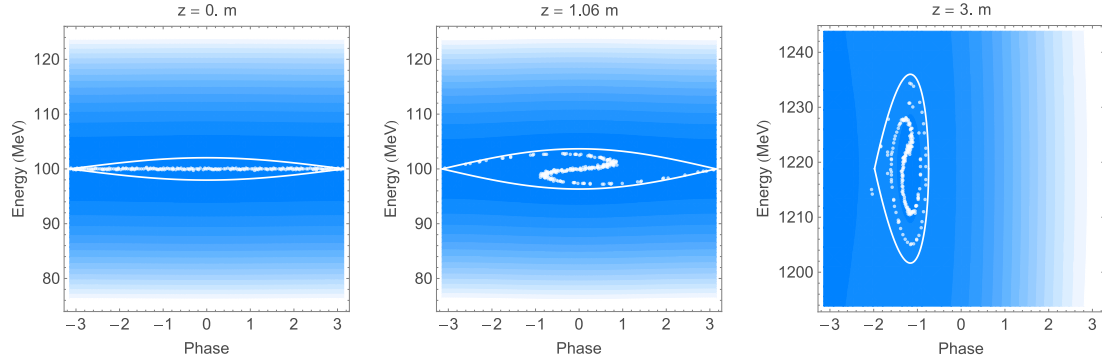


Figure 3.7: Phase space evolution for the residual magnetization tapering assisted capture and acceleration. On the left, the beam is injected into a bucket 1 m (6.7 Rayleigh ranges) upstream of the waist where the bucket is small. Middle: The bucket area is frozen after 45% of a synchrotron oscillation. Right: Nearly the entire beam is accelerated with moderate energy spread.

in order to allow the laser to clear. A larger gap may certainly be used throughout the undulator with the main consequence being a larger required residual magnetization. The solution for the undulator period, field, and  $K$  are also shown in the figure. The period starts at 6.1 cm to achieve resonance at 100 MeV for vanishingly small  $K$ . As the field increases near the 2 m point, the undulator period decreases in order to maintain resonance; however, once the particles begin to accelerate, both the period and  $K$  grow to increase the resonant energy.

We freeze the resonant phase at  $\psi_r = 0$  for the first meter (about half a synchrotron period) in order to allow for the beam to bunch with little energy spread. A chicane may be used to shorten this bunching section and possibly produce smaller energy spread beams. After the beam is bunched, the resonant phase is varied via Equation 2.45 to keep the action of the bucket a constant  $3.7 \mu\text{m}$ . The resulting final resonant energy is 1.22 GeV.

A 1D simulation with an initially unbunched e-beam with 0.1% rms energy spread is shown in Figure 3.7. 97% of the injected beam is captured and accel-

erated to the design energy with an rms energy spread of 0.17% and normalized longitudinal emittance of 0.16  $\mu\text{m}$ . The 53 total undulator periods necessitates at least a 2.8 J of laser energy at 20 TW. In practice, a Gaussian pulse of at least 60 fs full width at half maximum duration (plus enough to account for the e-beam and laser time of arrival jitter) and peak power of 40 TW yields a required laser pulse energy of at least 6 J.

### 3.4.3 Adiabatic capture: laser field ramp

The other approach to capturing an unbunched beam is to control the bucket height with the laser field. Since the height scales as  $\eta_{\text{sep}} \propto \sqrt{K_l}$ , one approach to this problem is to inject the beam with a small laser intensity and then ramp up the intensity over many synchrotron periods to slowly increase the bucket height. The most straight forward way of accomplishing this would be to adjust the focusing or add an additional undulator section before the main undulator. Assuming constant power, this unfortunately leads to a significant increase in the required laser pulse energy. As it turns out from the analysis below, taking advantage of the slippage effect might reduce such requirements.

We add the effect of slippage between the particles and the laser pulse by modeling the laser power as a Gaussian with peak power  $P_0$  and rms pulse duration  $\sigma_t = U_l/\sqrt{2\pi}P_0$  where  $U_l$  is the pulse energy.

$$P_l = P_0 e^{-\frac{1}{2}\left(\frac{s(z)-s_w}{c\sigma_t}\right)^2} \quad (3.5)$$

The constant  $s_w$  is a parameter ideally set to the slippage during the propagation from the entrance of the undulator to the laser waist  $s_w = s(z_w)$  to maximize the power seen near the waist. Resonance demands that the particles fall behind the laser by one ponderomotive wavelength every undulator period traversed. The slippage evolution is given by Equation 3.6.

$$\frac{ds}{dz} = -\frac{\lambda}{\lambda_u(z)} \quad (3.6)$$

In order to calculate the tapering, the equation for the power is substituted into the expression for the laser vector potential (Equation 2.13), and the tapering Equation 2.43 and slippage evolution are calculated with the the undulator builder Equation 2.44. The resulting solutions for  $\lambda_u(z)$  and  $s(z)$  determine the taper.

Again we turn to the problem of capturing an entire unbunched beam while maintaining phase space density. The bucket should initially maintain a constant resonant phase of zero until bunching is achieved. This distance can be calculated by integrating the spatial synchrotron frequency  $k_s$  (Equation 2.38) from the start of the undulator until a point that yields about a half synchrotron period. The bucket height at this point will set the scale of the energy spread of the beam. Note that we could insert a magnetic chicane to shorten this distance while at the same time obtaining a smaller energy spread. Finally, the bucket area is frozen by varying the resonant phase with Equation 2.45, taking the parameters at this point for the initial parameters in the equation.

As an example, we use our standard parameters from Table 3.2 with the addition of  $s_0 = 125$  fs and  $U_l = 1.5$  J. For 20 TW peak power, we have  $\sigma_t = 30$  fs. 50 cm have been added to the beginning of the undulator for the capture, and the laser waist is located 1 m from the beginning of the capture section. The left plot in Figure 3.8 shows  $K_l$  the instantaneous  $K_l$  felt by the particle throughout the interaction.

In order to simulate the particles' phase space trajectories, we again substitute the expression for  $P_l$  for  $P_0$  in  $K_l$  and replace it in the equations of motion (Equations 2.16 and 2.23). In order to allow each  $i^{\text{th}}$  particle to slip independently, we add its ponderomotive phase to its respective slippage coordinate  $s_i = s(z) + \lambda\psi_i/2\pi$ . The temporal envelope of the beam may then be calculated

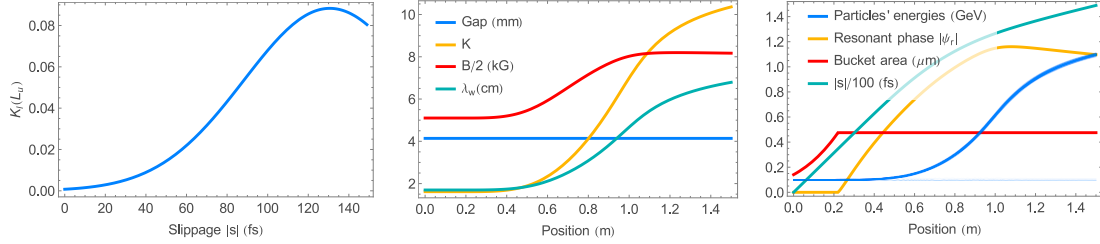


Figure 3.8: Plots showing the design of an accelerator with slippage assisted mildly diabatic capture. From left to right: normalized laser vector potential along the laser pulse at the laser waist; undulator parameters for the solved taper; and the energy evolution of 200 simulated particles along with quantities describing the dynamics along the interaction.

from the distribution of initial phases.

When a short, unbunched e-beam with 0.1% rms energy spread is injected into the accelerator, nearly the entire beam (99%) is accelerated to a mean energy of 1.1 GeV with an rms energy spread of 0.15%—slightly larger than the input beam—as shown on the right side of Figure 3.8. On the other hand, the normalized longitudinal emittance is preserved at 280 nm. Examining the phase space, we can see the capture process. At  $z=0$ , the particles are injected into the small bucket. After the designed 40% synchrotron rotation at  $z=21$  cm, the bucket area is frozen and the resonant phase begins to increase and is accelerated through the end. It is important to note that these simulations assume that the input e-beam bunch duration is small compared to that of the laser so that the laser field strength felt by the bunch is uniform. This scheme may be improved by applying  $R_{56}$  during the capture section in order to hasten the rotation and bunching with reduced energy modulation. The reduced energy modulation would reduce the required bucket area, enabling larger accelerating gradients throughout the interaction.

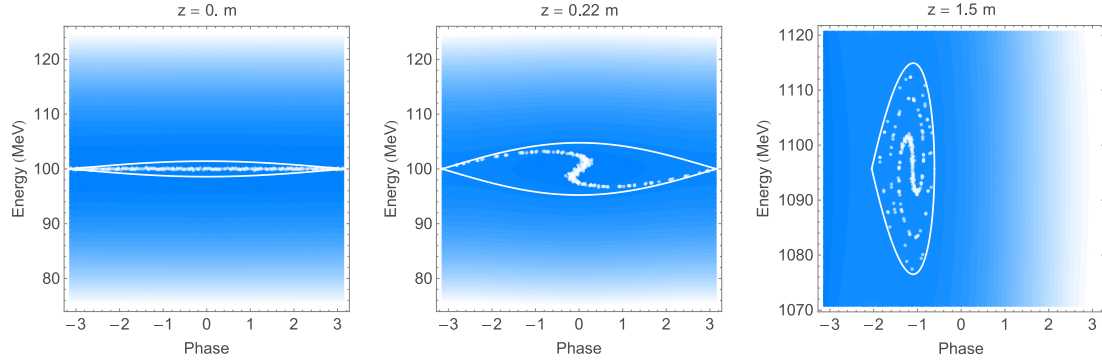


Figure 3.9: Phase space evolution for the slippage assisted capture and acceleration. On the left, the beam is injected into a bucket 1 m (6.7 Rayleigh ranges) upstream of the waist where the bucket is small. Middle: After 40% of a synchrotron oscillation, the bucket area is frozen. Right: The entire beam is accelerated with moderate energy spread.

### 3.5 Beam loading

In the description of the IFEL interaction, we have so far considered the electromagnetic radiation as an externally given function rather than as a dynamical variable of the system. This greatly simplifies the modeling of IFEL's and is a very good approximation as long as the accelerated charge is maintained low enough so that effects of beam loading or pump depletion can be neglected. In this section we will analyze the situation when this assumption is no longer valid.

In order to assess the limit of validity of this assumption, it is instructive to look at the energy balance in the system. The energy required to accelerate 1 pC of beam charge to 1 GeV is 1 mJ. This amount of energy needs to be transferred from the laser beam to the electrons. When the fraction of energy absorbed by the beam is significant with respect to the total laser pulse energy, the IFEL dynamics will be affected by the loading of the accelerating gradient from the beam of the accelerating waves.

It is useful to consider a different point of view which gives insight on the

mechanism of energy transfer in the undulator. A microbunched electron beam of 1 pC of charge would emit 1 mJ of coherent radiation at the resonant wavelength when traveling through the IFEL undulator. This radiation is emitted at the resonant wavelength of the undulator but at a phase opposite to the driver laser so that the fields cancel and the radiation effectively loses energy.

To describe in a quantitative way the beam loading in an IFEL accelerator, we need to solve the Maxwell equation for the electromagnetic field in presence of a source term factoring in the beam current. The equations are exactly the same as the FEL equations, and we can rely on an ample literature of algorithms and codes which have been developed through the years and already well benchmarked with experiments by the FEL community.

For full three dimensional simulations of the evolution of both the beam as well as the radiation in an IFEL accelerator, we adapted one of the most used and benchmarked FEL simulation code publicly available, Genesis [48]. The code solves the period averaged equation of motion for the particles and the radiation field equation in the slow-varying envelope approximation. The equation for the longitudinal space charge force electric field can also be solved. Unfortunately Genesis cannot be directly used to simulate IFEL accelerators since the undulator period can not be arbitrarily changed throughout the simulation, and the only undulator tapering implemented in the standard version of the code is a linear or quadratic variation in the magnetic field amplitude.

On the other hand, tapered undulators are typically designed and built in a piecewise fashion so each period has a fixed length. Using a simple script to process the input and output files, we devised a new approach to simulate the IFEL interaction. Therefore we can take advantage of Genesis options to exit and restart from a dump of the full 6D phase space of the particles and the radiation profiles at any given point (for example after every period).

The script we developed for self-consistent IFEL simulations requires as an

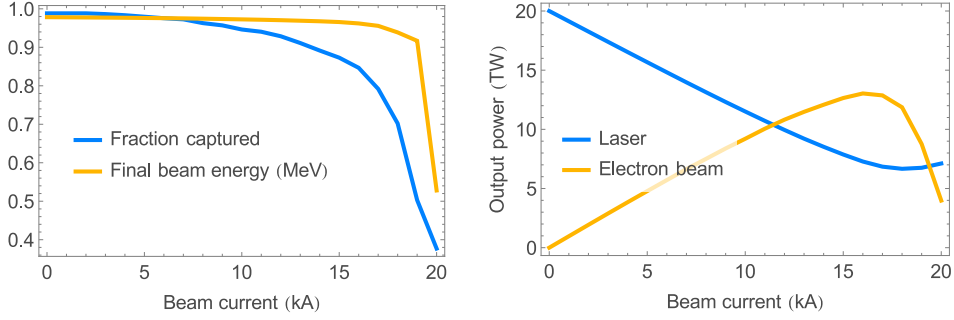


Figure 3.10: Output e-beam and laser parameters versus input peak current for an uncompensated undulator.

input file the tapered undulator data (period and amplitude vs. distance along the undulator). When launched, the code runs Genesis for the first undulator period asking for the full dumped beam and radiation record files. It then modifies the undulator parameters (period and  $K$ ) in the Genesis input file to take into account the tapering before launching the simulation for the second period. In order to properly follow the violent acceleration of the particles each period is simulated using more than 100 simulation steps. At the end of the second period we can reiterate this procedure and propagate the beam and the radiation through each segment sequentially. The simulations can also be run in time dependent mode to simulate the effect of the finite laser pulse width and the electron beam bunch length. In this case, the code shifts the radiation slices over the beam slices to take into account the slippage between each period.

With the development of this self-consistent simulation tool we can analyze the effects of beam loading in the GeV IFEL design discussed earlier. We take as a [reference](#) the undulator design with NdFeB magnets ( $B_r = 1.22\text{T}$ ), constant resonant phase  $\psi_r = -\pi/4$ , and a fixed gap. The undulator design consists of 26 periods with lengths increasing from 14 mm to 60 mm and  $K$  increasing from 1.8 to 10.3. Variations of the accelerator output parameters (final energy and fraction of trapped particles) as a function of input beam current for the case of a

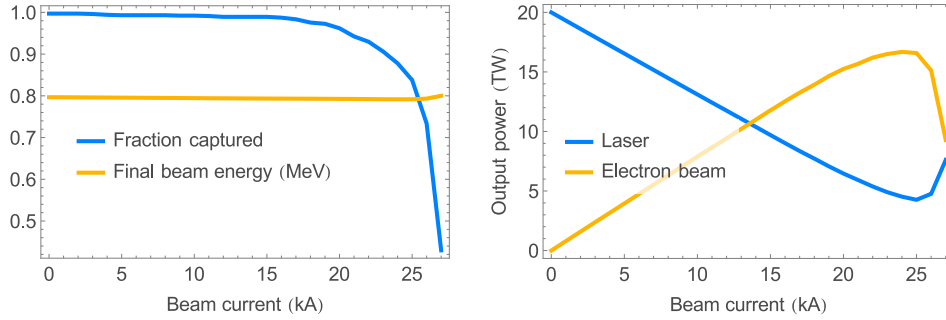


Figure 3.11: Output e-beam and laser parameters versus input peak current for a changing laser power compensated undulator taper design.

uniform and prebunched beams are shown in Figure 3.10. The final output laser and beam power is also shown.

For this example, the final energy of the IFEL does not vary much with beam current since this quantity is determined by the choice of the undulator tapering and not by the dynamics of the system. Significant decrease in the fraction of accelerated particles only starts to happen for very large currents ( $>10$  kA). A reference point is obtained observing that the power required to accelerate 20 kA of particles to 1 GeV would be 20 TW, or the full laser power. It is also important to notice that the beam loading is dependent on the bunching factor of the injected beam. If the beam is microbunched, the fraction of trapped particles is much larger and the current where the effects of beam loading occur is lower.

For larger beam currents such as those greater than 18 kA in Figure 3.10, the laser loses too much energy along the undulator and the ponderomotive accelerating gradient decreases. The consequence is that the electrons are no longer able to follow the design resonant tapering trajectory and particle detrapping from the stable potential bucket occurs.

Using a simple 1D model, it is possible to optimize the IFEL tapering to take into account the depletion of the IFEL driver and adjust the variation of period and magnetic field amplitude to compensate for the losses in laser power and

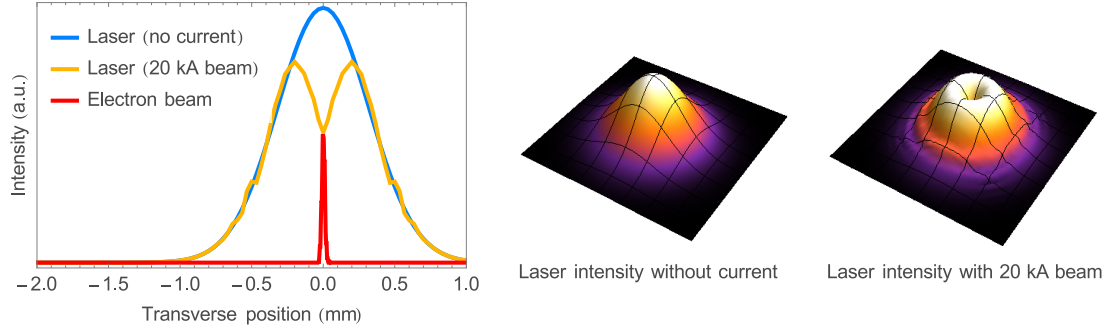


Figure 3.12: A dense electron beam erodes a hole in the laser intensity as it transfers power.

minimize detrapping. We can estimate the laser power absorbed in the IFEL when we inject in the accelerator an electron beam of current  $I$  since the energy gain is set by the resonance condition

$$\begin{aligned}
 P_{abs}(z) &= \eta I m_0 c^2 (\gamma(z) - \gamma_0) \\
 &= \eta I m_0 c^2 (\sqrt{\lambda_w(z)(1 + K(z)^2)/2\lambda} - \gamma_0)
 \end{aligned}
 \tag{3.7}$$

where  $\eta$  is the fraction of particles trapped in the ponderomotive bucket.

By scaling the laser electric field in Equation 2.43 as

$$K_l(z) = K_l(z) \sqrt{\frac{P - P_{abs}(z)}{P}}
 \tag{3.8}$$

where  $P$  is the input laser power, we can find the optimum tapering for a loaded IFEL.

In practice, this compensation is not perfect as it assumes that only the trapped particles change energy, and it completely neglects important effects such as harmonic emission, slippage and three dimensional effects. Nevertheless, by using the compensated tapered undulator obtained with this procedure, we obtain an IFEL design with  $>70\%$  efficiency which is a respectable number for a laser accelerator, quite comparable with the typical efficiency of RF accelerating structures. The result of the simulation are shown in Figure 3.11. Again we see a nearly constant

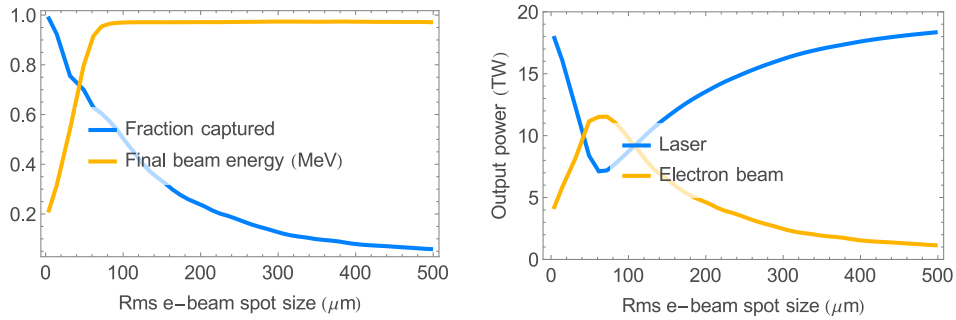


Figure 3.13: Output e-beam and laser parameters versus input e-beam rms spot size, scaling the emittance to keep the divergence constant, for a standard, uncompensated undulator taper design.

final energy for various beam currents; however this time, the relaxed tapering towards the undulator’s exit allows for acceleration of a larger beam current.

One of the major limitations to the efficiency comes from the fact that the electron beam has a much smaller transverse size than the laser beam in order to experience a nearly constant accelerating gradient. Due to this mismatch, the radiation is not absorbed homogeneously across its transverse cross section. The laser acquires a higher order transverse mode as it propagates while an intense electron beam basically burns a hole in the center (see Figure 3.12).

In order to achieve maximal power transfer one must strike a balance between electron and laser beam sizes. Figure 3.13 shows the performance of the earlier discussed accelerator with uncompensated tapering design as the electron beam size is varied. In order to reduce the effects of increased divergence, the emittance was scaled to maintain a constant spot size for each point in the scan. As the beam is made small, the current density explodes, and the power absorbed quickly depletes the on-axis laser intensity. The interaction is halted, despite the on-axis intensity later being replenished by power in the tails, as the ponderomotive gradient becomes insufficient to continue accelerating a significant fraction of particles. Large e-beam sizes cause degradation due to the low intensity off axis there. A

compromise is found by balancing tradeoffs for an intermediate sized beam.

In recirculating laser schemes where in order to increase the efficiency the laser power is replenished by a laser amplifier, it will be important to introduce optical elements in the recirculating cavity to restore the transverse profile before reusing the power for IFEL acceleration.

## CHAPTER 4

### Experimental design and setup

The experiment detailed in this dissertation was designed to achieve energy gain and accelerating gradient significantly larger than what is possible with conventional RF accelerator technology to pave the way for applications such as portable drivers for inverse Compton sources and FELs [49]. The experiment was conceived to bring together the two major groups active in IFEL research, combining ATFs electron beam and high power CO<sub>2</sub> laser system with a strongly tapered helical permanent magnet undulator designed and built at UCLA to achieve high gradient acceleration and significant energy gain. Previous IFEL experiments at Brookhaven National Laboratory's Accelerator Test Facility (ATF) [23] successfully demonstrated staging and narrow energy spread while the UCLA Neptune IFEL experiment achieved high gradient acceleration in excess of 70 MeV/m [24].

This chapter presents an overview of the experimental design and setup. We first discuss the design parameters. When designing a new experiment, it is often tempting to push the designed performance to the limits of possibility. A hard lesson learned was that pushing those limits also reduces the chance of success, especially when designing an experiment for a remote facility where beam time is scarce and must be used wisely. Unexpected deviations in some parameters necessitated a second undulator tune optimized for high capture. Consequently, two undulator configurations are presented for two subsequent experiments: the first tune was designed for high energy acceleration while the second was designed for high capture.

After discussion of the undulator design, construction, and measurements, we introduce the design of a prebuncher for a subsequent experimental run with the aim of significantly increasing the fraction captured. Finally, we introduce the ATF linac and CO<sub>2</sub> laser system, and discuss electron beam and laser transport and diagnostics.

## 4.1 Design parameters

The stated experimental goal was to achieve significant acceleration within a meter-scale IFEL by utilizing modest investment and available resources. The Brookhaven ATF is perfectly suited for this experiment as it has a linac capable of producing stable, high-quality beams and a CO<sub>2</sub> laser capable of producing terawatt peak powers. A summary of the initial undulator design parameters is shown in Table 4.1.

<b>Parameter</b>	
E-beam energy	50 MeV
Laser wavelength	10.6 $\mu\text{m}$
Laser peak power	450 GW
Laser waist	0.25 m
Laser Rayleigh range	9.6 cm
Undulator length	$\sim 50$ cm
Magnetization	1.22 T
Resonant phase	$\pi/4$

Table 4.1: Experimental design parameters

The linac at ATF produces stable beams with controlled emittance for energies between 45 and 70 MeV. The input energy for the experiment was chosen to be 50 MeV, to allow for stable, low emittance operation and to allow for significant

acceleration before hitting the radiation shielding limit of the ATF experimental hall at 120 MeV. In order to account for a finite output energy spread of the beam (which may be as large as the ponderomotive bucket height of several MeV), the accelerator resonant energy output was chosen to be around 115 MeV. The undulator length was chosen to be half of a meter for compactness and in order to achieve  $\sim 120$  MeV/m accelerating gradients—competitive with state of the art x-band RF accelerating cavities.

The peak power of the ATF’s CO<sub>2</sub> laser system at the time of the experiment was roughly 1 TW [50]. Since having a larger than design laser power relaxes alignment and timing tolerances so the undulator tapering was designed assuming a peak laser power of 450 GW in order to account for expected large variances in laser power and ensure successful operation. Furthermore, the transverse laser mode quality parameter  $M^2$  was assumed to be 1.5 to take into account the flatness of the laser spatial profile coming out of the amplifier. In the previous chapter, we saw that the average accelerating gradient using a TEM<sub>00</sub> mode Gaussian laser is maximized when the laser’s waist is placed near the center of the undulator and the Rayleigh range is chosen to be about 1/5 of the undulator length. With these considerations in mind, the experiment’s Rayleigh range was chosen to be 9.6 cm. Virtually all of the laser power is contained within three times the laser waist which in this case is 4.5 mm at the undulator’s ends. This value set the aperture of the vacuum chamber inside the undulator to  $>13$  mm.

A final consideration is the peak current of the accelerating e-beam which is typically 100 A without compression at the ATF. If the power transferred from the drive laser to the accelerating e-beam is significant, the available laser power will decrease along the interaction and may need to be compensated in the tapering equations. For a conservative estimate, we may assume that the entire e-beam is accelerated during the process. The power transferred from the laser to the electrons is the product of the e-beam current and change in energy per elementary

charge or about 6 GW. This estimated upper bound is about 1% of the expected peak laser power and therefore negligible.

There are many creative possibilities for undulator design: permanent magnet undulators, electrostatic undulators, electromagnet undulators, radio frequency undulators, and laser undulators for some examples. Electrostatic undulators, while attractive due to ease of construction and tuning, suffer from breakdown limits limiting their peak field strength and coupling factor. Electromagnetic undulators offer similar benefits as electrostatic undulators but without the breakdown, yet they require a multitude of power supplies to tune easily and care must be made to avoid field saturation within each yoke. Radiofrequency undulators may offer large fields and short periods but are current avenues of research, expensive, and may be hard to taper. Laser undulators are conceivable but require expensive lasers, which nonetheless produce field strengths which jitter too much for stable resonance, and wavelengths not suited for operation at 50 MeV.

The permanent magnet undulator [51] is a natural choice for IFEL design as it is cost effective, has a stable field with strengths approaching 1 T on axis, and gives fine control to the field and period tapering along the undulator. The next question is then whether to taper the period, the field, or both. Recall that the on-axis field strength is related to the period and gap by an undulator builder equation. If the period is kept constant, the gap would have to decrease along the undulator in order to increase the on-axis field and resonant energy. This choice would limit the final resonant energy, change rapidly the focusing of the undulator, and introduce problems with wakefields if the gap becomes too small. A reasonable choice then is to keep the gap constant and take advantage of the increase of field and undulator parameter  $K$  as the period grows to ease the physical design and construction of the undulator.

## 4.2 Tapered helical undulator

To design the undulator we follow the steps for the constant gap and resonant phase outlined in the [1 GeV example](#) in the previous chapter using the parameters available for the experiment. A necessary modification to the design laser focusing decreased the efficiency of the experiment with the original undulator tapering design so for a second experimental run, we designed a second taper by varying the magnetic gap to manipulate  $K$  throughout the undulator for increased beam capture efficiency at the expense of some energy gain. Consequently throughout this section, we will discuss magnetic and mechanical design, construction, and measurement for the two undulator tapers, referring to the first as “high gradient” and the second as “high capture”.

### 4.2.1 High gradient taper design

The undulator tapering Equation [2.43](#) along with the undulator builder equation [2.44](#) and the design parameters listed in Table [4.1](#) determine the undulator tapering. The only free parameter in the design is the choice of the resonant phase to determine the final energy and fraction of electrons accelerated to full energy. For this experiment, we chose a resonant phase of  $-\pi/4$  as a reasonable compromise between the accelerating gradient and fraction captured since the resonant particle still accelerates at  $\sin \pi/4 \approx 70\%$  of the maximum possible gradient and the phase width of the bucket is relatively large. The solution to the equations with the design parameters is shown in Figure [4.1](#).

The 1D equations of motion (Equations [2.16](#) and [2.23](#)) with the design parameters and undulator  $K$  and wavelength profiles shown in Figure [4.1](#) were then solved with an ensemble of longitudinal particle coordinates  $\psi$  and  $\gamma$  to simulate the output beam phase space. The input particle phases was uniformly distributed over the interval 0 to  $2\pi$  while their energies were normally distributed around

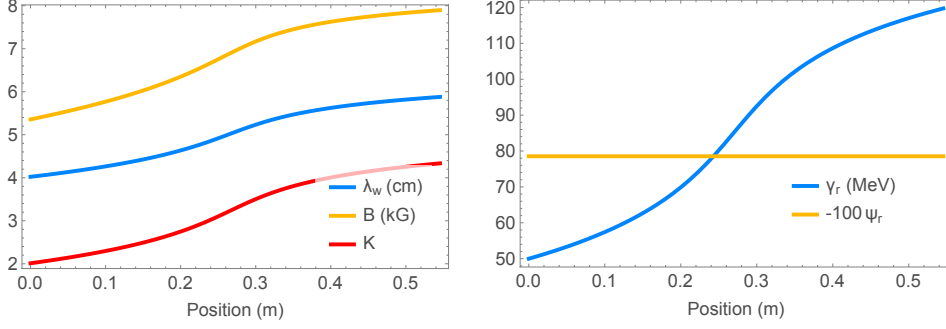


Figure 4.1: The Rubicon design tapering is the solution of the tapering equations and the design parameters listed in Table 4.1.

<b>Parameter</b>	
Number of periods	11
Total length	54 cm
Wavelength $\lambda_u$	4.00 $\rightarrow$ 5.93 cm
Field	5.4 kG $\rightarrow$ 7.4 kG
Undulator $K$	2.0 $\rightarrow$ 4.2
Resonant energy	50 $\rightarrow$ 115 MeV

Table 4.2: High gradient run undulator parameters

the input resonant energy of 50 MeV with an rms width of 0.15%. The particle coordinates at the end of the undulator revealed that as much as 50% of the beam should be accelerated from 50 to 115 MeV with an rms energy spread of 1.4% and a bunching factor of 0.9 for the accelerated fraction of the beam. As a first look, this performance is promising, but the 1D model ignores transverse dynamics and assumes a continuous change for the undulator parameters.

In anticipation of constructing the mechanical undulator, we discretized the period. This was done by sampling the first period  $\lambda_{w,0} = \lambda_w(0)$ , and then sampling subsequent periods as  $\lambda_{w,n} = \lambda_w(z_n)$  with  $z_n = \sum_{i=0}^{n-1} \lambda_{w,i}$  for  $z_n < 0.5$  m. The net result is 11 periods spanning a total length of 54 cm. The effect of the period discretization will be taken into account later in this section but will

ultimately be shown to not significantly effect the performance.

### 4.2.2 High capture taper design

As we will discuss in the [following chapter](#) the best experimental result obtained with the design tapering was the acceleration of 52 MeV electrons up to 106 MeV [52]. Not only the highest energies observed fell short of expectation by at least 10 MeV, but also the accelerated spectra had such large energy spreads that it was difficult to imagine the accelerator producing anything close to a monoenergetic beam. Obviously, these results dampen the attraction of the IFEL as a candidate for a future stable accelerator facility.

The dominant reason for the lackluster performance was a mismatch between design and experimental laser focusing. The undulator was originally designed for use with a 9.6 cm Rayleigh range CO<sub>2</sub> laser. Unfortunately after construction, it was discovered that beam line space constraints and a restricting dipole aperture just upstream of the undulator necessitated a laser Rayleigh range closer to 30 cm. While the increased Rayleigh range had the positive benefit of easing transverse overlap tolerances by increasing the laser spot size, it reduced the on-axis intensity threefold, thereby significantly limiting accelerating gradient where it was needed most. Consequently, the resonant fraction of the beam decreased dramatically near the center of the undulator.

In order to improve the efficiency of the interaction, either the laser focusing had to be changed to match the undulator design or the undulator tapering needed to be modified to match the laser. The former proved to be costly as the dipole gap would have to be increased and impractical since due to the experimental hall layout, the focusing optics would have to be placed in the middle of a walkway, blocking access to vacuum equipment and interlock systems. The solution chosen was to redesign and rebuild the undulator to accommodate the more relaxed laser

focusing.

Of course with the undulator already manufactured, the variation of the period along the undulator could not be altered. In order to relax the resonant energy gradient, we decided to vary the gap between opposing magnets within the undulator. This extra degree of freedom enabled us to change the undulator strength  $K$  while maintaining the same period tapering.

<b>Parameter</b>	<b>Value</b>
E-beam energy	50 MeV
Laser wavelength	10.3 $\mu\text{m}$
Laser focal intensity	4 TW/cm <sup>2</sup>
Resonant phase	$\pi/4$
Rayleigh range	25 cm
1/e <sup>2</sup> spot size	0.91 mm
M <sup>2</sup>	1.07
Laser waist position	undulator midpoint

Table 4.3: High capture run experimental design parameters

The undulator tapering is then determined by Equation 4.1 which is found by equating the ponderomotive gradient with the gradient in the resonant energy. When the undulator period and laser parameters are specified along with the initial condition that  $K$  at the entrance be such that the resonant energy is equal to the input beam's 50 MeV, the differential equation yields  $K$  which in turn determines the on-axis field strength along the undulator.

$$\frac{dK}{dz} = -\frac{8\pi K_l K \sin \psi_r + \frac{d\lambda_u}{dz} (1 + K^2)}{2\lambda_u K} \quad (4.1)$$

The undulator builder equation can then be used to estimate the gap along the undulator needed to create the designed on-axis field. In practice, 3D magne-

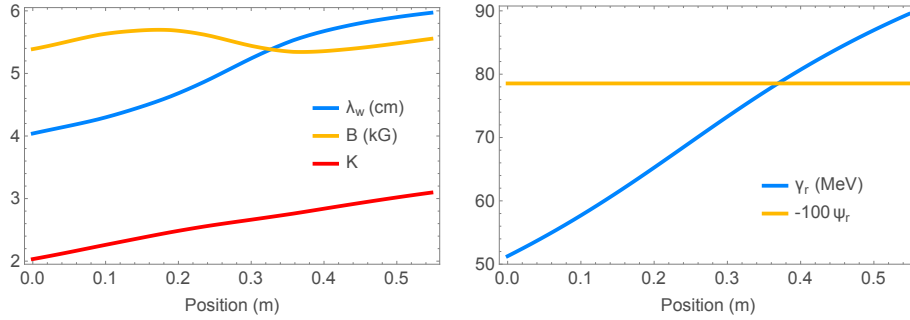


Figure 4.2: The undulator parameters for the high capture taper design are shown left while the dynamical quantities are shown right.

tostatic simulations were used determine the exact gaps required to achieve the designed  $K$ . The measured laser and e-beam parameters used in the tapering design are specified in Table 4.3. The design parameters were revised from earlier estimates to reflect measurements from the previous experimental run. For example the Rayleigh range was previously estimated to be 25 cm as measured by a scan of the evolution of the laser’s transverse profile along the undulator. Futhermore, we measured an  $M^2$  value of 1.07 which was also used in the design.

The taper design process involved repeatedly calculating a taper and then assessing its performance using simulations with the expected parameters. The design resonant phase and laser peak focal intensity dictating the accelerator’s performance were set to be  $-\pi/4$  at  $4 \text{ TW/cm}^2$  in order achieve full acceleration by operating well within the capabilities of the laser and softening alignment tolerances.

### 4.2.3 Mechanical design

The helical undulator used in the experiment is the first ever strongly period- and field-strength tapered permanent magnet undulator with a helical geometry. The mechanical design is based on the UCLA helical undulator design which was successfully developed for twisting an electron beam so that it could be used

for the generation of orbital angular momentum light [53, 54]. The undulator is composed of the superposition of two orthogonally oriented permanent magnet Halbach undulators each with four magnets per period and shifted by a quarter of a period relative to each other [51]. Strong tapering varies the resonant energy allowing for high gradient acceleration. The helical trajectory of the electrons traveling through the undulator coupled with a circularly polarized laser offers continuous acceleration as the electrons undulate in a helical motion about the undulator's axis resulting in more than twice the gradient of a planar undulator.

Whereas the transverse profile of all of the magnets are identical for ease of manufacturing, the undulator magnets' thicknesses are determined by the undulator period, which in turn is determined by the IFEL tapering equations derived in Chapter 2. Each magnet in a given period has identical dimensions and magnetization, and rotating polarizations as prescribed by the Halbach design. The choice of constant transverse dimensions (magnet shape and gap) along the undulator ensures that the period alone determines the on-axis field. An undulator builder equation gives an approximate relation between undulator period and normalized vector potential, and the builder equation for the helical Halbach permanent magnet undulator was reported by Equation 2.44.

The Rubicon undulator utilizes a thin pipe inserted into the gap between magnets to maintain high vacuum. Aluminum was chosen for the pipe's material for its low magnetic susceptibility. On the other hand, flanges for beamline connections are typically made of steel since the material's hardness preserves the shape of the knife edge used for cutting into copper gaskets in order to seal the vacuum. Since aluminum does not weld easily to steel, aluminum-steel blast formed flanges were used. The pipe geometry was chosen to have an inner diameter of 13 mm for reasonable vacuum conductance and a wall thickness of 0.5 mm in order to keep the magnet gap as small as possible while maintaining reasonable structural integrity. The magnet gap was chosen to be 15 mm, leaving 500  $\mu\text{m}$  on each side

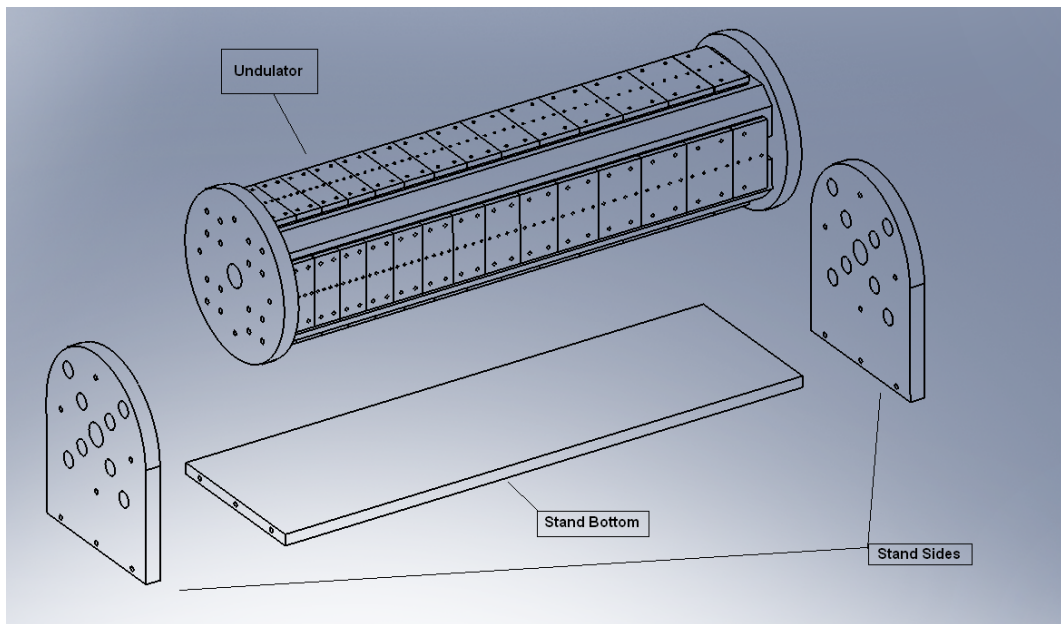


Figure 4.3: Engineering model of the partially assembled undulator body.

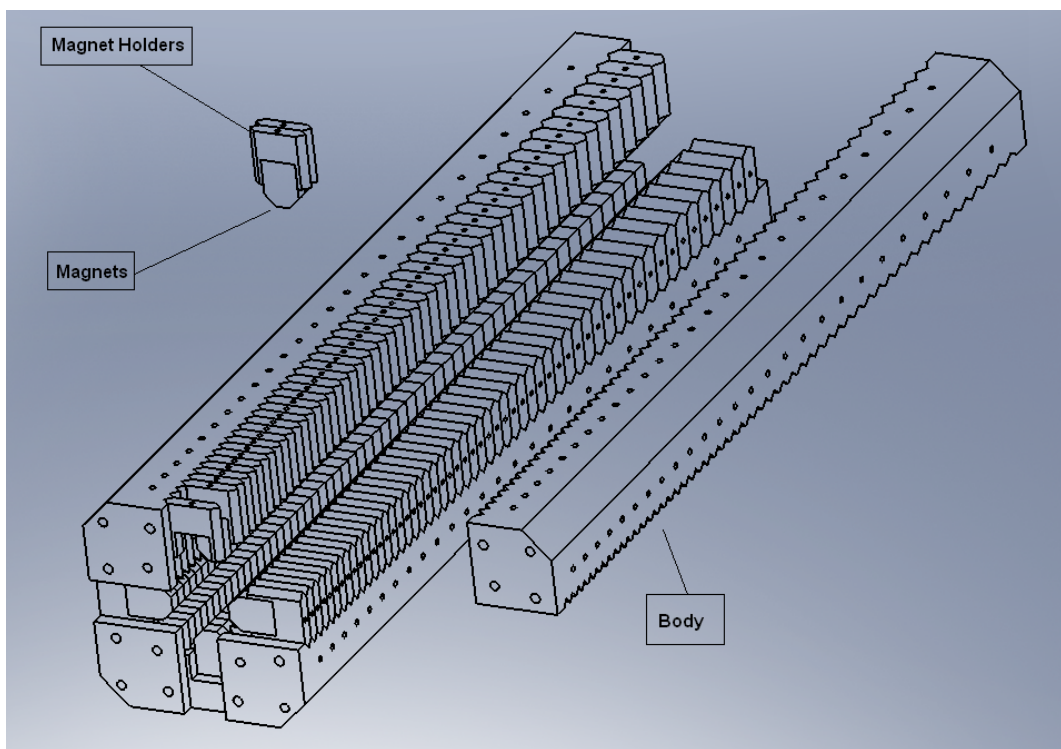


Figure 4.4: Engineering model of the undulator rails with magnets.

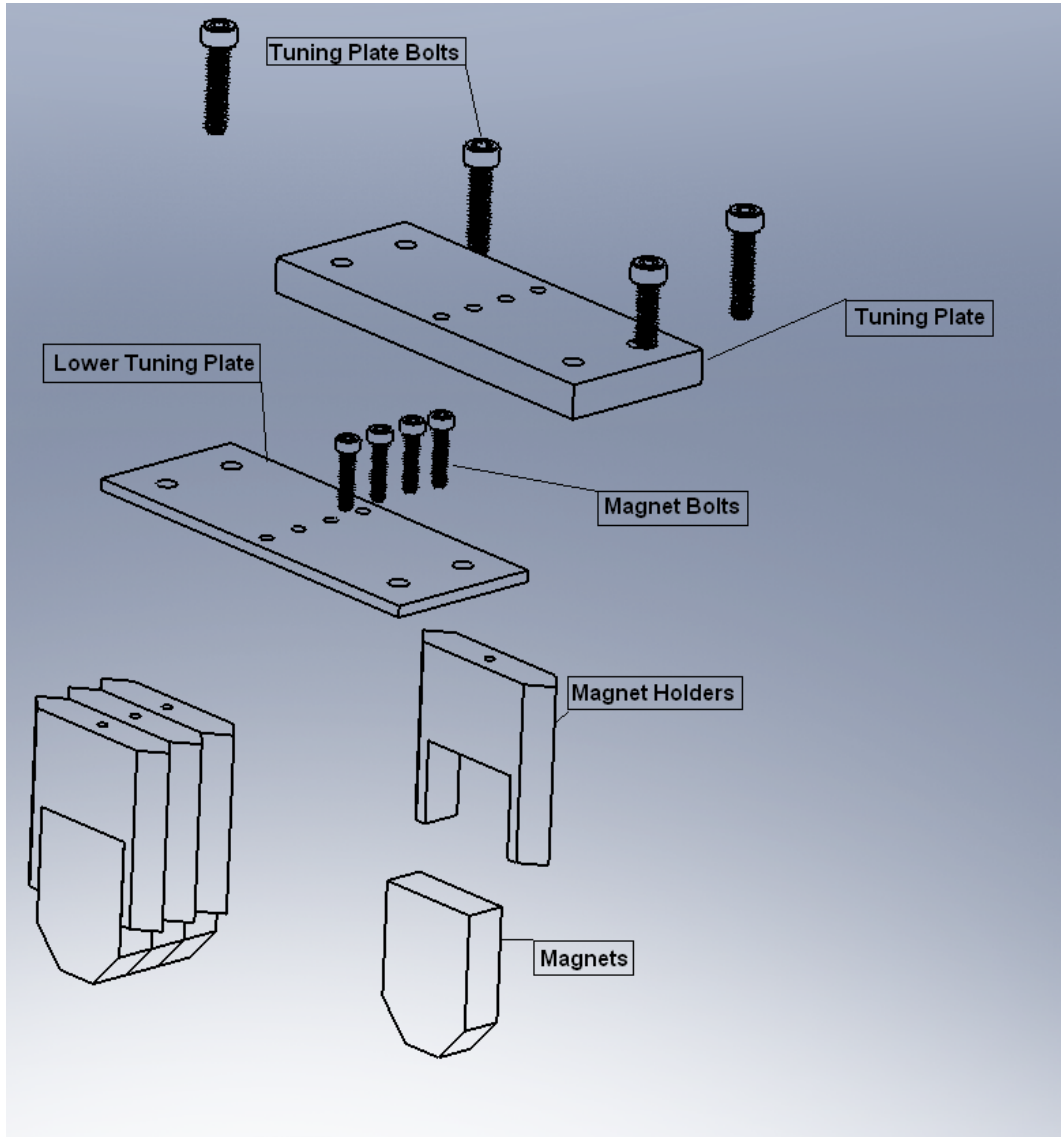


Figure 4.5: Engineering model of the undulator magnet holders and tuning plates assembly.

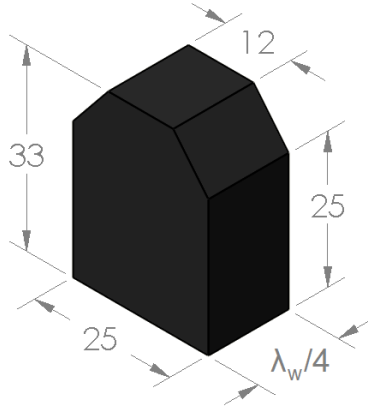


Figure 4.6: Magnet model with dimensions in mm.

for magnet tuning.

To ease manufacturing costs and design, the undulator magnets are all the same shape and vary only in their thickness. All are NdFeB magnets with a residual magnetization of 1.22 T and EDM (electrical discharge machining) wire-cut with 50  $\mu\text{m}$  precision to 33 mm on the major axis and 25 mm on the minor axis with the last 8 mm of the side nearest the beam linearly tapered from 25 to 12 mm as shown in Figure 4.6. Additionally, entrance and exit periods were designed to keep the axis of the helical motion of the electron beam centroid centered on the laser [34]. The scheme uses blocks with thicknesses  $\lambda_u/8$  and  $\lambda_u/16$ , each spaced by  $\lambda_u/4$  at the entrance and exit of the undulator. As a result, the thinnest magnets used were 2.5 mm thick.

#### 4.2.4 Construction

The magnets were ordered from a company specializing in producing permanent magnets with high residual field strength and coercivity. Each magnet was wire cut from a large cylinder of NdFeB with 1.22 T magnetization and  $\geq 1990$  kA/m intrinsic coercivity into a uniform shape with thicknesses of a quarter undulator period to within a precision of 50  $\mu\text{m}$ . The pole faces on one side of each magnet

were tapered to increase the magnetic flux density near the beam by allowing the gap between nearby magnets to reduce without collisions. The magnetization of each magnet was chosen to either point normal to the smallest (tapered end) or largest faces. Magnets with magnetization normal to the smallest face and pointing outward away from the magnet are referred to as up magnets while those pointing inward are down magnets. Those polarized so that the magnetization is normal to the largest face are referred to as in/out magnets. Each period is made from 4 up magnets, 4 down magnets, and 8 in/out magnets whereas the entrance and exit sections were each composed of 2 up and 2 down  $\lambda_u/8$  magnets, 4 in/out  $\lambda_u/16$ , and 1 up and 1 down  $\lambda_u/4$  magnets. The number of magnets ordered was twice the number needed to allow for spares in the event that some were damaged during construction.

The 100% excess of magnets allowed us to perform additional selection cuts to choose magnets with the least variance. First, each magnet was inspected for visual defects. Occasionally, magnets had chips on their sharpest edges due to the brittleness of NdFeB. The largest chips affecting  $>2$  mm and were discarded. Magnets with the deviation of the magnetic moment's axis from the mechanical axis greater than 2 degrees were also eliminated from the selection. The mean deviation was 1.36 degrees and standard deviation was 0.47 degrees. The requested remnant field strength tolerance was better than 2% deviation from 1.22 T. Specially designed brackets were used to position an axial hall sensor at a region of minimal field gradient transverse to the polarization, and the field of each magnet at that position was measured. The mean of the field measurements at these positions for each set of identically designed magnets was then calculated, and magnets with measurements closest to the mean for their group were selected. For these measurements, all of the magnets were less than 2 standard deviations from the means of their groups. The standard deviations for each group varied from 0.3 to 1.1% of the mean but was typically 0.5%.

The surfaces where the magnets and holders interface were first cleaned with acetone to remove oil. Alternatively, isopropyl alcohol is a better choice since the acetone removed some of the protective coating leading to a bit of localized rusting on the surface of some of the magnets. The holder surfaces were then roughened with coarse grit sandpaper and scored with a razor to increase the surface area available for the epoxy to bond with. The magnets were epoxied in their holders and placed in an oven for 2 hours between 50 and 60 °C and then allowed to cool for at least 48 hours. The annealing procedure was recommended by the epoxy manufacturer to increase the shear strength of the bond with etched aluminum by 50% [55]. Furthermore, there is evidence that thermal treatment improves the radiation resistance of NdFeB magnets [56]. The oven temperature throughout the annealing process was kept well below the Curie point of NdFeB (about 300 °C), and the magnetization of a test magnet was found to remain unchanged even after an integrated total of more than a week of continuous baking. The magnets polarized transverse to the beam have a large force pulling them in towards the pipe. Caps were bolted into the holders of these magnets, pinning the magnets in place to prevent catastrophic damage to the pipe or other magnets in the unlikely event of an epoxy bond failure.

The undulator was entirely designed and built at UCLA. Drawings for the parts were made using SolidWorks, computer aided design software. The undulator body and magnet holders were all manufactured to within a 50  $\mu\text{m}$  tolerance by the UCLA machine shop. The main body of the undulator is composed of 4 rails held in place by circular 3/4 inch plates at each end. Each rail has teeth creating slots for each magnet and was pinned to the end plates to ensure that they were parallel so that the magnet holders could be inserted in the slots between the rails. Each period has 4 modules of 4 magnets attached to a plate by a standard #4-40 bolt. These modules were installed into the slots between the rails, covered by an additional plate sandwiching the bolt heads, and bolted to the rails. This

assembly was attached to a frame made of two end plates connected to each other by a base plate. In order to maintain good vacuum while transmitting the laser, the electron beam is transported through a thin aluminum pipe which fits within the 15 mm gap between undulator magnet poles. With the rails removed, the four end plates were sandwiched together so that the pipe could be inserted and welded to the flange.

#### 4.2.5 Magnetic field modeling

The tapering solution describes the desired on-axis undulator field for efficient acceleration given the design parameters. Realizing that field can only be achieved after careful modeling of the fields generated by the physical undulator’s permanent magnet array. The undulator builder equation is a good first step, yet it can not capture the full complexity of the problem and ignores the tapered ends of the designed magnet blocks. As a next step to modeling the field, we used Radia, a 3D magnetostatic field solving code developed by the European Synchrotron Radiation Facility to design insertion devices for synchrotron light sources [57].

<b>Index</b>	<b>Period (mm)</b>	<b>Index</b>	<b>Period (mm)</b>
1	40.0	7	51.9
2	41.1	8	54.9
3	42.3	9	56.9
4	43.9	10	58.3
5	45.9	11	59.3
6	48.6		

Table 4.4: Undulator period lengths

As described earlier, we discretized the undulator period profile by sampling the design undulator wavelength every period. The resulting list of periods (see Table 4.2.5) became the layout plan for a three dimensional model of the magnet

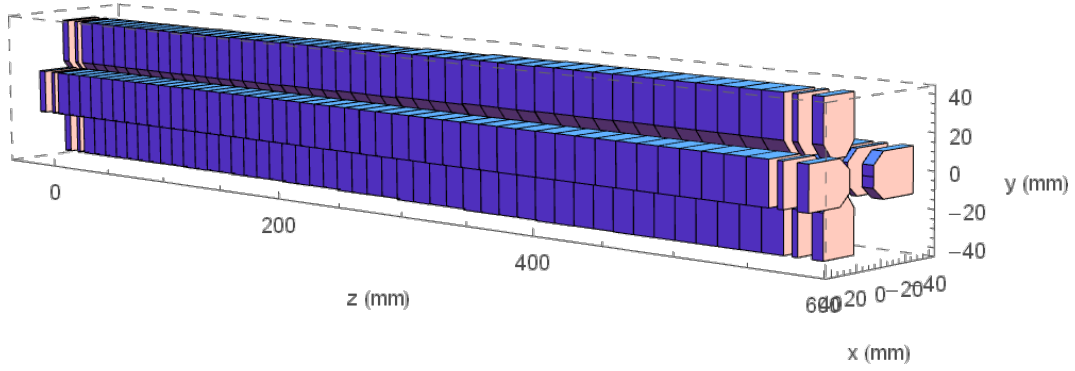


Figure 4.7: Undulator geometry for the Radia model.

array. From the on axis field profile which is then obtained, one can calculate the undulator parameter  $K$  and resonant energy along the undulator from the norm of the on-axis magnetic field.

Once the on-axis field is sufficiently close to design, the fields must be adjusted slightly in order to keep the trajectory of the electron beam on-axis. The velocity may be calculated from the first integral of the on-axis fields as  $\gamma m dx_i/dt = (-1)^i q \int dz' B_{3-i}(z')$  whereas the trajectory may be approximated assuming ultra relativistic electrons ( $dz/dt \approx c$ ) by the second integral as  $x_i = (-1)^i \frac{q}{mc} \int dz' \frac{1}{\gamma} \int dz'' B_{3-i}(z'')$ , where  $i = 1, 2$  correspond to the  $x$  and  $y$  coordinates. The increase in field amplitude causes the integral over each period to be nonzero, causing a deflection which grows for each period. If the field amplitude gradient is strong enough, the resulting deflection may become roughly the size of the laser waist causing the interaction to suffer from lower laser intensity off-axis.

In order to eliminate the trajectory walk-off, we modified the magnet gaps by slightly decreasing the gaps of the first two magnets in each period and increasing the gaps of the last two. This made the field within each period more uniform by increasing the magnetic field at the beginning of each period and decreasing it at the end of each to oppose the otherwise positive gradient in the magnetic field and compensate the trajectory deflection.

#### 4.2.6 Geometrical measurements and initial tune

The mechanical design of the undulator offered the possibility of tuning individually each of the permanent magnet blocks. As a first step to tuning the undulator, we initially positioned each magnet so that the gap between magnets matched the design. For the high gradient configuration, the gap was made to be a constant 15 mm by backing the magnets out completely, measuring their initial heights from the tuning plate, and then calculating the number of turns of the tuning bolts for each magnet to achieve that gap. The heights of each magnet sitting in their holders vary by hundreds of microns due to varying thicknesses of the epoxy resin used to bond the magnets to their holders. Some pitfalls of this approach were later realized. First, the tuning bolts have about 1/8 of a turn play before moving the magnets. Since we used #4-40 bolts, this introduced a systematic error of about 80  $\mu\text{m}$  with some additional variance due to the possibility of changing directions. Another source of error came from assuming that the rails which the magnets sit in were perfectly straight. As a result, the gap of the initial tune varied by hundreds of microns for each magnet, causing the field to deviate from design and necessitating significant trajectory corrections.

The results of the first experiment left room for improvement and motivated a subsequent experiment using the same undulator but with a different tune as mentioned earlier and will be discussed in detail in the following chapter. Having a chance to retune the undulator enabled us to improve upon the initial geometrical magnet tune by learning from previous mistakes. For this second high capture undulator tune, we increased the precision of the geometric tune by increasing the number of measurements of the physical geometry.

The undulator magnets are held in place by bolts which provide fine tuning of the gap over a range of a couple mm; however since the half gap needed to be increased by about 2.2 mm towards the undulator's exit, three 0.8 mm thick

aluminum shims were introduced to increase it by 2.4 mm. Measurements of the local shim thicknesses, height of each magnet from pole face to tuning plate (which varied due to random epoxy interface thicknesses), average rail widths for each period (which bowed under the pressure of the inserted magnets), facilitated a calculation of the overall initial half-gap, or distance of each magnet's pole face from the geometric axis when retracted fully. The results of these measurements and each magnet's calculated initial half-gap are shown in Figure 4.8 along with the design half-gap.

As mentioned in the [previous section](#), changing the gaps of the first and last two magnets of each period slightly from design helps to keep the e-beam trajectory oscillating about the geometric axis. Since thread tolerances cause up to 80  $\mu\text{m}$  play as each bolt was turned, we placed a hall sensor on axis near each magnet before moving to detect movement as its corresponding bolt was turned before recording the degrees turned. Furthermore, care was taken to only drive the magnets in one direction to reduce this lag error during tuning.

#### 4.2.7 1D field measurement setup

After the initial magnet placement, we measured the on-axis fields to assist tuning the undulator and to estimate the accelerator's performance. A motorized hall probe system shown in Figure 4.9 was developed to automate scans of the on-axis transverse magnetic field profile. The hall probe was attached to a threaded brass rod via a Teflon carriage and driven by a stepper motor through a brass pipe which was held in place by irises attached to either end of the undulator. This allowed for reproducible measurement step sizes of as large as 1.5 mm, or about 30 measurements per period, which was chosen as an upper limit to measure the peak field to better than 0.1%. The stepper motor was calibrated by measuring the number of steps required to move the brass rod 70 cm.

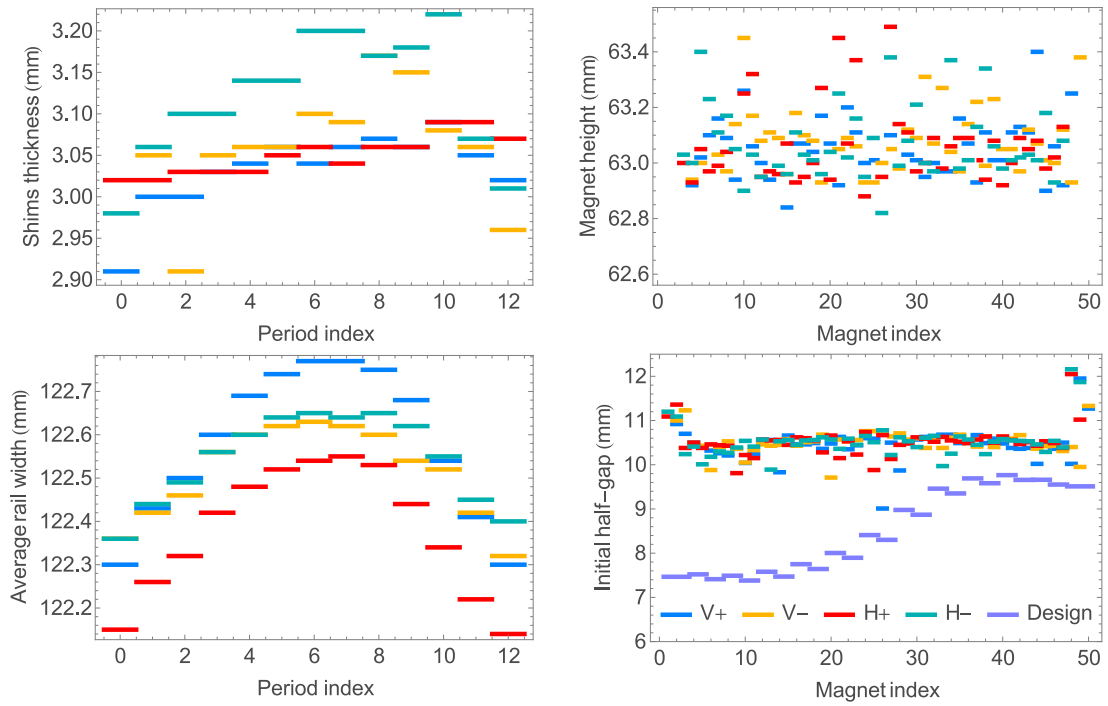


Figure 4.8: Various geometric measurements of the undulator and magnets are shown above. Vertical and horizontal magnets are color coded as shown in the bottom right figure.

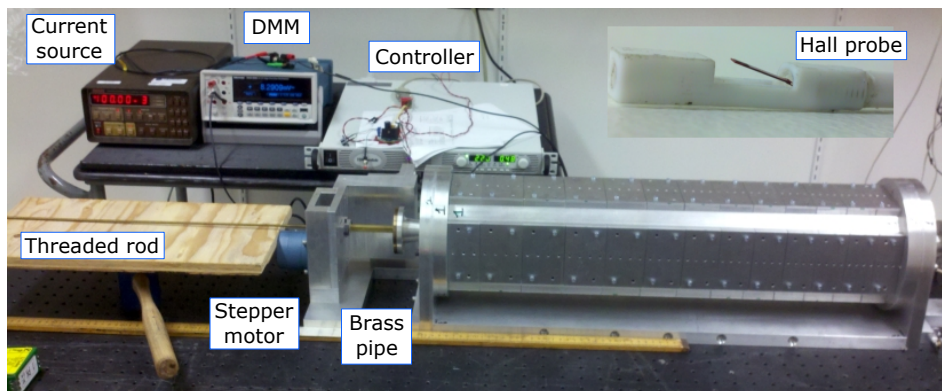


Figure 4.9: Undulator field scan setup.

A fixed current source supplied the hall effect sensor with stable current of  $50 \mu\text{A}$  while a digital multimeter measured voltage to a precision of about 0.004%. The hall sensor magnetic field response was determined to be 109.6 G/mV when calibrated with a reference magnet. Deviation from linearity in the range of 0.8 kG to 9.6 kG for positive and negative polarity was measured with two strong magnets arranged in a Helmholtz geometry and corrected for in the resulting scans. Measurements were automated with LabVIEW, a system design software, which was instructed to pause between motor drives to allow vibrations to damp. The software was configured to measure the field several times and then calculate the mean and standard deviation to evaluate the uncertainties in the measurement.

#### 4.2.8 Undulator tuning

The field scans guided the tuning. Each magnet holder was connected to plates by a single #4-40 bolt as shown in Figure 4.10. Adjusting the bolt allows the magnet to travel in a slot between the undulator rails, thereby modifying the magnet gap. Each magnet was first tuned into place geometrically as [described earlier](#). The gaps between magnets were then tuned simultaneously to achieve a less than 0.1% rms deviation with the Radia simulated field profile. The measured fields for the transverse directions are shown in Figure 4.11.

Integrals of the measured fields were calculated in order to estimate the mean velocity and position of the electron beam as it traverses the undulator and are shown in Figure 4.11. It is desirable to keep the electrons from deviating too far from the axis and out of the center of the laser radiation. The largest predicted electron beam undulation radius was estimated to be about half the expected minimum laser waist of  $\sim 1$  mm near the undulator's exit. A further goal of minimizing the deflection was met, and the exit angle was estimated to be less than 1 mrad.

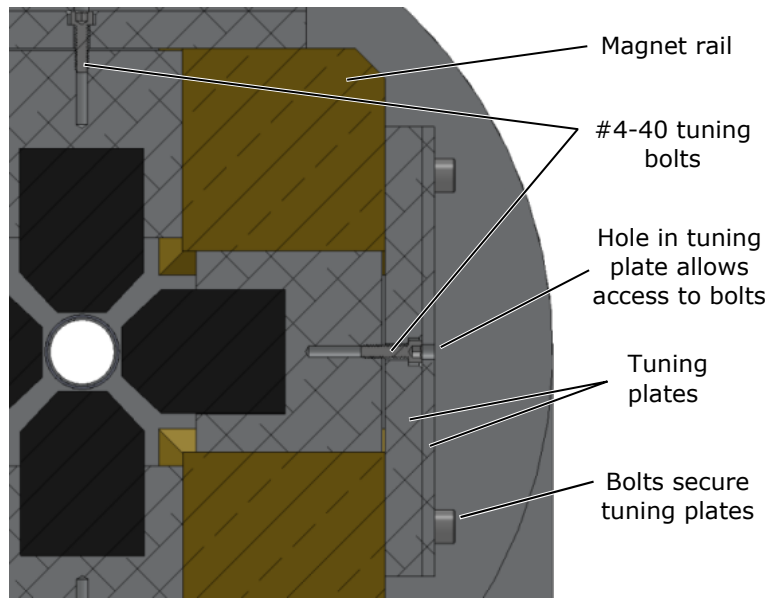


Figure 4.10: A cross sectional view of the undulator showing gap adjustment. The magnet sits in a slot in the rails and attaches to the tuning plate by a single bolt which can be adjusted to move the magnet in the slot.

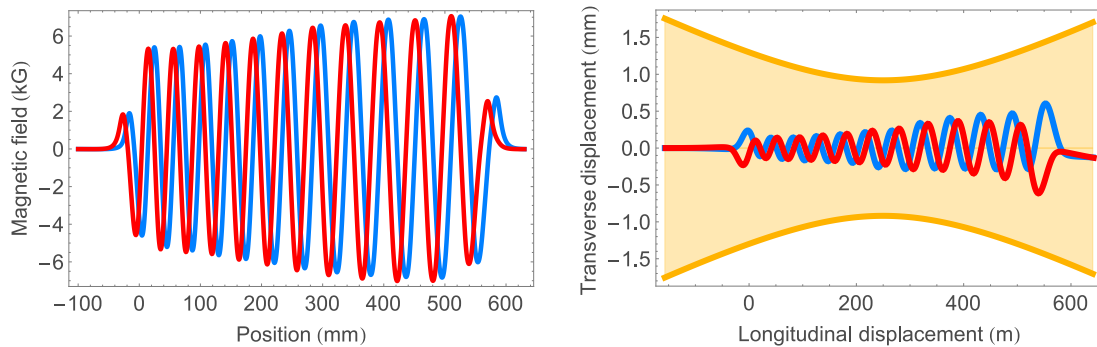


Figure 4.11: Measured transverse magnetic fields and calculated transverse trajectories (assuming a constant 50 MeV energy) for the high gradient undulator tune. The trajectories are superimposed on top of the design laser waist for scale.

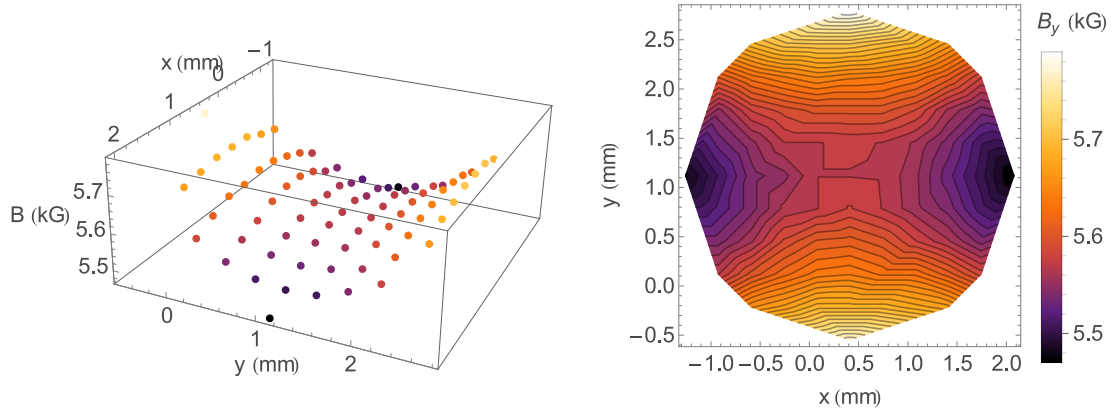


Figure 4.12: Transverse scan of the vertical component of the magnetic field measured at a peak within the undulator.

For the high-capture configuration, the fields were measured to be initially systematically low by a couple percent. Magnets were then tuned slightly in pairs, again moving the first two and last two pairs of magnets as groups, to increase the field to that of the Radia simulations. Finally, the fields were finely tuned to reduce the transverse kick and offset estimated by the first and second integrals of the field for a 50 MeV e-beam. The final measured fields were found to agree to within 0.5% rms of the Radia simulations.

#### 4.2.9 3D magnetic field scans

To further investigate the undulator magnetic field, we performed scans of the transverse fields in three dimensions with a 3-axis stepper motor assembly at ATF using a LakeShore calibrated hall probe. The setup consisted of a Newport stepper motor driven linear stage with 600 mm of travel and two transverse stages with 1 or 2 cm of travel distance. The hall probe was inserted snugly into the end of a hollow copper tube with approximate outer diameter of 4 mm. The tube was attached to the stage and aligned so that the hall probe was centered on the undulator's axis to within a couple millimeters at the entrance and midpoint of the undulator. Care was taken to keep the hall sensor surface's normal less than

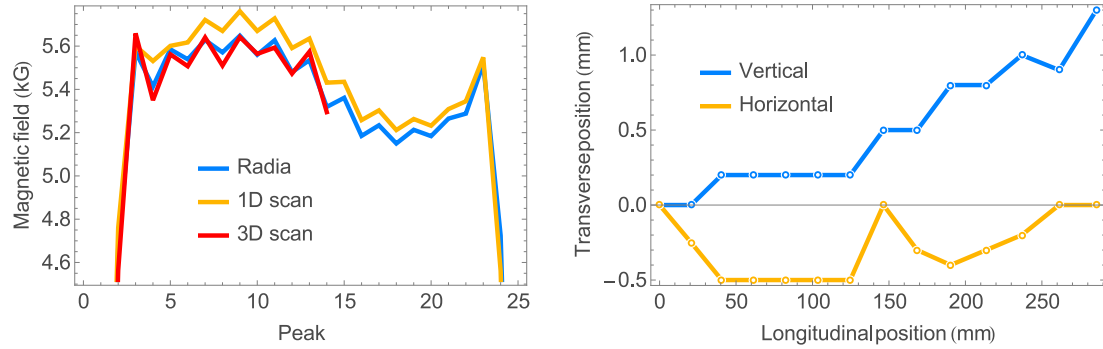


Figure 4.13: The left plot shows the design and measured peak values of the final tuned field while the right plot shows the positions of the saddle points measured with the 3D field scan.

5 degrees from the desired undulator axis so that the measured field was at least 99.6% of the actual field, and a digital multimeter measured the resistance between the copper tube and the undulator to detect collisions. The system was controlled with custom ATF software built on top of a National Instruments framework via Mathematica.

Scans were performed stepping forward longitudinally from the undulator’s entrance, raster scanning transversely, and then repeating. For each point, the field was sampled several times, and the median value was recorded. At each longitudinal position, the field was measured on a grid bound by a circle with fixed radius to avoid collisions with the beam pipe. The points were sampled in a spiral with points near the circle’s center measured first to reduce scan times. The result of each scan is a cylindrical lattice of field measurements which may be interpolated.

There are 25 field peaks on-axis—22 corresponding to the 11 periods and 3 corresponding to the entrance and exit periods. Each peak is at a maximum with respect to the longitudinal coordinate and at a saddle point with respect to the transverse coordinates. Figure 4.12 shows a transverse slice of a 3D field map of the magnetic field’s vertical component taken at the longitudinal position of one

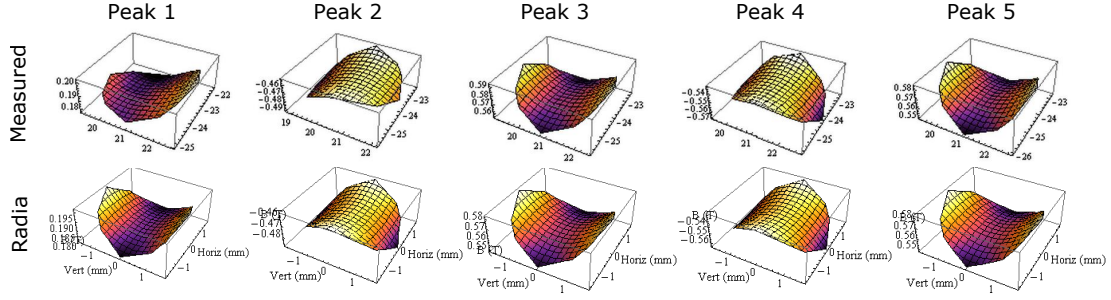


Figure 4.14: Measured and Radia field maps for the first 5 peaks.

of the 25 field peaks along the undulator. The saddle point is clearly visible near the center of the plot and the field increases for transverse offsets towards the similarly polarized magnets and decreases for excursions transverse to the pole faces of these magnets as the distance to the magnetic moment increases. For this peak, the field drops off twice as fast for horizontal offsets in  $x$  as it does for vertical offsets in  $y$ .

The saddle points of the peaks offer position markers of the magnetic axis of the undulator. Ideally, the electron beam should be centered on this axis for proper focusing and for reducing higher harmonics sampled by the electron. Figure 4.13 shows the amplitudes and positions of the peaks for the first 6.5 periods—as far as the stage could move the probe through the undulator. From the positions of the peaks, it is clear that the probe trajectory was not aligned to the undulator axis; however, the magnetic axis varied only  $100\ \mu\text{m}$  from a straight line in the vertical plane and as much as  $300\ \mu$  horizontally. The saddle point measurements of the final tuned fields agree well with Radia, fluctuating about the Radia model by typically less than a percent, whereas the 1D scan method with the hall probe was systematically higher than the Radia model. Transverse field maps for the first five peaks are shown in Figure 4.14 and the shapes of the measured field maps very closely match their modeled counterparts.

Unfortunately, the lack of a long stage precluded our ability to scan the undulator fully. On the other hand, the positions of the saddle points were relatively

straight. If the probe’s trajectory could be manipulated with mechanical stages so that it went straight through entrance and exit irises positioned coaxial with the undulator’s geometric axis, these saddle points may be seen to lie on a straight line. With that modification, this method could be part of a systematic scan procedure for future helical undulators.

### 4.3 Expected performance

In order to estimate the accelerator’s expected performance, we used the measured fields of the tuned physical undulator with the FEL simulation code Genesis 1.3 [48, 58]. The code simulates the particle motion in three dimensions and additionally solves the radiation evolution on a transverse grid. The longitudinal motion is solved with the FEL period averaged equations of motion [59]. Despite this approximation, Genesis is well suited for modeling the FEL interaction and has been used to guide the design of successful FEL experiments such as the LCLS [60, 61]. Since it does not allow for arbitrary period tapering, we chained together Genesis simulations for each undulator period using the measured period and  $K$  parameter from measurements [62]. Further, we verified that the results of our IFEL simulations agreed well with Tredi [63], a code successfully used in the design of the Neptune IFEL experiment [24].

Shortly before the experiment, certain parameters were changed out of necessity. First, the wavelength of the CO<sub>2</sub> laser pulse was changed from 10.6 to 10.3  $\mu\text{m}$  in order to mitigate temporal pulse splitting. Periodic rotational lines in the gain spectrum applied during amplification produce a train of pulses, reducing the peak power of the leading pulse. The gain spectrum was smoothed out by adding an isotope of CO<sub>2</sub> with slightly shifted energy levels and changing the seed wavelength from the  $10P$  branch of the spectrum (10.6  $\mu\text{m}$ ) to the  $10R$  branch (10.3  $\mu\text{m}$ ), which is more densely populated by rotational lines [50]. Since

the resonant energy varies inversely proportional to the square root of the laser wavelength, the resonant energy along the undulator was uniformly increased by 1.4% as a result of this shift.

A second, more consequential change was due to the late realization that a beam pipe aperture limited the spot size of the CO<sub>2</sub> laser to about 27 mm at a position 2 m upstream of the undulator. In order to transmit the entire laser pulse energy without clipping on the restricting aperture, the Rayleigh range of the laser was relaxed from 9.6 cm to about 25 cm. An unfortunate consequence of this change was that the ponderomotive gradient was no long matched to the resonant energy gradient set by the undulator tapering, leading to a decrease in the expected fraction of particles accelerated to full power. On the other hand, relaxing the focusing by a factor of three causes the waist to enlarge by a factor of  $\sqrt{3}$  making the alignment tolerances more forgiving.

<b>Parameter</b>	
Initial energy	50 MeV
Initial energy spread	0.15%
Current	100 A
Normalized emittance	2 $\mu\text{m}$
E-beam size at entrance	200 $\mu\text{m}$
Laser peak power	500 GW
Laser wavelength	10.3 $\mu\text{m}$
Rayleigh range	25 cm
Laser waist	910 $\mu\text{m}$

Table 4.5: High gradient run simulation parameters

The parameters used in the simulations are summarized in Table 4.5. The simulated input beam was uniformly distributed in phase and normally distributed in energy with a mean energy of 50 MeV and an rms width of 0.15%. The normalized

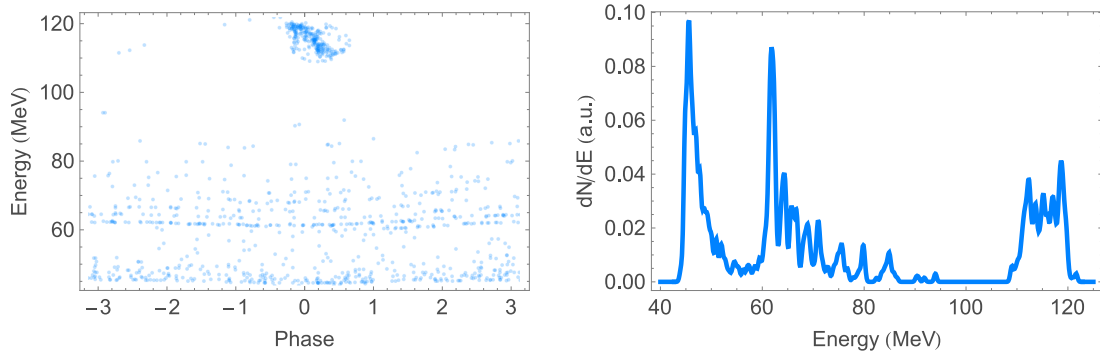


Figure 4.15: IFEL output phase space and electron spectrum for 500 GW peak laser power.

transverse emittance of the ATF e-beam was taken to be on the conservative side of the nominal range of 1 to 2 mm-mrad. The focused electron beam spot size at the entrance of the undulator was set to 200  $\mu\text{m}$  which beamline simulations performed using the Elegant accelerator code showed was just within the reach of the quadrupole doublet. While the matched beta function at the undulator's entrance is half of the 1 m value used here, simulations showed that using a longer beta function would not affect the accelerator performance significantly. Genesis used the 100 A beam current and macroparticle distribution and calculate longitudinal space charge fields using a Fourier series approximation as well as to calculate the reduction in laser field strength along the undulator due to the small level of optical-to-electrical power transfer.

The resulting longitudinal phase space of the simulated output beam is shown in Figure 4.15. The accelerated bunch is clearly separated from the background and has a mean energy of 117 MeV with a relative energy spread of 2.5%. One quarter of the particles remain trapped throughout the interaction, and the lengths of the resulting microbunches were less than 1 fs rms. Simulations for various peak laser powers were also performed in anticipation of laser power fluctuations. The result of these simulations showed that the fraction of fully accelerated particles increased with laser power from the capture threshold close to 300 GW to 26% at

500 GW. For powers greater than 500 GW, fraction trapped saturates at about 1/3 of the beam accelerated. The energy spread increases with laser power as expected since increasing laser power increases the ponderomotive bucket height, enabling it to accommodate more particles throughout the interaction. It is important to note that these simulations assume that the input e-beam bunch duration is small compared to that of the laser so that the laser field strength felt by the bunch is uniform.

<b>Power</b>	<b>400 GW</b>	<b>500 GW</b>	<b>600 GW</b>
Fraction accelerated	13%	26%	31%
Mean final energy	117 MeV	117 MeV	115 MeV
Energy spread (rms)	2.0%	2.5%	3.8%

Table 4.6: High gradient run simulation results

Time dependence was included by dividing the beam longitudinally by slices each one laser wavelength long and separated by an constant integer number of wavelengths. We used this method to simulate the temporal effects of the IFEL process for the parameters in Table 4.5. Both beam current and laser power temporal profiles were modeled as Gaussian with pulse lengths of 5 ps and 4 ps respectively and coincident at the undulator’s entrance. The accelerated fraction was 10% with a mean energy of 117 MeV and a fwhm energy spread of 1.7%. When taking into account the finite pulse widths of the laser and e-beam, the accelerated pulse had a reduced rms pulse length of 1.7 ps owing to the fact that only the center part of the laser had a strong enough electric field to maintain resonance. This result shows that it is important to keep the e-beam duration as short as possible in order to maximize the observed fraction of fully accelerated electrons. The shortest beam with reasonably stable relative charge fluctuations produced at the ATF is about 1 ps fwhm with 100 pC charge. On the other hand, the linac jitter at the ATF is estimated to be roughly 1 ps rms.

### 4.3.1 High gradient taper design tolerances

The final energy of the accelerated electrons is insensitive to most input parameters since the resonant energy is determined by the undulator tapering. Small deviations from the optimal parameters may cause fewer particles to remain trapped and accelerate so the best figure of merit describing the accelerator performance is the fraction of particles accelerated. A study of the tolerances in the input parameters was performed by systematically varying the parameters in the simulation from their optimal values. The simulations here are time independent so the predicted values only hold for short electron bunches, yet the resulting parameter ranges are useful regardless of bunch duration. The results of these parameter scans are listed in Table 4.7.

<b>Parameter</b>	<b>20% capture</b>	<b>10% capture</b>
Input energy	49.8 – 53.7 MeV	49.1 – 54.9 MeV
Laser power	> 440 GW	> 370 GW
Transverse beam offset	< 260 $\mu\text{m}$	< 480 $\mu\text{m}$
Rayleigh range	< 30 cm	< 37 cm
Focal position (rel. to center)	-11.8 – 1.2 cm	-16.8 – 7.7 cm

Table 4.7: High gradient run parameter tolerances

Restrictions on the input energy are limited by the ponderomotive bucket which is centered on the resonant energy. Particles injected significantly lower than 1 MeV below the design input energy of 50 MeV never accelerate to full energy. On the other hand, particles injected above the resonant energy find themselves in resonance further along the undulator, and 10% of the particles are still accelerated when injected 5 MeV above resonance.

Transverse beam offsets were introduced into the simulations in order to estimate acceptable alignment tolerances. Failure to fully cancel dispersion along bends in the ATF beam line may introduce positioning jitter as the output energy

of the linac varies due to phase jitter in the rf power supply. We usually observed transverse pointing jitter of  $<50 \mu\text{m}$  and occasionally as high as  $150 \mu\text{m}$  near the undulator's entrance. Furthermore, the undulator, laser, and e-beam are difficult to coalign to better than a couple hundred microns. The simulations show that these offsets should not be expected to significantly affect the fraction captured and that it would take offsets of at least  $0.5 \text{ mm}$  to completely extinguish the interaction. Of course these results hold for  $500 \text{ GW}$ , while lower laser powers will shrink the tolerable range of transverse offsets. The combination of alignment errors and pointing jitter make the larger laser spot size of  $\sim 1 \text{ mm}$  especially attractive. In a demonstration experiment where time and resources are rather limited, it is very desirable to keep the laser waist close to a millimeter in order to ensure the expedient success of the experiment. On the other hand if designing a dedicated IFEL accelerator facility, one could envision that it may be more practical to take the time to finely control these variances for larger gradients from the more tightly focused laser and more stable operation.

Since the experimental laser Rayleigh range is not equal to the design value, the ponderomotive gradient evolution will not match the resonant energy gradient set by the undulator. As a consequence of the gradient mismatch, the effective resonant phase of the accelerating beam changes according to  $\psi_{r,\text{eff}} = \sin^{-1}(K_l^{-1} K_{l,\text{design}} \sin \psi_{r,\text{design}})$ . One consequence of the resulting rapid change in resonant phase is that the particles no longer symmetrically rotate about a fixed point, but begin to slosh around in the extremes of the bucket at the synchrotron frequency. Near the laser waist where  $K_l$  is significantly less than  $K_{l,\text{design}}$ , the bucket shrinks and particles in this region begin to detrap. In order to reduce the number of particles lost in this region, it is helpful to place the waist near a phase of the synchrotron oscillation where the energy spread is maximal in order to make the height of the bucket more accommodating.

Since the synchrotron period over the first half of the undulator is about  $25 \text{ cm}$ ,

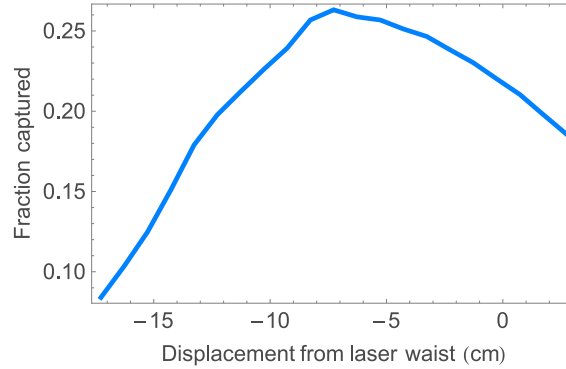


Figure 4.16: Fraction of accelerated particles vs position of waist relative to the undulator’s midpoint. The optimal laser waist position is about 7.5 cm upstream of the undulator’s midpoint.

the electrons have maximal energy spread about 19 cm into the undulator (3/4 of a complete synchrotron rotation) or 8 cm upstream of the undulator’s midpoint. Figure 4.16 shows the fraction captured as the position of the waist is scanned relative to the undulator’s midpoint. The fraction captured is maximized when the waist is placed 8 cm upstream as expected. In the next section of this chapter, a revised version of this experiment with matched gradients is devised, largely eliminating the benefit in this shift of laser waist positioning.

Accelerated electrons steal energy from the laser and reduce the electric field available for acceleration, and too much laser depletion may lead to detrapping late in the interaction. The electron beam produced at the ATF has a current of 100 A largely independent of beam charge. By energy conservation, the power lost by the laser is equal to the power gained by the electrons, and assuming that half of the 100 A beam is accelerated to 50 MeV, merely 5 GW of power or  $\sim 1\%$  of the laser power is absorbed.

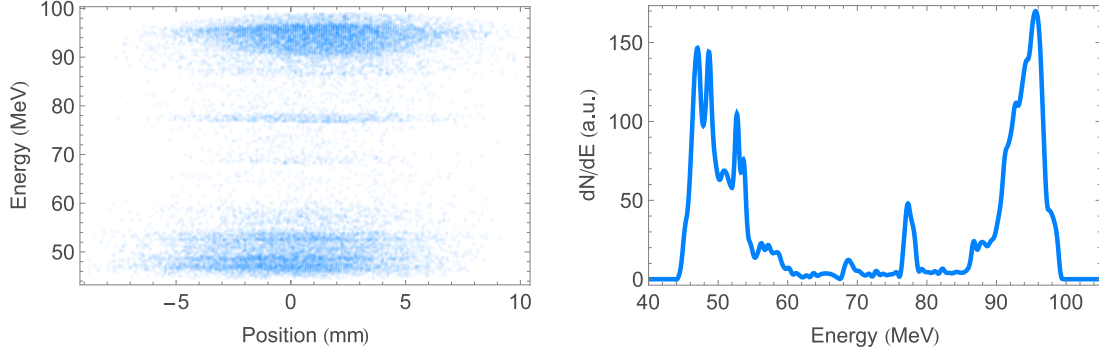


Figure 4.17: High capture simulation with  $18 \text{ TW/cm}^2$  focal intensity laser.

### 4.3.2 Performance estimates for high capture taper

Simulations were performed with the 3D IFEL code TREDI and are shown in Figure 4.18 for a 50 MeV input e-beam, laser focusing parameters listed in Table 4.3, and  $18 \text{ TW/cm}^2$  laser focal intensity corresponding to 250 GW power and 1 mm minimum waist. TREDI solves the Lorentz force equations rather than averaging the motion of the electrons over an undulator period [63] and was previously bench-marked against IFEL experimental results in planar undulators [24]. The simulation includes time dependent effects, and the 1 ps long e-beam and 4.5 ps laser pulse are synchronized at the entrance to the undulator. The simulations show that for the expected experimental parameters, as much as 43% of the beam is captured and accelerated to energies greater than 90 MeV. The accelerated beam has a mean energy of 94 MeV, rms energy spread of 2.3%, and is microbunched at  $10.3 \mu\text{m}$ .

One of the benefits of the relaxed tapering is the relatively modest requirements on the laser performance. Figure 4.18 shows how the maximum particle energy varies as the input laser focal intensity is increased with the same focusing. For sufficient intensity to fully accelerate electrons, the maximum energy can be seen to increase with the square root of the intensity as the bucket height scales with the laser field amplitude. While the laser focal intensity was previously seen to usually

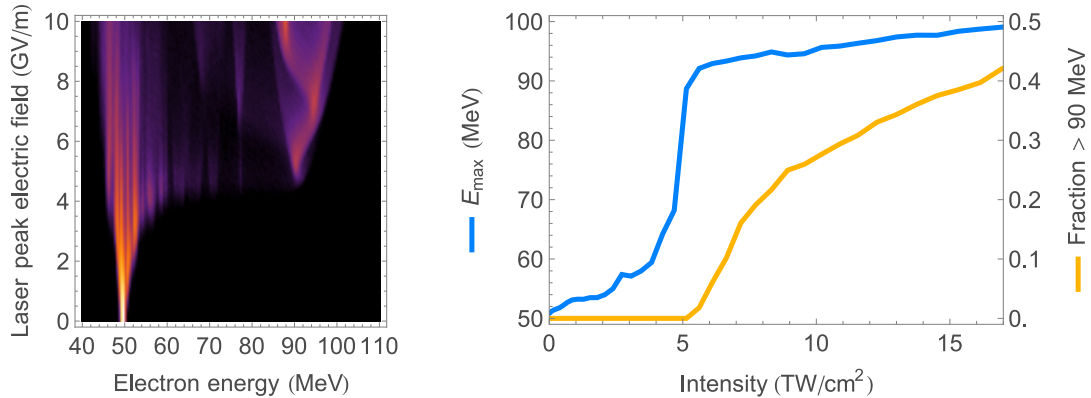


Figure 4.18: Maximum particle energy (solid) and fraction of beam with energy greater than 90 MeV (dashed) as a function of input laser focal intensity.

exceed  $15 \text{ TW/m}^2$ , the threshold for acceleration to 90 MeV for the measured undulator is merely  $5 \text{ TW/cm}^2$ . This suggests that full energy acceleration should be obtained for most shots. Furthermore, a quarter of the electrons are accelerated to energies greater than 90 MeV when the intensity is doubled to  $10 \text{ TW/cm}^2$ . These modest requirements on laser intensity for full acceleration opens the door to studies of the accelerated beam's properties.

This design approach led to the development of the first strongly period-, field-, and gap-tapered helical undulator and resulted in the first demonstration of output energy tuning in an IFEL accelerator as described in the next chapter. The design achieves efficient acceleration without prebunching by matching the ponderomotive and resonant energy gradients along the length of the interaction for the measured laser parameters.

#### 4.4 Prebuncher design for better trapping

The next step toward improving the efficiency of the Rubicon IFEL accelerator is to prebunch the input electron beam in order to increase the trapping efficiency. The fraction of injected charge which is accelerated to high energy is limited for

an electron beam with a uniform temporal distribution. Since different parts of the beam initially experience different phases of the ponderomotive wave, parts of the beam are accelerated while other parts are decelerated. If the resonant energy changes violently—that is, fast compared to the synchrotron period—particles with low energies may be lost. In order to increase the efficiency of the acceleration, it is necessary to prebunch and match the e-beam into the accelerating bucket. All optical accelerators benefit from this approach and prebunchers have been used in previous IFEL experiments to enhance their performances [23, 64, 65].

Generally, prebunching is accomplished by first imprinting a periodic energy modulation onto the electron beam and then applying  $R_{56}$  to convert the energy modulation to a density modulation. The simplest approach is to simultaneously apply energy modulation and  $R_{56}$  by using a low intensity seed with an undulator long enough for a quarter synchrotron oscillation so that the electrons are nearly maximally bunched. The low intensity seed ensures that the energy spread of the resulting bunch is small compared to the accelerator’s acceptance so that the particles may be concentrated near the center of the bucket. A drawback to this approach is that the longitudinal emittance is greatly diluted as the rotated phase space occupies more phase space. Shortening the energy modulator section and using a chicane enables compression with reduced energy spread while simultaneously providing control of the particle’s phases. The reduced energy spread and phase control enables injection into a ponderomotive bucket at a larger accelerating phase. Other more elaborate and effective bunching strategies are mentioned in Section 2.3.3.

We used the scheme of an energy modulator followed by a magnetic chicane for the Rubicon IFEL prebuncher, shown in Figure 4.4. The energy modulator consists of a single 50 mm period planar Halbach permanent magnet undulator [51] with NdFeB magnet blocks of 1.22 T magnetization and gap between opposing magnets chosen to be 17.5 mm in order to set the on-axis field strength such that

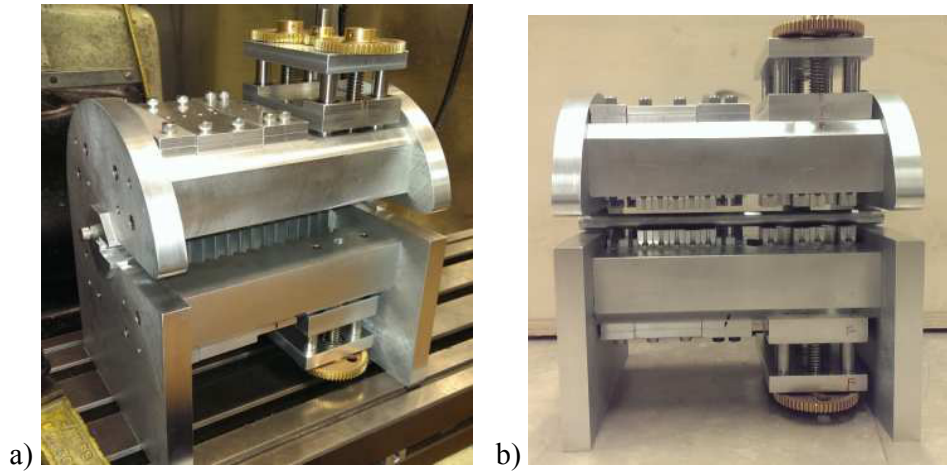


Figure 4.19: The figure above shows two views of the prebuncher module. a) A view of the partially assembled prebuncher shows the tuning plates and end iris for the aligning the hall-probe to the undulators axis for field scans. b) The prebuncher is shown with magnets inserted. On the left hand side of each picture is the energy modulating undulator while the right side of each shows the phase modulating chicane with motor assembly for adjusting the gap during the experiment.

the resonant energy coincides with that of the electron beam. The amplitude of the energy modulation is smaller than the height of the bucket for the IFEL accelerator so that particles fit within the resonant energy bandwidth of the accelerator. Additionally, the total length of the buncher was kept short in order to keep the separation distance between the undulator and dipole just upstream to a minimum. A planar undulator offers the desired weaker electro-optical coupling than a helical one and has the additional benefit of ease of installation and removal since a planar undulator can be simply slid over a pipe on the beamline without breaking vacuum. Entrance and exit magnet sections zeroing the second integral of the on-axis magnetic fields keep the particles oscillatory trajectories centered on the beamline axis.

The chicane is placed just downstream of the energy modulator in order to provide  $R_{56}$  for density modulation as well as to delay the particles relative to the laser wave fronts. In order to simplify construction, the same magnet dimensions used in the energy modulator are also used for the chicane; however, the gap between opposing chicane magnet pole faces can be varied by a system of gears, as shown in Figure 4.4, attached to a stepper motor in order to control the chicane field during the experiment. By finely varying the chicane field during the experiment, we can finely delay the electrons relative to the laser phase fronts in order to inject the bunched beam into the accelerating buckets by maximizing the fraction accelerated. Without a chicane, the energy modulator would have to be placed at specific positions upstream of the undulator to achieve the correct slippage for phase locking and would have to be placed far enough away to allow the small energy modulation to be converted to a density modulation during the drift.

Simulations of the prebuncher and IFEL accelerator guided the prebuncher design. The modeled energy modulator, chicane, and IFEL helical undulator magnetic fields were then used with 3D simulations of the IFEL interaction using

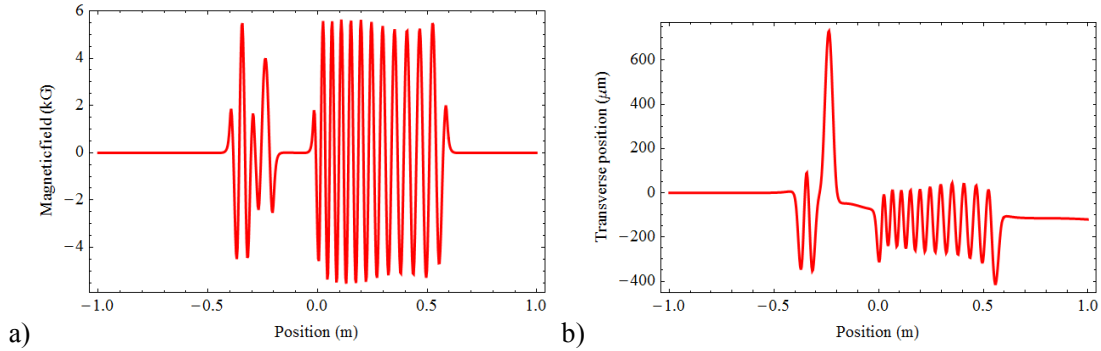


Figure 4.20: 3D simulations of a) the average magnetic field felt by the particles and b) the transverse position of the beam as it traverses through the buncher and helical undulator without laser. In the figures, the helical undulator is positioned at the origin while the energy modulator is positioned 40 cm upstream and the chicane 28 cm upstream of the IFEL undulator.

the General Particle Tracer (GPT) code [66]. Figure 4.20 shows the modeled fields along the beamline axis as well as the trajectory in the plane transverse to the on-axis prebuncher magnetic fields.

Simulations for a 235 GW laser show that with a chicane gap of 18.75 mm, 79% of the inject beam is accelerated to full energy as shown in Figures 4.21. Figure 4.21a shows the longitudinal phasespace of the electron beam just before entering the helical undulator. The electron density is concentrated in spikes along the beam and the red particles show the region of phase space which is accelerated to final energy. Figure 4.21b shows the final longitudinal phase space of the accelerated beam while Figure 4.21c shows the entire beam. Two GPT space charge routines were tried separately to investigate the effects of space charge on the accelerated beam. Neither meshed space charge fields nor pair-wise space charge calculations were found to significantly affect the properties of the output beam, suggesting that space charge should not play a significant role up to the energy spectrometer during the experiment.

The input laser power was varied in order to investigate the performance stabil-

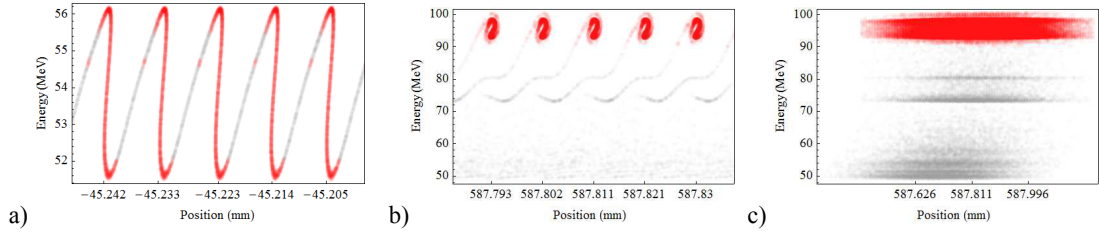


Figure 4.21: Simulations show the longitudinal phase space of a section of the e-beam initially one picosecond long a) just before and b) & c) just after the undulator which is positioned at the origin of the simulation coordinate system. The laser power used in the simulation is 235 GW, and the injected e-beam energy is 54 MeV. Position ticks in a) and b) are separated by one laser wavelength while ticks in c) are separated by 20 times the laser wavelength for scale.

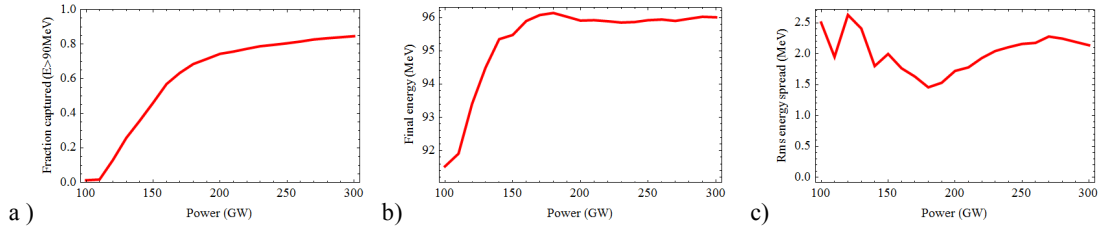


Figure 4.22: Laser peak power sensitivity scans show a) the fraction of injected electrons accelerated to full power, b) the mean energy of the accelerated fraction of electrons, and c) the rms energy spread.

ity of the prebuncher and accelerator combination. Figure 4.22a shows that once phase locked, at least half of the beam should be accelerated for laser power exceeding 150 GW. Furthermore, the average energy of the accelerated beam should remain a constant 96 MeV above this threshold (see Figure 4.22b). Finally, the rms energy spread of the accelerated beam, shown in Figure 4.22c, remains stable at around 2% for all laser powers. The simulations show that the prebuncher design should lead to relatively stable operation for various laser power fluctuations above 150 GW and may enable the capture of up to 85% of the beam for powers exceeding 300 GW.

The addition of a prebuncher to the Rubicon IFEL project should enable stable acceleration for the majority of the electron beam. The improved efficiency enables experiments requiring a significant amount of charge such as an IFEL driven inverse Compton scattering (ICS) experiment. The ATF has a long running ICS program, and recently the 3<sup>rd</sup> order harmonic was observed there [67]. Since the energy of photons scale as the energy of the electrons squared, doubling the e-beam energy increases the energy of produced gamma photons by a factor of 4. Furthermore, a prebuncher is a first step towards the demonstration of a planned compact high-efficiency electro-optical energy conversion experiment which will be studied later in Section 6.2.

## 4.5 ATF Linac and electron beam tune

The ATF linac uses a 1.6 cell s-band gun and two SLAC linac sections to produce electron beams with energies from 45 to 70 MeV with transverse normalized emittances of about a micrometer for 100 pC and somewhat larger at 1 nC [68]. The output beam can be sent to one of three experimental beam lines, and various diagnostics such as strip-lines, pneumatic beam position monitors, and a Faraday cup are available for monitoring the beam. We installed the undulator for the IFEL experiment on beam line 2, also known as the I-line, where the LACARA experiment previously demonstrated acceleration of up to 2 MeV in a 5 T superconducting solenoid with the ATF's CO<sub>2</sub> laser system [69]. As such, the beam line already had optics for CO<sub>2</sub> laser transport.

The experimental setup is shown in Figure 4.23. The electron is kicked onto the experimental beam line by a dipole magnet with a restricting aperture of 2.65 cm in the vertical plane. The laser is focused by a lens prior entering the vacuum system thru a high damage threshold NaCl window. In order to keep the laser intensity as high as possible, we placed the undulator as close to the

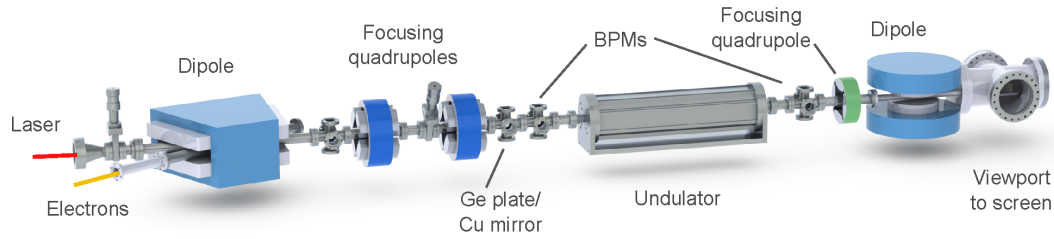


Figure 4.23: 3D model of the beam line with quadrupoles and undulator installed.

dipole as possible. To this end, we used a quadrupole doublet instead of a triplet and the bare minimum number of diagnostic crosses needed for the experiment: 2 beam position monitors, 1 vacuum pump and ion gauge. The undulator, another beam position monitor, final focusing quadrupoles, and spectrometer composed of a dipole and scintillator screen within an 8 inch 4-way cross complete the layout.

We modeled the electron beam transport using Elegant, an accelerator code that does 6-D tracking with matrices and/or canonical integrators, and supports a variety of time-dependent elements [70]. The left side of Figure 4.24 shows the designed beam focusing up to the undulator’s entrance. The lattice was designed by varying the quadrupole doublet to achieve a beta function of 0.45 m at a waist (alpha of zero) in both planes in order to match into the undulator. Unfortunately, the shortest beta function that the doublet could achieve was 0.9 m. Simulations showed that this would not affect the acceleration but would likely lead to an increase in the normalized transverse emittance of the accelerated beam. During the experiment, we approximately achieved this beam tune as shown on the right side of the figure, yet the beta function achieved right before the undulator was estimated to be closer to 2 m. Again, simulations showed that this shouldn’t significantly affect the acceleration of the electron beam.

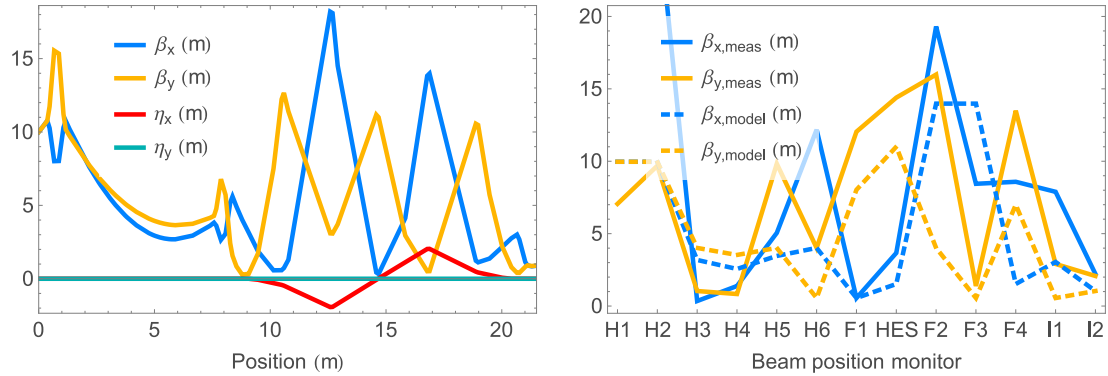


Figure 4.24: Twiss parameters for the experiment (left) and estimated beta functions at various beam position monitors along the beam line (right).

## 4.6 Energy spectrometer

The large variation in electron energies (40 to 120 MeV) expected after acceleration necessitated a wide range spectrometer. A large dipole magnet introduced dispersion into the beam which then scintillated on a phosphor screen and was imaged with a CCD camera. The energy was then calculated from the position of the electron beam on the screen.

The dipole magnet is a circular electromagnet with 14 inch diameter pole faces separated by a gap of 1.5 inches. A current-field scan revealed a linear field response of 420 G/A for currents up to 6.5 A. Energy resolution was optimized by typically operating at or near 6 A (2.52 kG) for most of the experiment to maximize dispersion. For the decelerated portion of the electron beam extending to 40 MeV, this results in a 15 degree bend. A wedge shaped vacuum chamber (shown in Figure 4.6) was built to accommodate these energies while still transmitting the laser on axis.

We calibrated the spectrometer by varying the dipole field to scan the beam across the scintillator screen. As the electrons bend in the magnetic field, they traverse a circular arc with radius of curvature given by  $r = p/qB$ . Scanning a

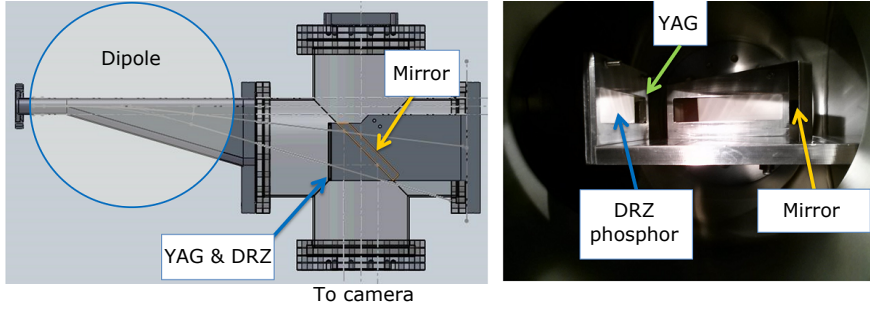


Figure 4.25: Spectrometer layout and optics.

fixed energy beam across the scintillator by varying the magnetic field yields the radius of curvature which can be used to infer the energy of the accelerated beam for a fixed dipole magnetic field. The deflection of a particle through the dipole is approximately given by  $\Delta x = 2\Delta s R/r = 2\Delta s qBR/p$  where  $R$  is the dipole magnet radius. Since the dipole is circular, the path length  $\Delta s$  through the dipole is independent of energy to a reasonable approximation, and change in position on the screen should be linear in  $B$  and inversely proportional in the momentum  $p$ . We see in Figure 4.6 that the position of the beam on the screen does indeed vary linearly with respect to dipole current, and a linear fit was used to calculate the calibration curve:  $pc = 63600\text{MeV}/(1503 - x)$ .

When examining charge density as a function of energy, it is necessary to calculate the Jacobian between pixel and energy as so  $\frac{dN}{dp} = \frac{dN}{dx} \frac{dx}{dp} = \frac{dN}{dx} / \frac{dp}{dx}$ . In order to calibrate the charge, we placed the entirety of the beam on a section of the screen taking care to avoid camera saturation. We then integrated the background subtracted ADC pixel counts for several shots to estimate the response of the screen and compared this to the average of multiple Faraday cup charge measurements. Assuming a linear charge to signal dependence and relative insensitivity of the screen photon yield to the energy of the incoming beam, this analysis yields a number of electrons per ADC count.

We also measured fiducial marks on the screen in order to calibrate for beam

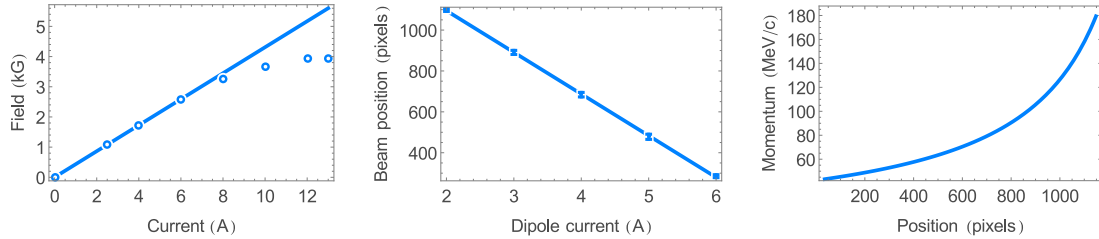


Figure 4.26: Shown above are the magnet field calibration and spectrometer energy calibration.

dispersion and vertical spot size in order to enable an energy dependent transverse emittance measurement. In order to improve the energy resolution of the spectrometer, we inserted a quadrupole between the undulator and spectrometer dipole to minimize the beam size in the dispersive plane at the spectrometer screen. Elegant and GPT simulations showed that the spot size of the accelerated beam should be approximately  $560 \mu\text{m}$  in the horizontal, dispersive plane. Simulations showed that with this final quadrupole inserted, the spot size should be halved to  $230 \mu\text{m}$ , thereby improving the energy resolution by a factor of two. With a dispersion of about  $1.8 \text{ MeV/mm}$  at  $90 \text{ MeV}$ , this allows the spectrometer to image spectra details with about  $0.4 \text{ MeV}$  wide.

The high gradient experimental run utilized a single DRZ phosphor scintillator screen. In order to avoid damage of the screen from the electron beam for the high capture experiment, we decided to use a YaG crystal to image the lower energy section of the beam and DRZ with the side covered in a thinner layer of plastic now facing the camera for the accelerated portion of the beam (see right side of Figure 4.6), taking care not to hold the beam on the DRZ. A downside to this approach was that much of the light produced in the YaG was channeled to the edges and illuminated the boundary near the DRZ. In hindsight, it would have been good to use a small mask to keep the YaG signal from polluting the DRZ. In more recent experiments, we removed the YaG and used the DRZ exclusively. We calibrated the DRZ and YaG separately, and found that the signal from the DRZ

was an order of magnitude larger than the YaG. The response of the 12-bit camera spanned 3 orders of magnitude, and we attenuated the spectrometer images with ND filters to maximize signal without saturating the camera.

## 4.7 CO<sub>2</sub> laser

### 4.7.1 Laser transport

The CO<sub>2</sub> laser produced from the exit of the main amplifier NaCl window has a waist size of about 1.5 cm and propagates roughly 23 m with a half-angle divergence of order 1 mrad to about to a waist size of about 4 cm on the NaCl window at the entrance to the beam line. The transport line consists of about a dozen polished copper mirrors each of 3 inch diameter or larger. Each mirror is adjusted to align the CO<sub>2</sub> laser through a series of irises which in turn are aligned to the centers of the mirrors with the use of a HeNe laser. The final mirror is motorized with two Newport Picomotor Piezo Linear Actuators in order to finely control the angle of the mirror with respect to two orthogonal axes for final alignment down the beamline.

Diagnostic laser pick-out points included a kinematic mount insertable in air just before the thick NaCl vacuum window sealing the beam line and a pop-in copper mirror in vacuum 15 cm upstream of the undulator. The first was right before the final focusing optics and accommodated a 3 inch silicon mirror for imaging the laser with a pyroelectric camera or a 3 inch NaCl window for picking off a reflection to be used as a reference signal during germanium timing. The vacuum popin mirror near the undulator was used to extract the laser through a zinc sulfide Cleartran window, transmissive to 10  $\mu\text{m}$ , to a Spiricon Pyrocam III pyroelectric camera which could slide along a rail next to the undulator to monitor the evolution of the spot size close to the focal region.

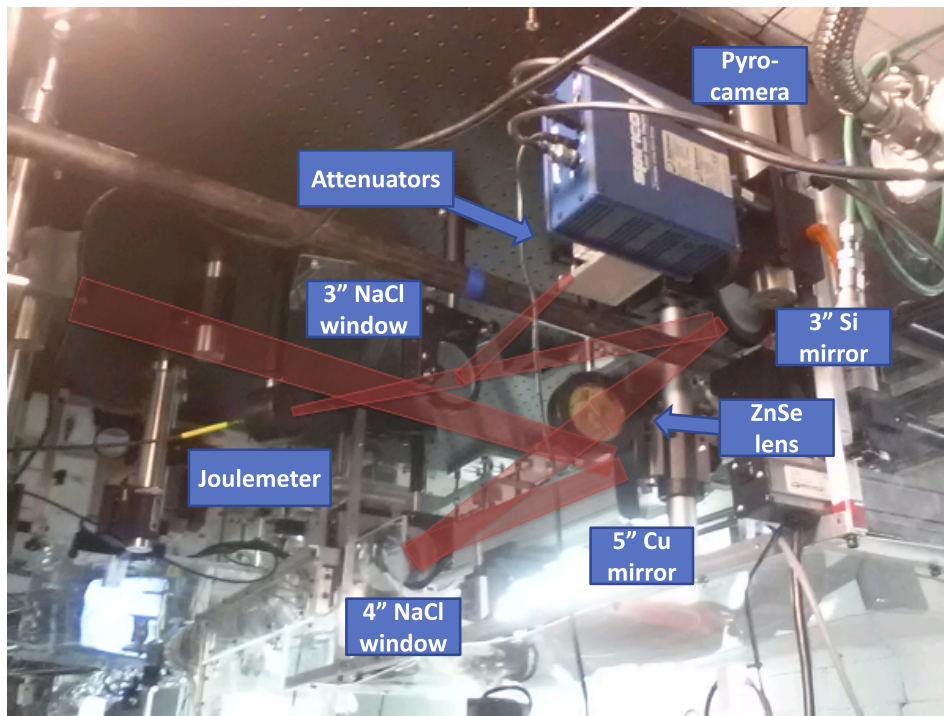


Figure 4.27: Diagnostics near the experiment for monitoring the pulse energy and transverse profile.

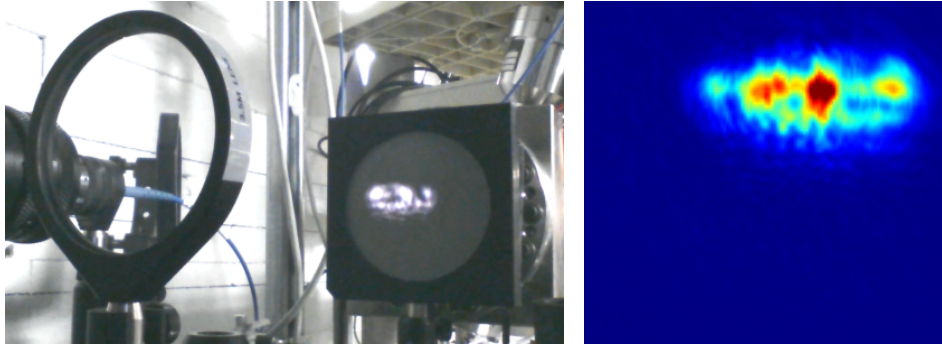


Figure 4.28: Laser pulse energy calibration and transverse profile monitoring.

The beam line is defined by an iris positioned 3 m upstream and another positioned 5 m downstream of the undulator, and a HeNe laser is aligned to these reference points in order to align components to the beamline. On the other hand, the final CO<sub>2</sub> alignment iris and lens are located 4.5 m upstream of the undulator. In order to align the CO<sub>2</sub> laser to the beam line within the undulator, irises on the rail in the focal region are aligned to the beam line HeNe, and the CO<sub>2</sub> (imaged with the Pyrocam) is coaligned to these irises using the Picomotor controlled mirror near the final focusing lens.

Additionally during the experiment designed for high capture, we setup online diagnostics to monitor the laser within the experimental hall. Several meters upstream of the lens, we focused the reflection from a NaCl window onto a calibrated joulemeter in order to measure the pulse energy. During laser operation, shock waves within the amplifier may move mirrors, disturbing beam alignment, and the mode quality may degrade if the beam clips on one or more the mirror apertures as it propagates to the experimental hall. We placed another NaCl window in the path of the aforementioned reflection to produce a secondary reflection which we then attenuated with filters and placed on a Pyrocam. This allowed us to monitor the laser mode quality within the experimental hall during the experiment and helped to diagnose alignment problems as they developed.

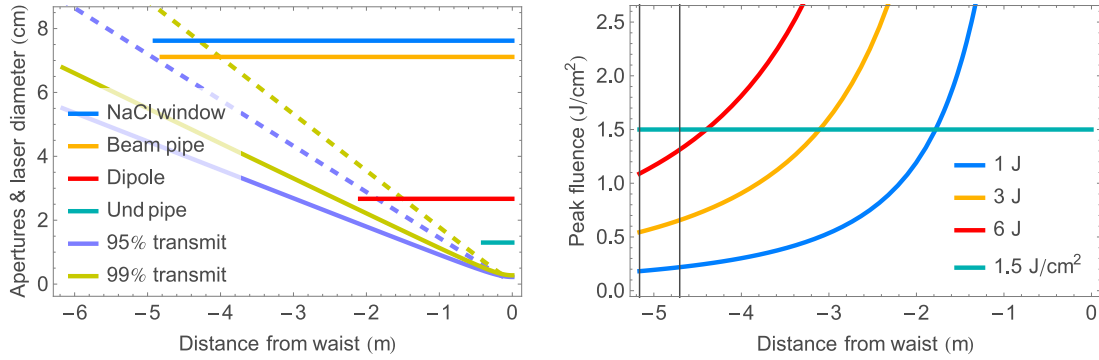


Figure 4.29: The clear apertures (diameter) of various beam line elements are shown left along with the diameters of a circular laser cross sections containing 95% and 99% power transmission for 25 cm Rayleigh range (solid lines) and for 9.6 cm Rayleigh range (dashing). The peak fluences for various laser pulse energies are shown right, and the gray vertical lines on the left represent the transport line’s last mirror as well as the NaCl vacuum window.

#### 4.7.2 Laser focusing

Upon arriving at the ATF, we surveyed the laser optical path up to the undulator installation point in order to ensure clear transmission to the undulator. The pipe and dipole apertures measured during the survey are shown plotted relative to the undulator midpoint in Figure 4.29. The survey revealed that the dipole used to kick the beam onto the beam line had a vertical limiting aperture of 2.67 cm. Since beam position monitors, quadrupole magnets, and vacuum components needed to be placed between the dipole and undulator, their entrance-to-entrance distance needed to be made larger than 2 m. This placed an upper limit of about 13 mrad on the full beam divergence, necessitating a longer Rayleigh range of about 25 cm. In the figure, beam diameters containing 95% and 99% of the laser power are shown plotted for this 25 cm Rayleigh range with solid lines and for 9.6 cm Rayleigh range with dashed lines. We chose a relatively large buffer to permit passage of mixed laser modes with  $M^2$  up to 1.5.

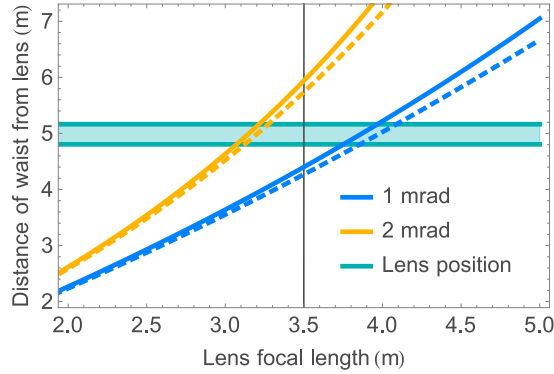


Figure 4.30: Plot showing the lens to waist focal distance vs thin lens designed focal length. The solid lines are for a fundamental Gaussian mode while the dashed lines show  $M^2 = 1.5$ .

The amplified laser pulse is transported with a large spot size of two inches in order to avoid damage to beam line elements by keeping peak fluences low. The final lens was positioned after the last copper mirror and the NaCl vacuum window. This position keeps laser fluences far below the damage thresholds for Cu mirrors ( $4.5 \text{ J/cm}^2$ ) and NaCl elements ( $1.5 \text{ J/cm}^2$ ). The right plot of Figure 4.29 shows the peak fluence for a 25 cm Rayleigh range and various laser pulse energies. Placing the lens 4.9 m upstream of the waist position keeps the optical elements safe from damage for laser pulse energies up to at least 6 J and gives a positioning error cushion of about 17 cm up and downstream.

After choosing the lens position, we used Gaussian beam propagation matrices to determine the lens focal length needed to place the waist position 4.9 m downstream of the lens [71]. Figure 4.30 shows the result of this calculation for the laser estimated by ATF to be about 2 inches diameter with a divergence of 1 to 2 mrad at this position. The horizontal band shows the region between the mirror and vacuum window where the beam can be easily placed without beam line modification. We chose a 3.5 m focal length in order to keep the actual lens position as close to the designed position as possible. The lens design was a 3 inch diameter biconvex NaCl lens with high power anti-reflective coating. The lens was

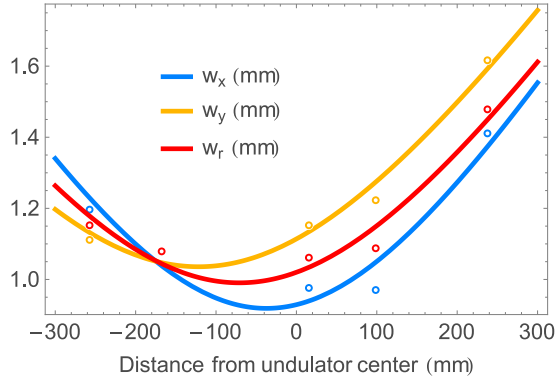


Figure 4.31: Waist scan showing the  $1/e$  spot size evolution with the undulator midpoint at the origin.

translated along a rail in order to focus the laser to a waist at various positions along the undulator.

Once the lens was installed, we performed a laser waist scan by picking out the laser near the undulator and imaging the laser’s transverse profile with a Spiricon Pyrocam III. The results of the scan are shown in Figure 4.31 and a summary of the fit parameters is given in Table 4.7.2. The waist position for both transverse planes was found initially several centimeters upstream of the undulator midpoint, giving ample room for positioning the lens. A slight astigmatism in the focused beam led to slightly different focal properties for the two transverse planes. We also calculated the average deviation of the  $1/e^2$  intensity contour from the beam’s centroid in order to estimate the radial waist which more accurately represents the on-axis intensity. The result is a beam with Rayleigh range 30 cm and minimum waist approximately 0.99 mm with otherwise good mode quality. The imaged mode was produced by sending the output of the CO<sub>2</sub> oscillator to the beamline via the main CO<sub>2</sub> amplifier and should approximate that of the amplified pulse. We later verified these results using the output of the regenerative amplifier.

During amplification, higher order modes may be excited within the main amplifier and nonlinear focusing due to intensity sensitive effects may distort the

	$x$	$y$	$r$
$w_0$ (mm)	0.92	1.04	0.99
$z_0$ (mm)	-37	-122	-71
$z_r$ (mm)	257	327	299
$M^2$	1.04	1.06	1.04

Table 4.8: Laser waist scan results

beam by focusing various parts differently. In order to estimate the effect that this may have on the laser during the experiment, we measured the amplified laser pulse spot size by propagating a reflection from the focused laser in air to a waist at the pyroelectric camera with sufficient attenuation to prevent damage and saturation to the sensor. The measured spot size for the amplified pulse was in good agreement with the low power measurements (within 6%); however, the power in the tails (estimated by fitting a Gaussian to the core of the beam) near the minimum waist position grew to 12% (at 2.8 J) to 17% (at 4.7 J) of the total power in the beam.

### 4.7.3 Temporal laser pulse diagnostics

The laser peak power is an important parameter affecting the performance of the IFEL so in addition to energy, it is useful to study the temporal structure of the laser pulse. ATF employed two methods to this task [50]: the first was to study the spectrum of the amplified pulse, while the second method investigated pulse splitting by imaging the temporal profile using a streak-camera.

A small fraction of the laser energy was taken via a reflection of the amplified pulse from a NaCl window and was sent to a spectrometer composed of a diffraction grating and a pyroelectric camera. The pulse duration may be inferred from the spectral bandwidth by assuming that the time-bandwidth product of the amplified pulse is limited by the uncertainty principle for Gaussian pulses

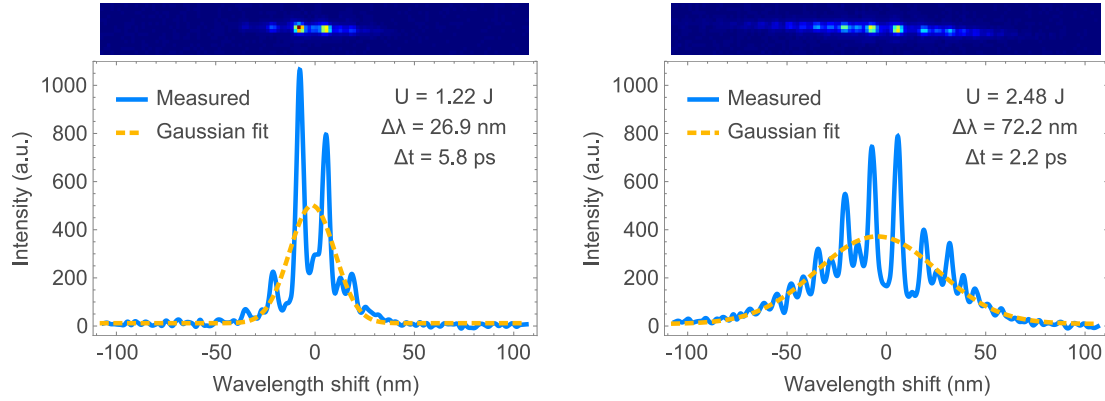


Figure 4.32: Measured spectra for two amplified shots at different laser energies.

$\Delta f \Delta t \geq \ln(4)/\pi \approx 0.44$ , where the quantities  $\Delta f$  and  $\Delta t$  are the full width at half maximum values of the frequency bandwidth and pulse length respectively [71]. Additionally, we may use the relation  $\Delta f \approx c\Delta\lambda/\lambda^2$  for wavelength bandwidth  $\Delta\lambda$  small relative to the central wavelength  $\lambda$ .

Two such shots are shown in Figure 4.32. The higher energy shot (right) has twice the energy of the lower energy shot (left), yet spans a much larger bandwidth covering more lines from the CO<sub>2</sub> rotational spectrum. The larger bandwidth implies a shorter pulse length and overall much larger peak power.

We imaged a series of shots over two consecutive days, recording final amplifier high voltage and output power as well as the power of the pulse from the regenerative amplifier seeding the main amplifier for each shot. The fit fwhm bandwidth for the shots are shown in Figure 4.33, with the point at zero output energy corresponding to the unamplified output of the regenerative amplifier. The bandwidth grows due to saturation or power broadening during amplification and appears to grow quadratically with output pulse energy as  $\Delta\lambda \approx 23.5 + 4.3U^2$  where the energy  $U$  is measured in J and bandwidth is measured in nm. Assuming that the output pulse is bandwidth limited yields a relation between pulse duration (in ps) and laser energy of  $\Delta t \approx 6.6/(1 + (U/2.4)^2)$ . Alternatively, the spectral broadening may also be explained by self-phase modulation, resulting in a chirped

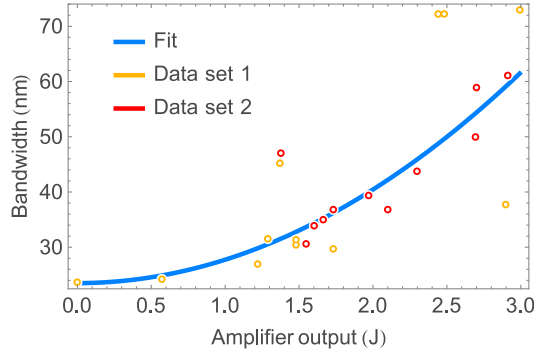


Figure 4.33: Fit bandwidth is plotted versus output pulse energy.

rather than Fourier transform limited pulse. As will be shown in Section 5.1, measurements of the IFEL interaction suggest that the power grows approximately linearly with respect to output laser energy.

We used a Hamamatsu C1587 streak camera to further investigate the pulse structure [50]. A reflection of the amplified pulse from a NaCl window was sent to the streak camera where it was mixed with 900 nm light from a CW diode laser in a AgGaS<sub>2</sub> to upconvert to a frequency high enough to extract electrons from a photocathode. The extracted electrons were then accelerated and imaged on a scintillator. The streak camera is operated near the signal threshold to avoid space charge effects. The resulting signal granularity yields a temporal resolution of about 2 or 3 ps; nevertheless, this is fine enough to detect the expected picosecond structure.

Figure 4.34 shows the streak camera data for two shots revealing a pulse train temporal structure referred to as pulse splitting. Since the IFEL only uses one of these peaks, it is important to estimate the energy of the leading pulse which tends to be the largest. The peaks are separated by 25 ps corresponding to the frequency separation of rotational lines in the 10R branch of the CO<sub>2</sub> gain spectrum. The left, lower power shot appears to only have two such pulses, with the leading pulse containing up to 80% of the energy. This number is a reasonable estimate but suffers from some uncertainty due to the streak camera setup's relatively

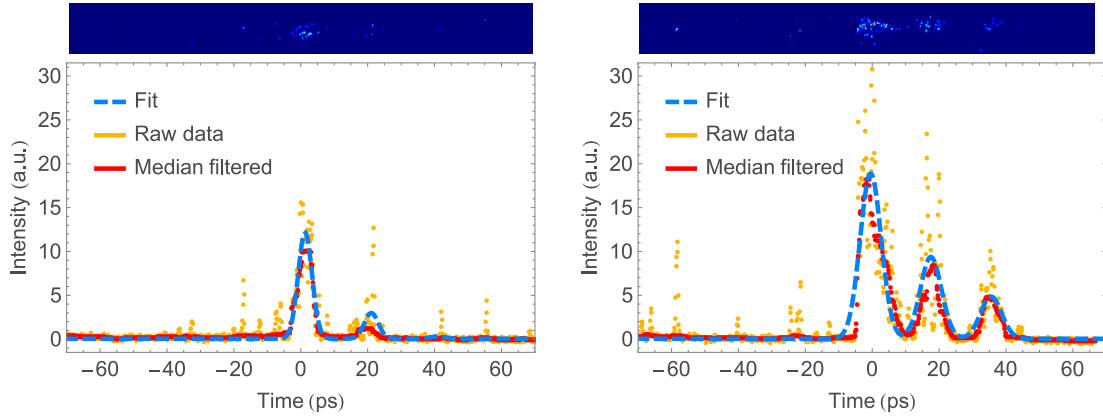


Figure 4.34: Streak camera images for two different shots.

low sensitivity and may be a slight overestimate since it is possible that some prepulsing from spontaneous amplification arriving before the seed contains some energy. The right plot shows a high energy output with about 3 or 4 times larger total energy, yet the leading pulse peak power may be about twice that of the first as much of the energy is in two trailing pulses. In this case, the leading pulse contains no more than about 60% of the laser energy.

#### 4.7.4 Laser energy measurements

Since the IFEL performance is very sensitive to the input laser pulse energy, we recorded this parameter for every shot during the experiment. The measured pulse energies for shots during the the two IFEL runs are shown in Figure 4.35. The first, high capture, run used a pulse energy measurement in the laser room only a few optical elements after the main amplifier. Some of this energy may have been lost on many apertures (all mirrors used had at least 3 inch diameters, but due to the 45 degree orientation for 90 degree reflection, have only a 2.1 effective aperture) as the laser was propagated to the experimental hall where the undulator resided. As a result, the energy delivered to the experiment was reduced relative to this measurement.

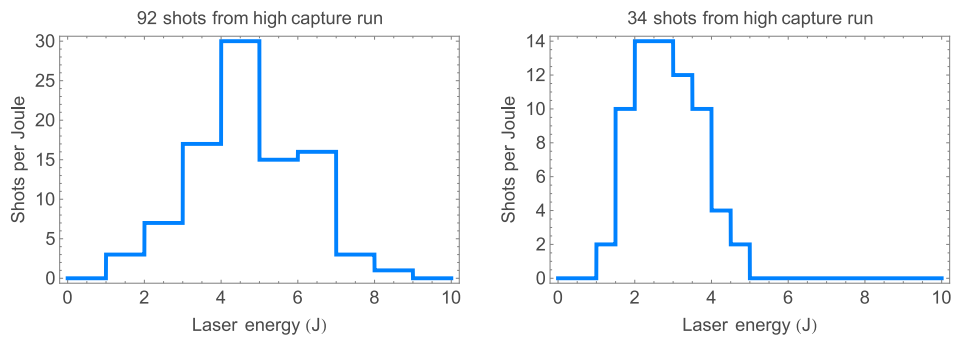


Figure 4.35: Measured laser energy from the high gradient run measured near the main amplifier (left) and from the high capture run measured in the experimental hall (right).

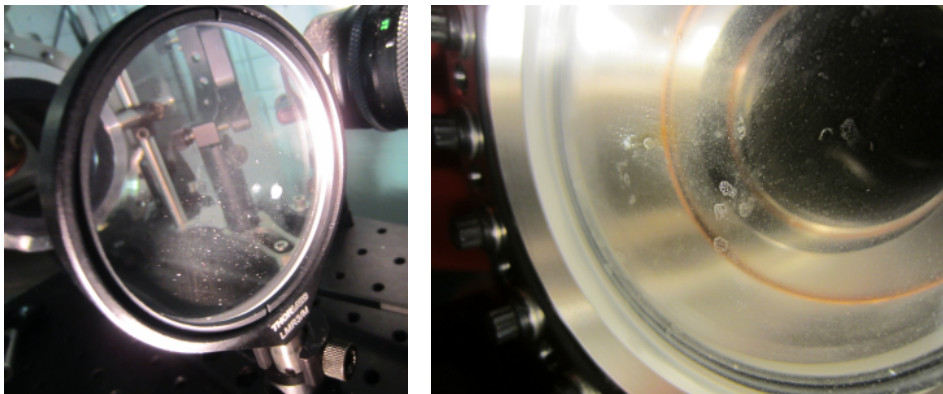


Figure 4.36: Localized damage to the final focusing lens (left) and NaCl vacuum window (right) acquired during the first, high capture run.

For the subsequent high capture experiment, we installed a joulemeter in the experimental hall to measure the laser pulse energy and calibrated it by dumping the entire pulse energy, which would otherwise be sent into the beamline vacuum, into another, calibrated joulemeter. Since the calibration joulemeter was placed just upstream of the NaCl vacuum window, this calibration accounts for all aperture cuts and reflections from the final focusing NaCl lens. On the other hand, it ignores reflections from the vacuum window which may amount to a reduction of up to 4% per surface ( $\sim 8\%$  total) of the measured energy. This estimate may be conservative since the window sustained damage during the first run as shown in Figure 4.36, creating imperfections within the NaCl which may reduce transmission locally.

# CHAPTER 5

## Experimental results

In this chapter, we present some of the results of the UCLA-BNL IFEL experimental campaign. In the first two sections of this chapter, we examine efforts to establish acceleration and optimize the accelerator's performance by varying the input parameters such as synchronization between electron and laser pulses and laser polarization. Next, we examine the spectrum of the IFEL accelerated electrons for the high gradient undulator configuration and compare these spectra to simulations to gain insight into the dynamics. Since the laser focal parameters did not match the design, the accelerator's performance suffered, necessitating a redesign of the undulator tapering and a second experiment. In the final two sections, we discuss the results of the high capture experiment utilizing this second, more relaxed undulator tune as well as a measurement of the accelerated beam's transverse emittance.

### 5.1 Synchronization

Temporal synchronization between electrons and laser was crucial to the success of the experiment as it placed the electrons in the region of the laser pulse with maximum electric field. We accomplished synchronization by first measuring the electrons by a strip-line just upstream of the dipole and measuring the laser pulse using a fast photodiode positioned near the undulator's midpoint. The laser is redirected to the photodiode through a ClearTran vacuum window via a 1 cm diameter Cu mirror inserted in the beam path. The output of the regenerative

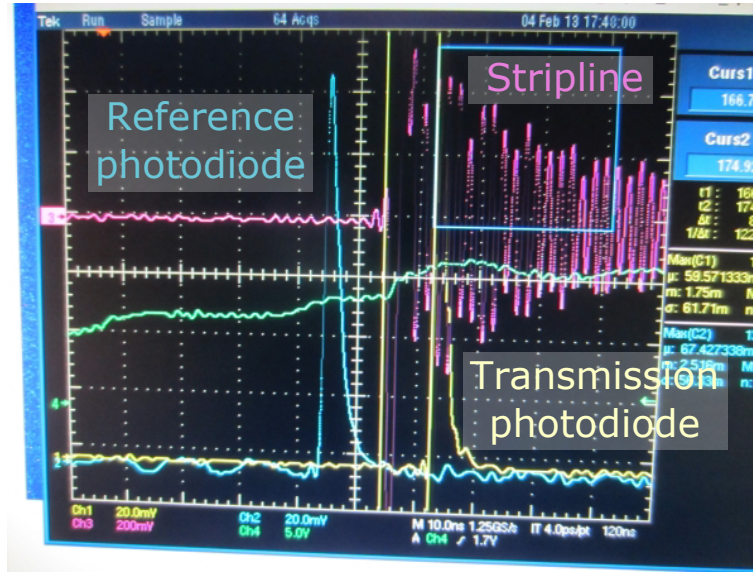


Figure 5.1: Oscilloscope showing signals from the strip line and photo diode (labeled transmission). A signal from a photo diode upstream of the Ge plate was used as a reference to measure the suppression of the laser through the Ge plate.

amplifier was transported through the main amplifier without amplification so that the path length of the laser is the same as that for the amplified pulse. The cables were chosen to have equal lengths so that the signals' relative delay would not be altered. We measured the distance between the strip line and photo diode and calculated the time that light (and ultrarelativistic particles) would take to traverse this distance. We then changed the laser delay (by changing the timing of the YaG slicing for large steps and then via a long delay stage for fine steps) until the measured time of arrival difference between the electrons and laser was equal to the time-of-flight distance between the two detectors. In this way, the two beams were synchronized to within about 1 ns.

Since the pulses are each on the order of a picosecond long, the nanosecond synchronization is insufficient to overlap the pulses longitudinally and achieve IFEL interaction. Finer timing was accomplished by measuring the electron-beam modulated transmission of the laser through a thin germanium plate inserted into the

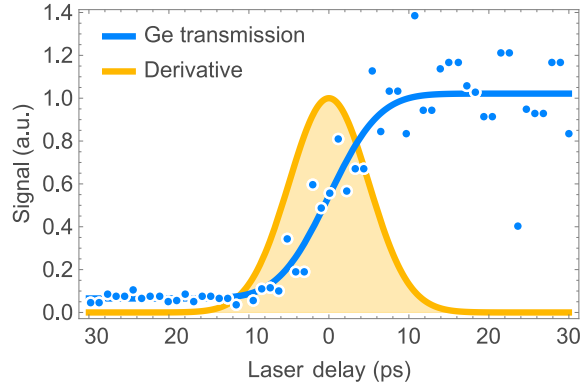


Figure 5.2: Plot showing the Ge transmission and IFEL acceleration data versus laser delay.

beam line [72, 73]. The plate itself is placed about half a meter upstream of the undulator and masked by an aluminum plate with a 2 mm diameter hole aligned to the beamline HeNe. Figure 5.2 shows the results of the Ge facilitated synchronization for the high gradient IFEL run. When the 10.3  $\mu\text{m}$  laser is incident on the Ge plate, a fraction of the light is transmitted downstream to the fast photo diode as shown on the right side of the figure. A reflection of the laser upstream of the NaCl vacuum window focused onto another fast photo diode served as a reference to monitor the laser energy incident on the Ge and is used to normalize the unattenuated transmitted signal.

We then varied the laser delay until the transmitted laser signal was extinguished. At this point, the electrons arrive earlier than the laser, creating an electron-hole solid state plasma in the Ge which modifies the optical properties of the semiconductor increasing the absorption and reflection. The plasma is formed on a time scale faster than 100 fs and persists for nanoseconds so is perfect for picosecond precision synchronization. Synchronization is then achieved by varying the laser delay to find the threshold where the laser transmission is barely suppressed. The resulting curve can be considered a temporal cross-correlation of the electron and laser pulses. An error function fit and its derivative are both

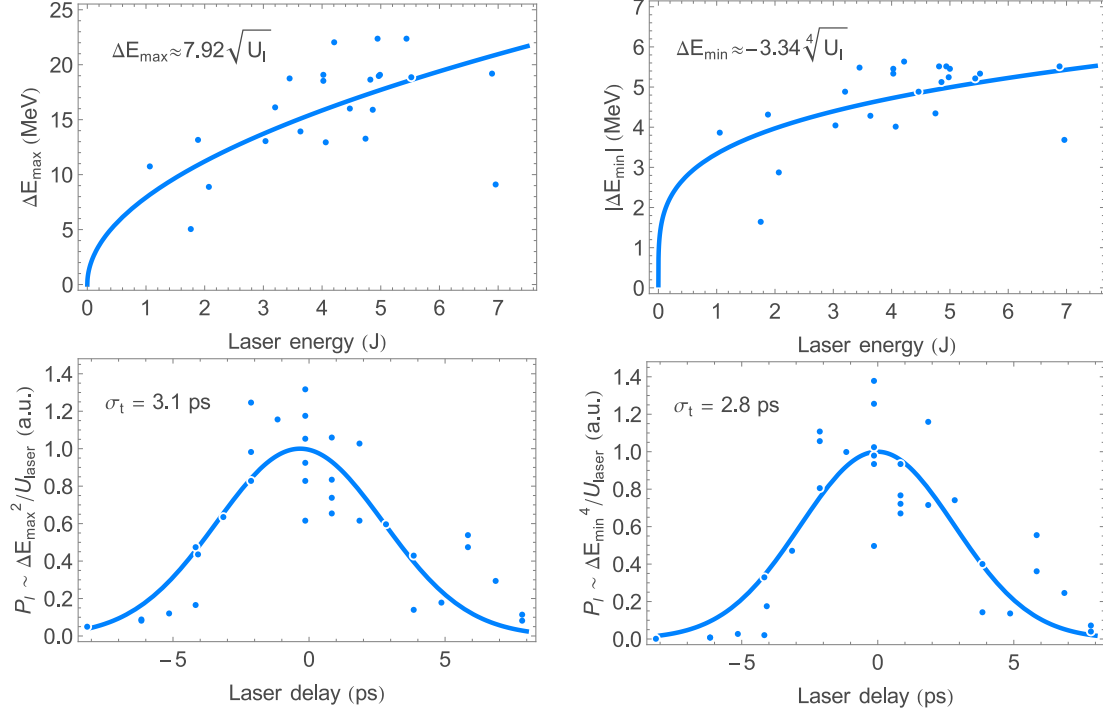


Figure 5.3: Plots IFEL acceleration metrics (max and min energy changes) versus laser delay as well as corresponding acceleration vs laser energy correlation plots.

shown in the figure and yield an rms length of the interaction region of 4.7 ps. Since the estimated electron beam time of arrival jitter is on the order of 1 ps, this value is an upper bound on the laser pulse length.

Upon achieving synchronization, we removed the Ge plate and switched to high power laser operation. The Ge has an index of refraction of 4.0 at 10.3  $\mu\text{m}$  [74] so the plate's couple hundred micron thickness may possibly delay the laser on a picosecond time scale, necessitating another temporal delay scan during initial IFEL operation. As a byproduct of this scan, we may learn more about the laser temporal pulse structure via the interaction. The results of a scan of IFEL acceleration versus laser delay are shown in Figure 5.3.

The peak laser power used in this measurement was below the threshold for full acceleration so that the IFEL operates in a regime where the induced energy

gain of the electrons depends on the peak laser power. The accelerating gradient is proportional to the laser field amplitude, and indeed independently from the laser delay, we see a square root dependence of the maximum energy gain on laser energy in the bottom right of Figure 5.3 with maximum energy gains of merely a third of the accelerator’s design. Normalizing each shot by the square root of the laser energy removes this correlation, reducing variance due to shot-to-shot laser energy fluctuations, and results in normalized energy gain versus laser delay. On the other hand, the temporal pulse shape is determined by the laser power which is proportional to the square of the accelerating gradient and energy gain. The bottom left plot in the figure shows the square of the normalized energy gain as a proxy for the laser power versus laser delay. A Gaussian fit yields an rms width of 3.1 ps. The width of the curve is the convolution of the pulse widths of the laser and electron beams as well as their relative time jitter. Since the electron beam’s time of arrival jitter is on the order of 1 ps, the fit result may be considered an upper bound on the average rms laser pulse length.

In order to verify the results of this measurement, we examine the maximum decelerated energies. As particles begin to undergo synchrotron rotations within the ponderomotive bucket, some electrons are decelerated to nearly the energy of the bucket’s separatrix, and these particles may detrap within one or two undulator periods as the resonant energy increases. As a result, this measurement should depend only on the laser power and be independent of the change in the resonant energy gradient near the undulator’s midpoint. The separatrix height increases with the square root of the laser field strength as shown in Equation 2.35 so the maximum electron deceleration should approximately scale as the fourth root of the laser energy assuming that the laser power is simply proportional to the laser energy. The top right plot of Figure 5.3 shows that this is indeed a reasonable assumption. Normalizing the maximum energy loss by the fourth root of the laser energy removes the laser energy dependence. The fourth power of this

scaled energy then is a measure of the laser power and is shown in the bottom right of the figure. A Gaussian fit to this yields an estimated rms pulse width of 2.8 ps, slightly smaller than, yet similar to the previous estimate.

## 5.2 Polarization

The helical IFEL interaction as presented in Chapter 2 requires a circularly polarized laser with a particular handedness. To realize this polarization in the experiment, we used a zeroth order quarter wave plate to convert the polarization of the output of the regenerative amplifier from linear to circular. When the input linear polarization of the laser is aligned with the wave plate's fast or slow axis, the output polarization remains linear, whereas when the polarization makes a 45° angle with the axes, the output polarization is circular. For all other angles, the output polarization is elliptical. In this section, we will first discuss the IFEL interaction with the helical undulator and an elliptically polarized laser, and then show the effect of the laser polarization on the measured spectra.

### 5.2.1 Elliptical IFEL acceleration

The linearly polarized laser vector potential is the real part of the complex phasor

$$\vec{A}_l = \frac{\sqrt{2}mcK_{l,\text{rms}}}{|q|} u(\vec{x}) e^{i\Phi(\vec{x},\zeta)} \hat{x} \quad (5.1)$$

where  $K_{l,\text{rms}} \equiv |q|E_{\text{rms}}/mc^2k$ ,  $\zeta = kz - \omega t$ ,  $u(\vec{x})$  is a pulse form factor, and  $\Phi(\vec{x}, \zeta)$  is a phase factor.

A quarter waveplate is a thin piece of birefringent material with differing indices of refraction for two orthogonal axes in the material. The two axes are called fast and slow as the field component polarized along the slow axis is delayed in phase by  $\pi/2$  relative to the component along the fast axis. To make circularly polarized light, the quarter waveplate is rotated so that the linearly polarized light's

electric field is oriented  $45^\circ$  relative to either axis. Here, the incident light's polarization is rotated by an angle  $\alpha$  relative to the x-axis which is taken to be the slow axis.

$$\vec{A}_l = \frac{\sqrt{2}mcK_{l,\text{rms}}}{|q|} u(\vec{x}) e^{i\Phi(\vec{x},\zeta)} (\hat{x} \cos \alpha + \hat{y} e^{i\pi/2} \sin \alpha) \quad (5.2)$$

Inserting the field (the real part of Equation 5.2) into Equation 2.15 yields the energy evolution of an electron in the combined undulator and laser fields.

$$\begin{aligned} \frac{d\gamma}{dt} &= -\frac{q}{mc^2} \dot{\vec{x}} \cdot \frac{\partial \vec{A}}{\partial t} \\ &= -\frac{\sqrt{2}ckK_{l,\text{rms}}K}{\gamma} u(\vec{x}) (\cos \psi_u \cos \alpha \sin \Phi + \sin \psi_u \sin \alpha \cos \Phi) \end{aligned} \quad (5.3)$$

Here, we've ignored the initial velocity which may be made small. The product of harmonic factors with phases  $\psi_u = \int_0^z k_u dz$  and  $\Phi$  produce two beat-waves with phases given by Equation 5.5.

$$\frac{d\gamma}{dt} = -\frac{ckK_{l,\text{rms}}K}{\gamma} (\cos(\alpha - \pi/4) \sin \psi_+ + \cos(\alpha + \pi/4) \sin \psi_-) \quad (5.4)$$

$$\psi_{\pm} = kz \pm \int_0^z k_u dz - \omega t \quad (5.5)$$

The result is a summation of two ponderomotive waves from the combined action of the undulator magnetic field and laser electric field on the electrons. The first wave has a superluminal phase velocity and is therefore only resonant with tachyons. The second wave has a phase velocity with which known physical particles can match. Consequently, the subluminal wave may accelerate properly matched particles while the superluminal wave averages to zero and is ignorable. As a result, we will define the ponderomotive phase as  $\psi \equiv \psi_+$ . The energy gradient and ponderomotive phase may then be written as the following.

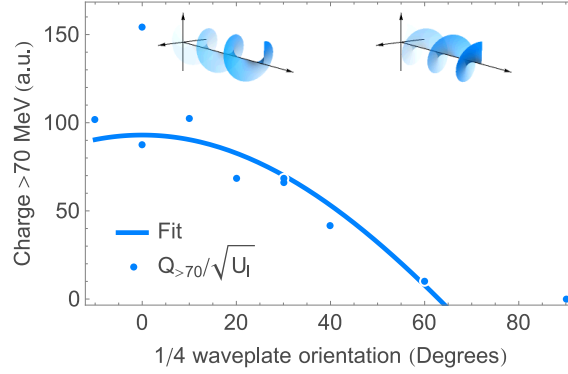


Figure 5.4: Polarization scan showing charge accelerated above 70 MeV versus quarter waveplate orientation.

$$\frac{d\gamma^2}{dz} = -2kK_{l,\text{rms}}K \cos(\alpha + \pi/4) \sin \psi \quad (5.6)$$

$$\psi = kz + \int_0^z k_u dz - \omega t \quad (5.7)$$

The acceleration is fully suppressed when the angle of the incident polarization is  $\alpha = 45^\circ$  relative to the quarter waveplate's slow axis, while for  $\alpha = -45^\circ$ , the wave is maximized. For  $\alpha = 0$  the light is linearly polarized, and the accelerating gradient is suppressed by a factor of  $1/\sqrt{2}$  in this case.

### 5.2.2 Polarization scan

We now turn to measurements of the elliptical IFEL accelerated spectra. We first determined the quarter waveplate orientation which produced circularly polarized laser by extinguishing the laser with a polarizer and then inserting the quarter wave plate upstream and rotating it to maximize transmission. Rotating a further  $90^\circ$  from this position in either direction changes the handedness of the circular polarization, yet since the light's phase is difficult to measure, we chose to determine this empirically via the IFEL interaction.

Figure 5.4 shows the effect of polarization on a measure of the IFEL interaction. The polarization is determined by the quarter waveplate orientation with the origin defined as the first axis we tried. Since these shots were operated below the full capture intensity threshold, the charge accelerated to high energies is very sensitive to laser polarization and we increased camera gain to be sensitive to this charge. As a result, the camera saturated for charges less than 70 MeV and we chose to examine the charge accelerated above 70 MeV as a measure of the IFEL interaction. Fluctuations in parameters such as laser power and spatiotemporal overlap introduce variance in the data. In order to reduce the dependence of the data on laser power variations, we normalized the charge by the square root of the laser energy as it was done for the delay scans since the field depends on the square root of the laser power.

The quarter waveplate scan shows that the interaction was maximized for one orientation of the quarter waveplate corresponding to circular polarization and was completely extinguished for the opposite handed circular polarization (90° rotation) in agreement with Equation 5.6. Near 65° quarter waveplate angle, the interaction is suppressed sufficiently that no charge is accelerated above 70 MeV, and at 90° no acceleration was observed. The fit shown in the figure is proportional to  $Q \propto \cos \theta - \cos 65^\circ$ .

We also replaced the quarter waveplate with a half waveplate and use it to rotate the linear polarization. Rotating the linear polarization by 90° did not affect the accelerated electron spectrum, showing that the helical motion of the electrons within the undulator had no preferred direction—that is, the motion was circular rather than elliptical.

### 5.3 High gradient acceleration

Once temporal overlap was achieved and the laser polarization was matched to the electron helix, we focused on increasing the laser energy in an effort to maximize the IFEL acceleration. The electron beam was focused to about 300  $\mu\text{m}$  with 800 pC (about 8 ps duration) initially to relax spatiotemporal alignment, and then reduced to 200  $\mu\text{m}$  with 100 pC (about 1 ps duration) of charge for more careful studies. Whereas the resonant energy of the undulator was designed to be 50 MeV, we chose to run initially at 52 MeV in order to ensure that the beam would be captured by the growing bucket.

Unfortunately whereas the [undulator was designed](#) for a 9.6 cm Rayleigh range, the physical beamline dimensions [restricted this to >25 cm](#) and the [focused laser was measured](#) to have an effective Rayleigh range closer to 30 cm. This discrepancy between design and experimental Rayleigh ranges caused a mismatch between the ponderomotive gradient driven by the laser and the gradient in the resonant energy set by the undulator tapering as [mentioned earlier](#). For a given laser power, the factor of 3 increase in the Rayleigh range implies a  $\sqrt{3}$  reduction in peak on-axis electric field near the undulator midpoint where the resonant energy tapering is steepest. This mismatch challenged our obtaining the full design acceleration performances in this experimental run by significantly increasing laser peak power requirements and motivated a [redesign of the undulator taper](#) for a [subsequent](#) run with improved capture.

Control of the longitudinal and transverse positioning of the laser focus allowed optimization during the experiment. The 3 inch diameter NaCl lens was translated along a rail in order to focus the laser to a waist at various positions along the undulator. The lens was positioned to place the laser waist 7 cm upstream of the undulator midpoint to maximize the accelerator performances as initially suggested by simulation-based optimization and then confirmed experimentally.

Transverse overlap was investigated by investigating how varying the laser transverse position at the entrance to the undulator affected the IFEL interaction. First a mirror was inserted just upstream of the copper mirror upstream of the final focusing lens to inject a HeNe laser onto the CO<sub>2</sub> beam path. The HeNe position was monitored on a beam position monitor (BPM) positioned about 10 inches upstream of the undulator, and a picomotor attached to the copper mirror provided fine control of the laser transverse position. We were not able to reproducibly position the HeNe upon each insertion due to instability in the mirror mount and actuator; so we repeatedly inserted the mirror until the HeNe was on the BPM and then recorded relative movements. Since each laser shot took a couple minutes and each laser position move took a few minutes, taking a few shots at one laser position required about 10 minutes, limiting the study to several positions. Figure 5.5 shows the results of the scan of the transverse laser position. The laser's measured transverse intensity profile at the undulator's entrance was fit to the maximum relative beam intensity estimator  $I \sim \Delta E_{\min}^4 / U_1$  for each position. For each of these shots, the beam charge was 100 pC and spot size was about 200  $\mu\text{m}$ . We chose the position with the best performance, and the fit suggests that this position was indeed near the beam axis.

Losses during transport reduced the laser power delivered to the undulator. Energy losses from reflections and apertures were estimated at the time of the experiment to be 27%; however, [comparing the energy measurements](#) in the laser room from the high gradient run with the laser energy in the experimental hall from the subsequent high capture run suggests that these losses may have been a factor of two larger. Images of the amplified pulse near the focus suggest that as much as 17% of the energy ended up in the tails of the transverse intensity profile due to higher order transverse modes. Furthermore, the laser has been observed to occasionally drift due to misalignment in the amplifier caused when shock waves move mirrors slightly during discharge. A study of the laser focus

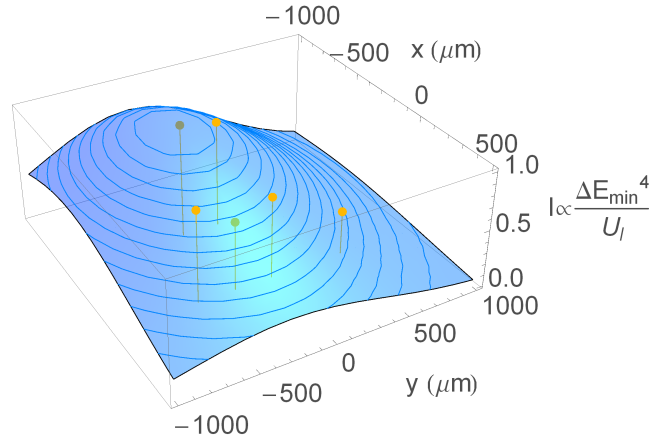


Figure 5.5: Transverse scan showing the maximum normalized laser intensity estimator for the laser at different transverse positions and a binormal fit with the measured laser waist at the undulator’s entrance.

positioning revealed that the interaction changed by as much as 20% when the laser was displaced by 500  $\mu\text{m}$  transversely. The maximum laser pulse energy measured upstream of transport was 8 J. Assuming 4.5 ps rms and a 1 mm spot size, the peak intensity used in the experiment exceeded 20  $\text{TW}/\text{cm}^2$ .

The maximum accelerated electron energy was measured for different shots with various estimated peak laser intensities from the measured laser energy as shown in Figure 5.6. The data are in rough agreement with simulations for the measured input parameters generated with the 3D IFEL code TREDI also shown in the figure. TREDI solves the Lorentz force equations rather than averaging the motion of the electrons over an undulator period [63] and was previously bench-marked against IFEL experimental results in planar undulators [24]. The simulations suggest that the laser intensity was just shy of that needed for full acceleration.

Raw images were acquired with a high resolution 12-bit camera with a dynamic range wide enough to capture the entire image without saturation. Background noise was subtracted, and energy was calibrated relative to a dipole current scan

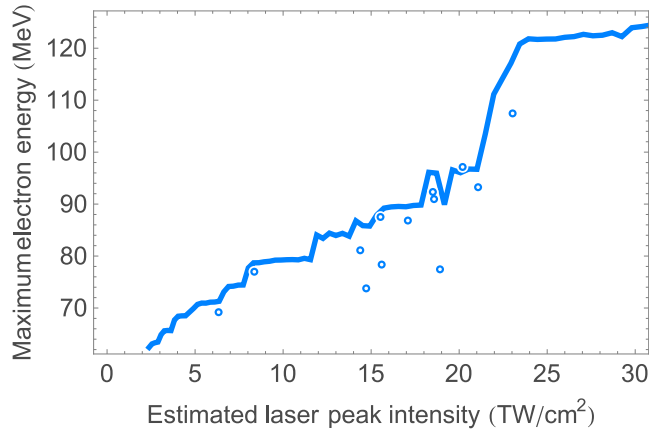


Figure 5.6: Maximum measured (dots) and simulated (line) output energy versus peak focal intensity.

with input beam of fixed energy. Spectra for the highest energy laser pulse is shown in Figure 5.7 along with spectra from a beam without laser and the results of simulation for the input parameters. The spectra shows that a small fraction of the beam was accelerated to energies as high as 106 MeV. Since the interaction region of the undulator is 54 cm long, this implies an average accelerating gradient of 100 MeV/m—a new record for average accelerating gradient at the time. This was one of the first few shots and had a charge of 800 pC, spot size of 300  $\mu\text{m}$ , and measured laser energy of 7.5 J.

In both measured and simulated spectra, part of the beam was decelerated by as much as 8 to 10 MeV as particles out of phase saw opposite electric field from resonant particles. Looking at the particle dynamics in longitudinal phase space, the decelerated fraction can be viewed as the part of the beam that falls out of the bottom of the bucket as the resonant energy is violently increased by the undulator tapering. Peaks in the spectra above 60 MeV appear in both the experimental and simulated spectra and can be explained as electrons dephasing at various positions in the undulator where laser intensity was insufficient to maintain a large enough ponderomotive bucket height for the local energy gradient.

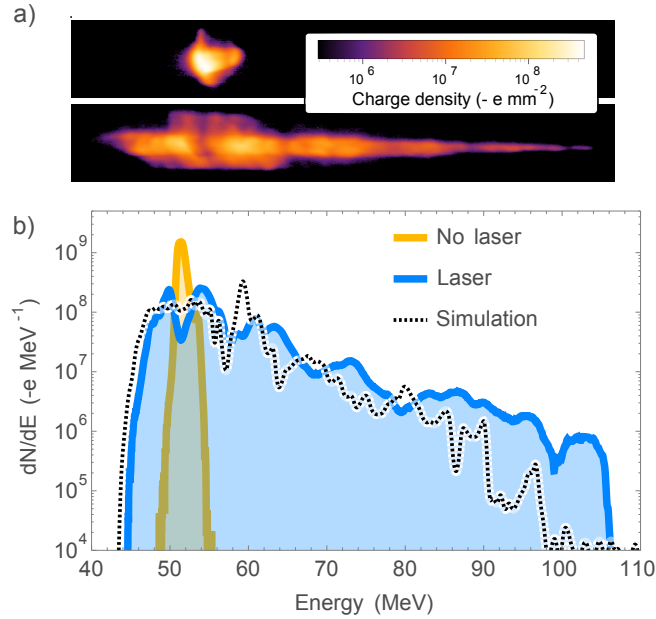


Figure 5.7: Raw spectrometer images (a) and calibrated spectrum with simulation (b) for a shot without laser and one with the highest energy.

Since the electron bunch and laser pulse lengths are comparable, time dependent effects can not be neglected and are included in the simulation. Similar electron and laser pulse lengths cause different slices of the electron beam to see different laser intensities and therefore detrap at different energies, smearing out the spectra. The dip at 52 MeV in the measured spectrum is due to a dark fiducial mark on the spectrometer screen caused by damage to the phosphor screen from an integrated exposure of  $>100$  nC/mm<sup>2</sup> to 52 MeV electrons from the input beam for shots without laser. Since the charge density of the accelerated beam was significantly less due to large dispersion and the unaccelerated beam illuminated the same position for the majority of shots, the rest of the screen remained undamaged.

We also attempted a study of the effect of the input electron beam energy on the IFEL performance, the results of which are displayed in Figure 5.8. The initial electron energy was varied by changing the linac phase slightly and then

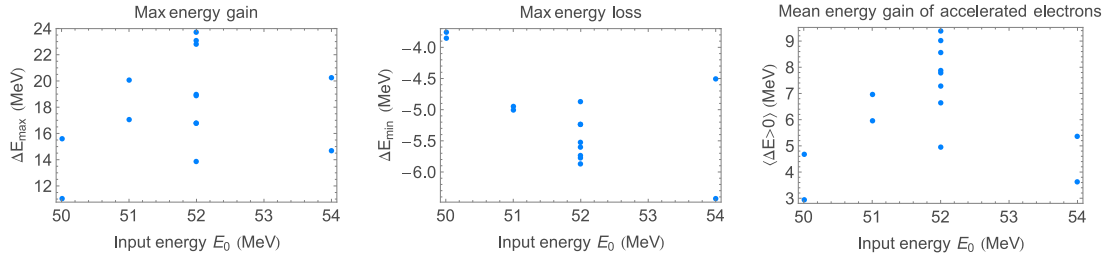


Figure 5.8: IFEL performance versus input electron energy.

scaling the magnetic focusing fields to account for the energy change. Because the beam’s velocity and trajectory changed slightly, each energy change necessitated a few shots to resynchronize on a picosecond time scale. The results of this study show that the energy acceptance of the accelerator is at least 8% or 4 MeV.

This high gradient run achieved unprecedented energy gains of up to 54 MeV. The average energy gradient over the 54 cm long undulator is larger than 100 MeV/m and competitive with state-of-the-art conventional RF-based accelerators suggesting the IFEL as a promising candidate for a medium-to-high energy range compact accelerator. Despite these successes, the accelerator failed to achieve the designed output energy due to a mismatch between the design and experimental laser focusing, and the highest energy shot was neither reproducible nor of a useful amount of charge. In fact, all of the accelerated beams during the high gradient run had huge energy spread and were very unstable, motivating a redesign of the undulator and a subsequent run to improve the quality and reliability of the accelerated beams.

## 5.4 High capture acceleration

In order to improve the quality of the IFEL output beam, we [redesigned](#) the undulator tapering to account for the measured focused laser intensity and focal properties. To ensure that the majority of shots would be accelerated to full

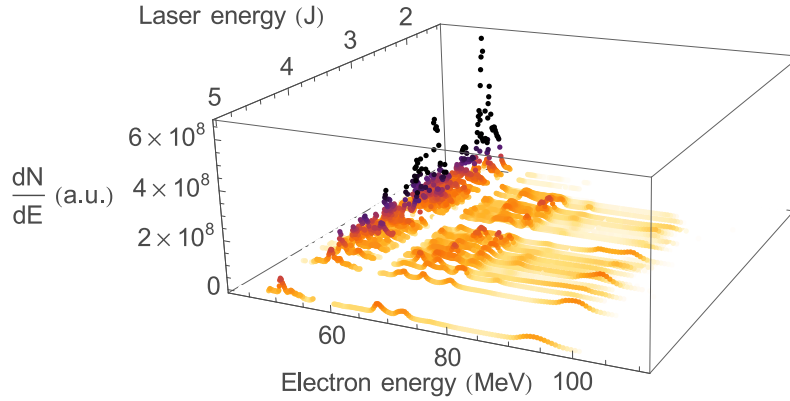


Figure 5.9: Plot showing the spectra of all IFEL shots for one day during the high capture run.

energy, we designed the threshold intensity to be  $5 \text{ TW/cm}^2$  which was about a fifth of the high gradient configuration's  $25 \text{ TW/cm}^2$  full acceleration threshold intensity and well within the sample of estimated intensities from the previous run. As a result for this “high capture” undulator tapering configuration, we obtained much improved beam spectra with slightly lower final energy. For this run, we ran with an electron beam size of about  $170 \text{ }\mu\text{m}$  rms and charge of  $100 \text{ pC}$  corresponding roughly a  $1 \text{ ps}$  duration at  $100 \text{ A}$ .

A summary plot of all shots for one day is shown in Figure 5.9. All shots with measured laser energy greater than  $1.95 \text{ J}$  show acceleration to the design energy of  $93 \text{ MeV}$  whereas the few shots with laser energy less than  $1.95 \text{ J}$  showed maximum electron energies monotonically increasing with laser energy, yet falling short of the design energy. The energy of the accelerated beams was remarkably stable. Of the 46 shots with laser power above the capture threshold ( $>180 \text{ GW}$ ), 37 had reasonable timing and charge. The energy distribution of the peak charge density for these shots is shown in Figure 5.10. The energies of the peak charge density of the accelerated beams were normally distributed and with a fit mean of  $93.7 \text{ MeV}$  and rms width of  $1.2 \text{ MeV}$  ( $<1.3\%$  relative jitter) which is remarkable considering that laser power variation for these shots was  $27\%$  rms. The raw data

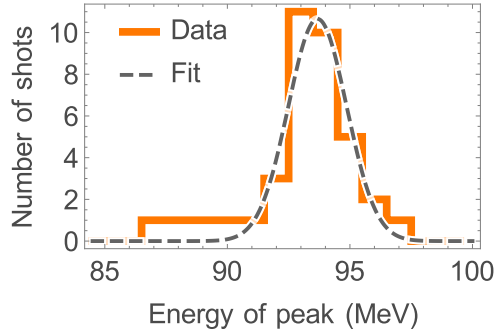


Figure 5.10: Histogram of the energy of the peak charge density of the accelerated beam.

has a median energy of 93.5 MeV with a standard deviation of 2.0 MeV (2.1%) with the difference in these rms widths due to the low energy tail consisting of a few shots with low charge, and increasing the charge cut slightly removes these shots so beams with greater charge are better described by the Gaussian fit. On the other hand, applying a

In this second undulator tuning configuration, final energy fluctuations are negligible, reflecting an important advantage of IFEL over other laser-based acceleration schemes in terms of output stability. If the laser provides a sufficient ponderomotive gradient, the IFEL output energy is only set by the tapering of the undulator resonant condition with laser fluctuations at first order only affecting the accelerator capture efficiency. This demonstration also shows that the IFEL output energy could be tuned by controlling the undulator magnetic field. For example, in next generation IFELs, computer control of the magnet gaps or additional small electromagnets throughout the undulator could be used to tune the output energy of the accelerator on demand.

Three shots are displayed in Figure 5.11. Up to 30% of the injected beam is accelerated to 93 MeV final energy. A clear monoenergetic bunch of electrons is present with a final output rms energy spread of 1.8%. The fraction of charge accelerated is large considering that the injected electron bunch was uniformly

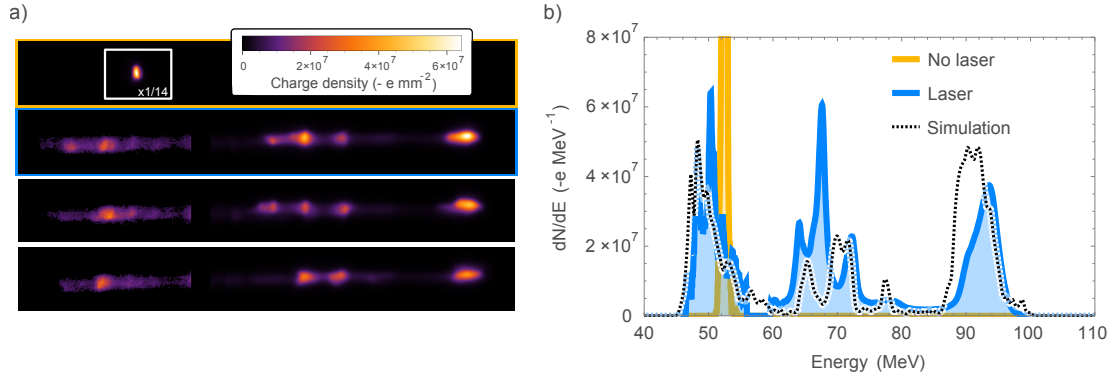


Figure 5.11: Raw electron spectrometer images for various shots (a) and calibrated electron spectra for the first two shots (b) for the high capture IFEL configuration.

distributed over many laser periods, and simulations with a prebuncher designed for a subsequent run show that the fraction captured may be increased to as much as 80% of the injected charge [75]. Furthermore this low energy spread result compares very favorably with the best laser wakefield acceleration demonstrations and could be reduced in future IFELs by better matching the input electron beam's phase space to the accelerator as discussed in Chapter 3.

The data is compared with three-dimensional particle tracking simulations in the combined laser and undulator fields using all the measured input parameters and field maps (i.e. no free parameters). The simulation code [66] solves the Lorentz force equations rather than averaging the motion of the electrons over an undulator period and compares well with the bench-marked IFEL codes TREDI [63] and Genesis [48]. A larger than expected amount of charge is lost around the intermediate energies 65 to 75 MeV corresponding to just upstream of undulator's midpoint where the accelerating gradients are largest. In this region, the laser waist begins to narrow slightly, and the tails of the electron beam are bathed in lower laser intensity. As this happens, the effective resonant phase increases, shrinking the ponderomotive bucket, and causing particles near the bucket's separatrix to detrap. On the other hand, the large laser waist allowed much more of

the electrons to make it through this highest gradient region than the previous, high gradient experiment, showing that a large waist compared to the electron beam is important for high efficiency IFEL acceleration.

## 5.5 Emittance measurement

The electron beams produced during the high capture experimental run were shown to have relatively low energy spread growth in line with that expected by simulation. Initial simulations also suggested that the normalized transverse emittance of the accelerated electron beam should be conserved. In order to investigate the acceleration's effect on the transverse emittance, we used the quadrupole located after the undulator a measurement of the vertical emittance of the laser-accelerated beam. Due to the rotational symmetry of the helical IFEL interaction and as supported by the simulation, it is reasonable to assume that the value obtained also applies to the horizontal plane.

We first measured the emittance just downstream of the linac using a section of beamline with a 6 m drift separating two quadrupole triplets. Figure 5.12 shows two sets of electron beam size measurements for each of the 6 beam position monitors (BPMs). The first and last two pairs of BPMs each straddle a quadrupole triplet while the BPMs located near the middle of the plot are in the middle of the drift. The emittance and twiss parameters were calculated by simultaneously fitting all permutations of these beam position measurements using the beamline geometry and magnetic elements with currents read out at the time of the measurement. The fit normalized emittances were  $1.3 \mu\text{m}$  for the horizontal plane and  $1.5 \mu\text{m}$  for the vertical. The lines in the figure represent the beam size evolution for each transverse plane calculated by propagating the fit twiss parameters through matrices for each of the beamline elements and scaling by the fit emittance.

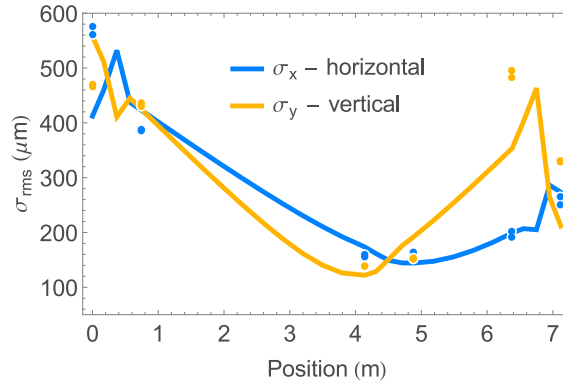


Figure 5.12: Fits to electron beam rms widths for a section of beamline with a 6 m drift between two quadrupole triplets.

As a next step to measuring the emittance of the beam, we varied the current in the quadrupole between the undulator and spectrometer while imaging the spot size on the spectrometer. Figure 5.13a shows the results of the best fits to quadrupole scans[76] for the unaccelerated and accelerated electron beams. The normalized vertical emittance of the unaccelerated beam was measured to be 1.3 mm-mrad in good agreement with the measurements taken upstream of the experimental setup. For accelerated electrons between 92 and 94 MeV taken during the high capture experimental run, the best fit for normalized vertical emittance yields an estimate of 3 mm-mrad. This is in relatively good agreement with the value of 3.3 mm-mrad from the simulations as shown dashed in the figure.

The observed emittance growth is affected by fluctuations in spatial overlap between the electrons, laser and undulator. Space constraints on the beamline limited the electron focusing optics just upstream of the undulator to a doublet instead of a triplet, reducing our ability to reduce the betatron function of the electron beam to match the natural focusing of the undulator. The unmatched beam causes betatron oscillations within the undulator which cause emittance growth oscillations within the helical undulator to not average out to zero. Simulations shown on the right side of the figure show that the growth could be eliminated

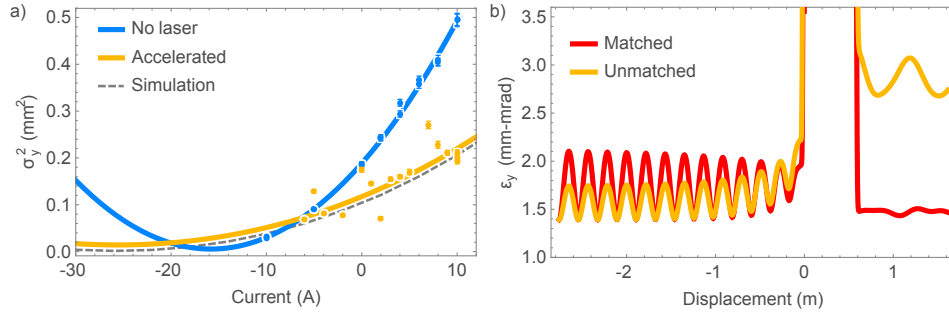


Figure 5.13: Quadrupole scans showing measured emittance (a) and simulated emittance evolution for a matched and unmatched beam (b).

by reducing the e-beam rms spot size to 80  $\mu\text{m}$  and limiting the relative pointing jitter to  $<100 \mu\text{m}$ . Indeed, a more recent iteration of the experiment with a more closely matched betatron function has been shown to preserve the transverse normalized emittance of the accelerated beam. For future IFEL accelerators, it is therefore important to properly match the beam into the undulator's natural focusing channel in order to preserve the accelerated beam's normalized transverse emittance.

## CHAPTER 6

# Tapering enhanced stimulated superradiant amplification

Up to here, this dissertation has investigated the challenge of accelerating electrons by transferring energy from the laser to the electron beam in a strongly tapered undulator. The lack of nearby boundaries or a medium (gas, plasma) to couple the light to the electrons implies very little irreversible losses and in principle enables very high energy transfer efficiencies. [Simulations show](#) that an IFEL could be optimized to transfer nearly 80% of optical power to a relativistic electron beam [\[17\]](#). Reversing this process by taking the e-beam and laser output from a heavily loaded IFEL and putting it back into the accelerator backwards, a majority of the energy stored in the electron beam may be converted to coherent radiation.

Based on this idea, we investigate in this chapter a novel scheme for efficient generation of radiation whereby a high intensity seed laser pulse and a relativistic electron beam copropagate in a tapered undulator, and the IFEL interaction is used to decelerate the beam. The scheme relies on the coherent emission of a prebunched beam going through an undulator in the presence of an intense driving field (i.e. stimulated superradiance emission [\[77\]](#)). Very strong tapering of the undulator is the other key ingredient to enable high conversion efficiencies and support large deceleration gradients and electron energy losses.

For perspective, saturation effects limit FEL conversion efficiency to levels comparable to the Pierce parameter  $\rho$  which is typically  $< 0.1\%$  [\[9\]](#). FEL undulator tapering [\[28\]](#) has been shown to allow much larger efficiencies. At very

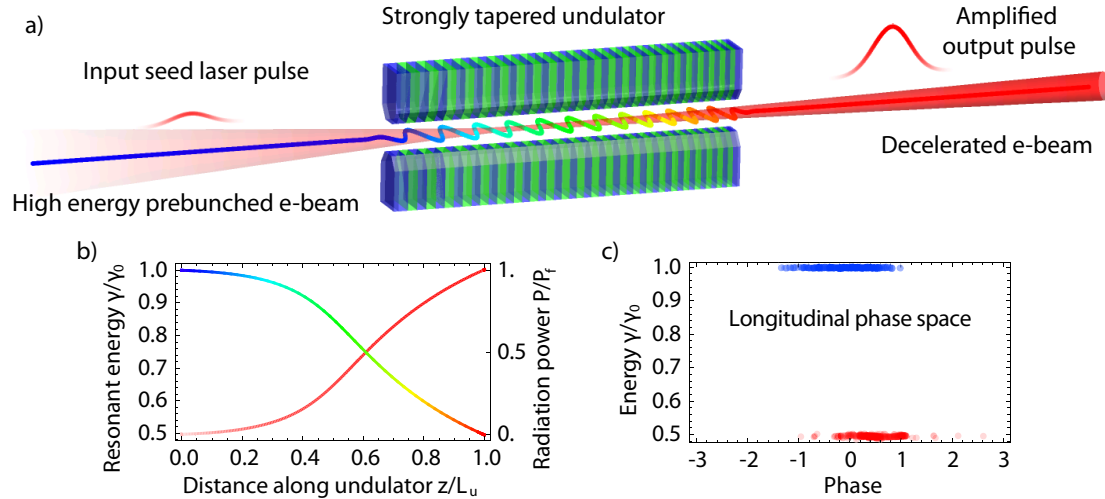


Figure 6.1: An implementation of TESSA. The diagram in a) shows a seed laser focused into the strongly tapered undulator along with a prebunched electron beam. As the e-beam energy—blue represents high energy while red is low—decreases along the undulator, the laser power grows. Plots of b) the normalized electron energy and laser power along the undulator and c) initial and final longitudinal phase spaces are shown.

long wavelengths (35 GHz) where it is possible to use a waveguide to maintain an intense radiation field on axis, up to 35% conversion efficiency has been demonstrated [78]. At shorter wavelengths [79, 80], the reduction of gain guiding and the onset of spectral sidebands have limited the effectiveness of tapering [81]. For example at the LCLS, the power extraction has remained well below the percent level limiting the amount of energy in the pulse to a few mJ. Higher conversion efficiencies could lead to unprecedented intensity x-ray pulses with over  $10^{13}$  photons per pulse providing sufficient signal-to-noise to enable the long sought goal of single molecule imaging [11]. In the visible and UV spectral ranges, large electrical to optical conversion efficiencies are also very attractive for the development of high average power (10-100 kW-class) lasers especially when considering that superconducting radio-frequency linacs can create relativistic electron beams with very high wall-plug efficiencies and MW average power.

Tapering-enhanced stimulated superradiant amplification (TESSA) can be viewed as essentially an IFEL accelerator run backwards as a decelerator (see Figure 6.1). The drive laser field stimulating the electron emission can be obtained from an external seed laser or, in a spectral region where external sources are not available, from redirecting FEL radiation into a TESSA afterburner undulator [82]. In this case, the FEL radiation can be refocused to reach peak intensities significantly larger than the FEL saturation level, thereby greatly increasing the initial decelerating gradient. In principle, it is also possible to obtain the seed pulse from the build-up in an oscillator cavity [83]. The required beam prebunching may be obtained by using the seed laser and a constant parameter undulator possibly in combination with one or more chicanes to apply  $R_{56}$  for larger bunching factors and reduced energy spread [33].

In the analysis of TESSA which follows, we identify i) a low gain regime where the radiation does not vary in power significantly along the undulator so we can assume a constant and known radiation field and ii) a high gain regime where significant amplification occurs.

## 6.1 Low gain regime

In the low gain regime, the energy stored in the radiation field does not significantly change along the undulator. By introducing an undulator builder equation such as Equation 2.44 relating the undulator strength  $K$  to its period  $\lambda_u$  and specifying  $K_l$  for the laser, a low gain tapering equation for the period may be produced. Such low gain tapers determined by Equation 2.43 for a Gaussian laser have produced undulator taperings successfully verified with IFEL acceleration experiments [24, 52].

In order to reach a better understanding of the TESSA dynamics, we start by analyzing the low-gain regime where the radiation power does not significantly

change along the undulator. Defining the efficiency as the relative change in energy for the beam  $\eta_{net} = \gamma_f/\gamma_0 - 1$  and assuming  $|\eta_{net}| \ll 1$  for the constant period tapering case, we obtain an estimate of  $\eta_{net} \approx -2\pi N_w K_l \sin \psi_r$ . In practice to reach tens of percent efficiency, the number of periods in the undulator  $N_w$  should be on the order of  $K_l^{-1}$ . This regime can be useful in an oscillator configuration (an analysis without undulator tapering is presented in [83]) where a small fraction of the output power is split and redirected at the input and the low gain is compensating the losses per pass. Note that if the injected electron beam is not prebunched, the first section of the interaction can be designed with  $\psi_r \approx 0$  until full bunching occurs and the deceleration can start. Since the efficiency in the low-gain regime is independent of beam parameters, the output radiation power scales linearly with the input e-beam current. Considering diffraction, for a nearly constant undulator  $K$ , efficiency is maximized when a TEM<sub>00</sub> Gaussian seed laser is focused with a Rayleigh range of  $z_r \approx 0.15L_w$  to a waist at the undulator midpoint [17].

## 6.2 Low gain TESSA experiment at ATF

The experimental results presented in this dissertation [demonstrated energy doubling](#) of a 52 MeV beam with  $\sim 100$  MeV/m average accelerating gradients and [capture of up to 30%](#) of an unbunched electron beam [52] using a strongly tapered undulator in a helical geometry IFEL interaction. Reversing the process to decelerate a prebunched beam by the same mechanism, one could imagine the possibility of extracting half of the e-beam power and converting it into coherent radiation. For comparison, FELs are typically limited by the Pierce parameter  $\rho$  to less than 1 percent electro-optical power conversion and even the best lasers don't exceed efficiencies of about 30% so converting nearly half of the e-beam power to coherent radiation would be significant achievement. Since the maxi-

imum electron beam peak power of 65 GW (1 kA at 65 MeV) at ATF is below the  $\sim 100$  GW CO<sub>2</sub> laser power needed for 50% deceleration, the gained optical power does not significantly affect the interaction, and the decelerator operates in the low gain TESSA regime.

### 6.2.1 Experimental design

The IFEL decelerator project builds off of the experience of the helical IFEL experiment by retuning the [existing helical undulator](#) to decelerate electrons instead of accelerating them. The experimental setup is depicted in Figure 6.2. The e-beam and laser both enter from the left side of the figure, and the dipole ID1 cancels dispersion as it kicks the electrons onto the beamline with the laser pulse. IQ1, IQ2, and IQ3 are focusing quadrupoles while IPOP1, IPOP2, and IPOP3 house beamline diagnostics. A prebuncher & phase delay stage located just upstream of the undulator prebunch and phase-lock the e-beam to the ponderomotive wave. Downstream of the undulator lies an energy spectrometer for the decelerated beam as well as a CO<sub>2</sub> laser pickout for laser diagnostics (joulemeter, spectrometer, and streak camera).

In order to further increase the strength of the stimulated radiation, compression and prebunching are necessary. The peak current of the beam will be increased from 100 A to 1 kA with ATF's compressor. Furthermore, a combination prebuncher and chicane phase delay module is currently being built at UCLA with the goal of increasing the fraction of the beam accelerated to full energy. The electron beam acquires an energy modulation at the resonant wavelength while the chicane module delays the modulated beam in order to phase lock to the ponderomotive wave at the entrance of the helical IFEL undulator. 3D simulations show that up to 70 to 90% of the injected beam should be fully decelerated. With a 30 MeV change in energy, 1 kA current, and 80% capture, an estimated 24 GW e-beam power should be transferred to the radiation field.

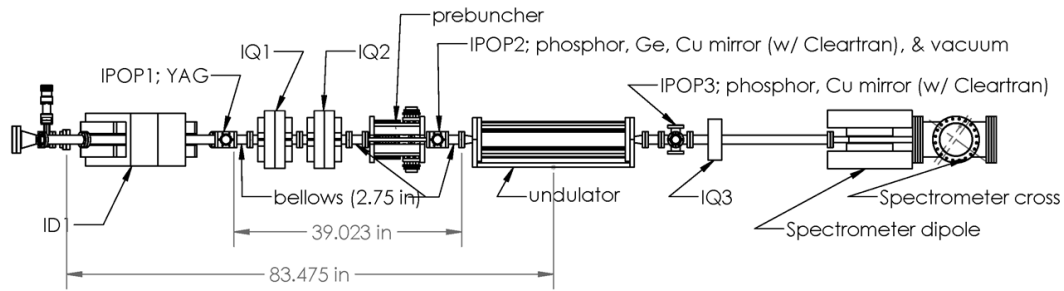


Figure 6.2: Diagram of the beamline setup for the IFEL decelerator project at ATF.

### 6.2.1.1 Helical undulator design

The tapering of the helical undulator was previously modified for the [high capture](#) IFEL configuration, enabling the first demonstration of IFEL resonant energy tuning. Since the undulator period is predetermined by the dimensions of the magnets in the undulator, the gap between magnets was changed in order to manipulate the field and resonant energy along the undulator. In order to reverse the effect of the accelerator, the undulator may be reversed and the gap tapered in order to reduce the resonant energy during the interaction. In this case, a positive resonant phase  $\psi_r$  yields a tapering with decreasing resonant energy along the undulator. The highest stable energy electron beam that may be produced at the ATF is 70 MeV, and the final energy of the decelerated electron beam is 42 MeV. The experimental parameters are summarized in [Table 6.1](#).

When the undulator period and laser parameters are specified along with the initial condition that  $K$  at the entrance be such that the resonant energy is equal to the input beam's 70 MeV energy, the tapering equations yields  $K$  which in turn determines the on-axis field strength along the undulator. The undulator builder equation can then be used to estimate the gap along the undulator needed to create the designed on-axis field which can then be [modeled with Radia](#).

The laser and e-beam parameters used in the tapering design are specified in

Table 6.1, and the calculated period and resonant energy as well as the solutions to the IFEL/FEL equations are shown in Figure 6.3. The initial seed power was chosen to be large enough for significant deceleration but small enough to increase the ratio between the signal (stimulated power) to background (seed power). The resonant phase was set to a constant  $\pi/4$  as a compromise between bucket depth and ponderomotive gradient.

<b>Parameter</b>	
E-beam energy	70 to 40 MeV
Laser focal intensity	4 TW/cm <sup>2</sup>
Laser wavelength	10.3 $\mu$ m
Rayleigh range	30 cm
Laser waist	undulator midpoint
1/e <sup>2</sup> spot size	0.99 mm
M <sup>2</sup>	1.07
Resonant phase	$\pi/4$

Table 6.1: IFEL decelerator design parameters

### 6.2.1.2 Time resolved laser diagnostics

The setup of the beamline for the IFEL decelerator experiment is very similar to that of the IFEL accelerator experiment with the exception of the laser diagnostics. While the peak power of the radiation is increased nearly 30% during the interaction, since the laser pulse duration of 4.5 ps is longer than the 1 ps e-beam duration, the total energy of the radiation field should only increase by a few percent, necessitating temporally resolved power measurements of the amplified pulse. In order to resolve the power gain, the amplified CO<sub>2</sub> laser pulse will be extracted from the beamline about 4 m from the undulator where intensities are below damage thresholds for transport optics and sent to a streak camera for time

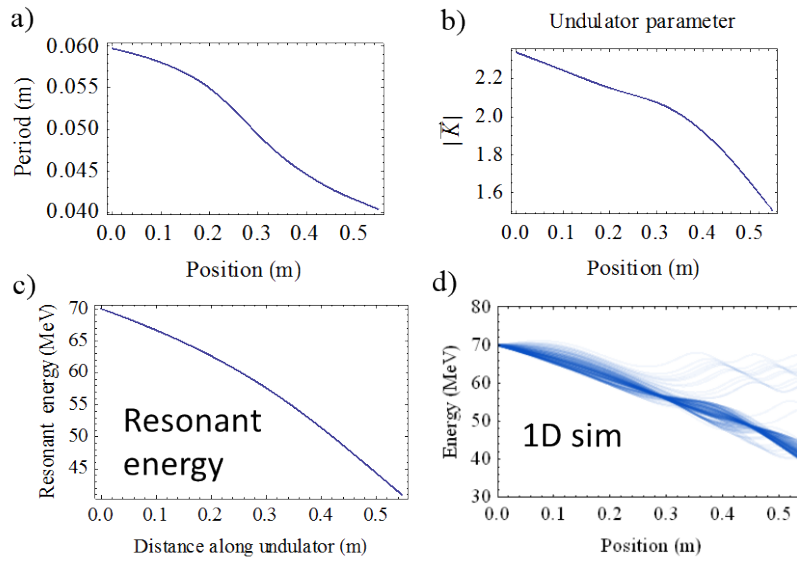


Figure 6.3: The a) period and b) normalized undulator vector potential decreases along the undulator causing c) the resonant energy to decrease. d) Solutions to the equations of motion describing the longitudinal IFEL dynamics were calculated with the design seed laser and undulator tapering.

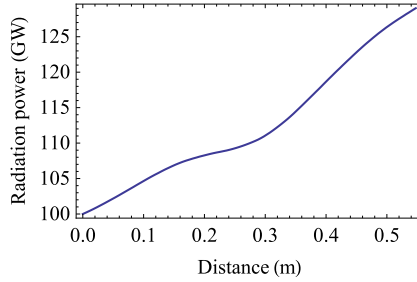


Figure 6.4: The radiation power grows along the undulator as the electrons are decelerated.

domain measurements and a diffraction grating for spectral measurements. Furthermore in order to understand better the laser evolution, small reflections from the laser will be split off up- and down-stream of the undulator and calibrated to yield relative energy measurements.

### 6.2.2 Simulations

Simulations were performed with the 3D FEL code Genesis 1.3 [48] for a 70 MeV input e-beam, laser focusing parameters listed in Table 6.1 and 100 GW seed laser power. The radiation power grows along the interaction as shown in Figure 6.4. Figure 6.5 shows the output beam’s longitudinal phase space at the end of the undulator. Up to 43% of the beam is captured and decelerated from 70 to 42 MeV while the radiation power grows by nearly 30%. The transverse profile of the laser spot is also shown in Figure 6.6.

### 6.2.3 Experimental outlook

While recent achievements in IFEL acceleration have focused on high-gradient acceleration, the UCLA-BNL helical IFEL decelerator experiment aims to achieve high-gradient deceleration in order to demonstrate high efficiency electro-optical conversion. The undulator tapering design achieves this by matching the reso-

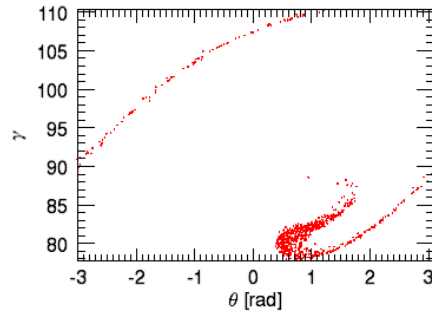


Figure 6.5: The e-beam longitudinal phase space is shown at the exit of the undulator. The beam loses 28 MeV as the particles are decelerated from 70 to 42 MeV.

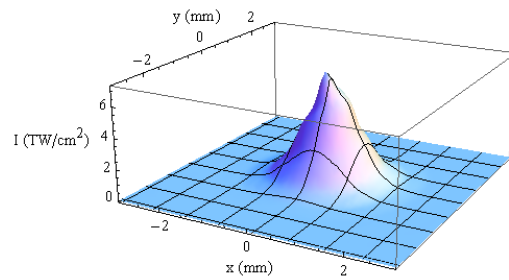


Figure 6.6: The transverse radiation profile is shown at the exit of the undulator. Growth of the radiation at the center of the seed is clearly visible.

nant energy and ponderomotive accelerating gradients for decelerating resonant phases with the strongly tapered helical IFEL undulator. By compressing and prebunching the electron beam, significant power gain should be observable with time resolved laser measurements. For moderate laser intensities, over 40% of the e-beam energy is predicted to be converted to coherent radiation. Such gains are impressive for a single pass amplifier, and when stacked in a laser recirculation scheme, may pave the way to yet greater laser amplification in future experiments.

### 6.3 High gain regime

Whenever the stimulated superradiant emission becomes the dominant contribution to the total laser field driving the interaction, the undulator can be tapered more aggressively in order to take advantage of the additional ponderomotive drive. In this case, the tapering which maximizes conversion efficiency depends on the injected e-beam current since a higher current generates more radiation per unit length which allows larger decelerating gradients and higher electro-optical energy transfer rates. Thus, whereas the output radiation power scales linearly with injected current in the TESSA low gain regime, the output power in the high gain regime grows faster than linearly with respect to input e-beam current.

The main difference in calculating the tapering is that now  $K_l$  is the total electromagnetic field due to the seed plus the stimulated radiation, which is a dynamic variable evolving throughout the interaction and depending on the entire history of the e-beam spot size, current profile, and change in resonant energy throughout the interaction. The result is a complicated delay differential equation for  $K_l$  where three-dimensional effects play an important role. In this case, it is easier to optimize the undulator tapering by solving for the actual field evolution with the help of 3D simulations.

In practice, the well-benchmarked 3D FEL simulation code Genesis [48] is

used to solve for the intensity of the radiation sampled by the electrons after a small number of undulator periods without tapering. This value is then fed into the tapering equation to calculate the optimum change of parameters for the following undulator section. These parameters along with the recorded particle and radiation distributions from the previous simulation are read by Genesis for the next step of the calculation which evolves the system for another small section of undulator. The optimization algorithm is then repeated until the end of the undulator. The result is an optimum undulator tapering and a self-consistent 3D simulation of the evolution of the electron beam and radiation in the optimized tapered undulator.

This tapering generation algorithm, dubbed Genesis-informed tapering scheme, or GITS, can be used both in the constant and the varying period cases. For the former, Equation 2.42 is used to calculate the undulator  $K$  parameter variation while the period is held constant to the initially assigned value. For the variable period undulator, Equation 2.43 is used where  $K$  is related to the period by the undulator builder equation.

It is of critical importance to choose the variation of the undulator parameters in order to maintain the majority of the particles trapped in the ponderomotive bucket. In particular due to 3D effects, not all particles experience the same laser intensity or  $K_l$ . In order to account for this problem, GITS looks up the local intensity seen by each macro-particle in the simulation and softens the tapering to keep any desired fraction of the beam trapped within the resonant bucket.

A particle maintains resonance if it is trapped near a local minimum of the ponderomotive potential. For particles with small relative energy deviations from resonance  $\eta = \gamma/\gamma_r - 1$ , the Hamiltonian can be approximately written as

$$H = ck_w \left( \eta^2 - \frac{2K_l K}{1 + K^2} (\cos \psi + \cos \psi_r + (\psi + \psi_r - \pi \operatorname{sgn} \psi_r) \sin \psi_r) \right) \quad (6.1)$$

Particles in regions of phase space with  $H < 0$  are trapped within the bucket, while particles outside of the bucket where  $H > 0$  are free. It is important to note that the size and location of the bucket changes with the field sampled by each particle. Equation 6.1 is first evaluated for each particle with  $\psi_r = 0$  to select particles with  $H < 0$ . We then determine the minimum  $K_l$  for this fraction of particles and use it with the tapering equations to determine the tapering of the undulator parameters.

With this method, it is helpful to start with a prebunched beam so that the tapering is allowed to change rapidly. Prebunching via the method of energy modulation with an undulator followed by  $R_{56}$  via a chicane or drift is greatly desirable here as it results in highly bunched beams with reduced energy spread, which increases ease of trapping by concentrating the injected e-beam in phase space. The use of a chicane also enables the e-beam bunches to be phase shifted to the center of the accelerating bucket. Furthermore, refocusing the driving radiation increases the bucket height, further decreasing the Hamiltonian and therefore increasing ease of trapping.

The advantages of prebunching and focusing the radiation before deceleration with TESSA help explain the differences with respect to standard FEL tapering. The FEL mechanism fills the ponderomotive bucket at zero resonant phase so that only a relatively small core region of phase space may be matched into an accelerating bucket. Conversely, the TESSA approach tailors the input phase space to match well a strongly decelerating bucket from the beginning, allowing strong deceleration without sacrificing a significant fraction of the injected beam, and then optimizes the deceleration by matching the tapering and ponderomotive gradients while selecting the resonant phase in order to maximize trapping.

## 6.4 High power EUV light source

In the rest of this chapter we examine the results of GITS for a couple of relevant cases where high extraction efficiency can enable break-through applications for electron beam-based light sources. In the first example we consider a 1 GeV linac-driven radiation source for EUV lithography, which requires achieving high average power at 13.5 nm. In a conventional SASE FEL optimized for this wavelength range, a practically achievable Pierce parameter is on the order of  $\sim 0.002$ , thus a state-of-the-art superconducting RF light source such as XFEL can achieve about 100 W average power output with  $\sim 50\mu\text{A}$  average current. Applying a conventional adiabatic tapering technique to maximize the output power with a 5 GW seed and 23 m long undulator with parabolically tapered K could possibly increase the efficiency to 18% as shown in Figure 6.7a, yielding 8 kW average power which is still insufficient to meet industry needs of roughly 20 kW average power.

On the other hand, using a refocused EUV seed to drive a TESSA amplifier, it is possible to convert nearly half of the electron beam power into the 13.5 nm light, all within a 23 m long undulator. The solid lines in Figure 2 show the radiation power increase from the starting seed peak power of 5 GW from an upstream FEL to a final  $>1.8$  TW as the electron beam with a modest initial bunching factor of 0.58 is decelerated in the process from 1 GeV to 320 MeV for a variable period undulator. Note that this remarkable numerical result still corresponds to a relatively modest decelerating gradient value of about 30 MeV/m, something that has already been demonstrated experimentally in the inverse (IFEL) configuration.

While the undulator builder equation describes the relationship between period and field amplitude for fixed gap, it is also possible to change the field by increasing the gap while holding the period constant. The results of simulations for a fixed period undulator optimization (dashed curves in Figure 6.7) show a

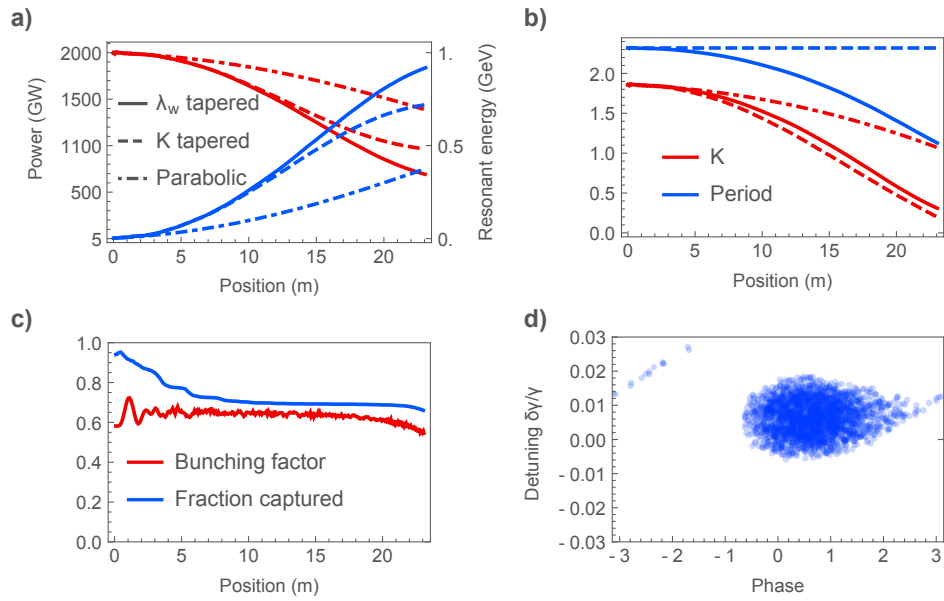


Figure 6.7: The results of GITS optimizations for a 1 GeV, 4 kA e-beam with a moderate initial bunching factor of 0.58 lasing at 13.5 nm with a seed power of 5 GW from an upstream FEL are shown in the above plots for the case of varying period (solid lines) and constant period (dashed). Also shown are the results of simulations for an undulator with parabolic tapering (dot-dashed lines).

reduced output peak power of 1.35 TW, demonstrating that varying the period of the undulator improves the conversion efficiency.

Applying these results to the same example of a 50  $\mu\text{A}$  average current XFEL-like driver beam (1 GeV electron energy, 20 kHz rep rate, 4 kA peak current, and 500 fs rms bunch length) with the TESSA afterburner, one can achieve  $>20$  kW average power output at 13.5 nm—well within the application target range.

<b>Parameter</b>	<b>EUUV</b>	<b>X-ray</b>
E-beam energy	1 $\rightarrow$ 0.32 GeV	14.35 $\rightarrow$ 10.7 GeV
Rms energy spread	0.002	0.0001
E-beam current	4 kA	4 kA
E-beam emittance	2.0 mm-mrad,	0.3 mm-mrad
E-beam spot size	45 $\mu\text{m}$	10.5 $\mu\text{m}$
Initial bunching	0.58	shot noise
Laser peak power	5 GW $\rightarrow$ 1.8 TW	5 MW $\rightarrow$ 9.6 TW
Laser wavelength	13.5 nm	3.0 $\text{\AA}$
Seed Rayleigh range	1 m	3 m
Seed waist	3 m	4 m
Undulator period	2.32 $\rightarrow$ 1.00 cm	3.34 $\rightarrow$ 2.90 cm
Undulator K	1.86 $\rightarrow$ 0.19	3.63 $\rightarrow$ 2.85
Undulator length	23 m	120 m
Resonant phase	0 $\rightarrow$ 1.14	0 $\rightarrow$ 0.66

Table 6.2: EUUV and x-ray GITS simulation parameters

## 6.5 X-ray FEL afterburner

As another example, we consider the application of TESSA tapering to the generation of hard x-rays. The challenge here is to maximize the energy per pulse in

order to enable single molecule imaging. More than  $10^{13}$  photons in a  $<10$  fs pulse are required in order to beat the damage and obtain the diffraction information before destroying single molecules [84]. For 4 keV photons (3 Å wavelength), the peak power corresponding to this pulse approaches 1 TW.

We start our simulations with an unbunched electron beam and 5 MW of seeded FEL radiation power, which is typical after self-seeding [85]. An important effect is uncovered by the time-dependent simulations. When trapped in the ponderomotive potential, the electrons undergo synchrotron oscillations in longitudinal phase space with period  $z_s = \lambda_w \sqrt{(1 + K^2)/4KK_l \cos \psi_r}$  and sideband frequencies are generated as discussed in [79]. In the time-domain, these correspond to oscillations in the time-profile of the field amplitude. This effect is clear in the simulation results shown in Figure 6.8 where we follow a 5 fs slice of the beam along the undulator. The ripple in the temporal power profile shown in Figure 6.8b appears in the spectrum in Figure 6.8c as sidebands around the central resonant frequency. As the amplitude of this oscillation grows, particles in those slices experiencing lower laser intensities detrap from the ponderomotive bucket and efficient energy exchange stops. While time independent simulations yield 13 TW of power, the sideband instability limits the average power of time dependent simulations to less than 6 TW as shown in Figure 6.8a.

Shown along the undulator in a) are the mean powers for simulations with identical initial conditions but different frequencies of chicane delays used to suppress the sideband generation. b) and c) show the output temporal profiles and spectra for a standard time dependent simulation and a sideband suppressed simulation with delays every 13 m. The undulator parameters and bunching factor for the case with delays per 13 m are depicted in d) and output longitudinal phase space is depicted in e).

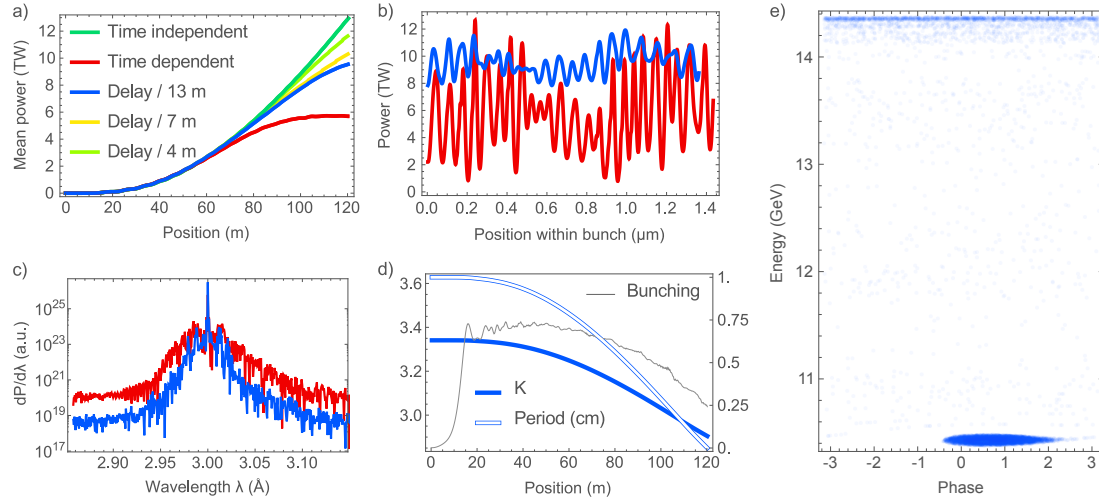


Figure 6.8: GITS simulations for the case of an x-ray FEL afterburner with a 14.35 GeV, 4 kA unbunched electron beam and 5 MW seed laser with 3 Å wavelength.

### 6.5.1 Sideband suppression

This synchrotron sideband instability is somewhat mitigated by strong tapering which causes the synchrotron frequency to quickly vary along the interaction [81]. In order to suppress further the sideband instability, we introduce delay modules periodically throughout the undulator. The function of these delays [86] is to introduce 180 degree phase shifts for the sideband oscillations while preserving the phase of the fundamental resonant frequency. The required delays are on the order of  $z_s(1 + K^2)/4\gamma^2$  or 30-100 nm for our case and can be introduced using magnetic chicanes. Isochronous chicanes are preferred for this application since due to the large energy spread of the electron beam during the deceleration, bunching and trapped fraction are degraded by the introduction of a large chicane dispersion. The number of the chicanes required to suppress the formation of the sidebands is set by the instability growth rate.

Simulations with such delays placed every 13 m (9 delays total) yield more than 11 TW peak power levels and nearly 10 TW average power with 120 m

undulator as shown in Figure 6.8 and summarized in Table 6.4. For an 8 fs electron beam 2 times longer than the 4 fs total slippage length, this simulated output power corresponds to  $\sim 10^{14}$  photons per pulse. Simulations with more frequent delays, also shown in Figure 6.8a, further reduce the sideband growth and produce average powers approaching that of time independent simulations.

## CHAPTER 7

### Conclusions

The results of the helical inverse free electron laser experimental program detailed in thesis for the first time demonstrate monoenergetic, high gradient, high energy gain acceleration of a large fraction of an electron beam injected into a laser-accelerator. These achievements suggest the IFEL as an excellent candidate for compact laser-based acceleration in the medium-to-high energy range. Energy gain larger than 50 MeV and 100 MeV/m average gradients exceeding those of conventional radio frequency accelerators were obtained using laser intensities of order  $10^{13}$  W/cm<sup>2</sup>—nearly five orders of magnitude lower than those used with LWFA experiments.

Additionally, we showed that the accelerator output energy may be controlled by varying the gap within the undulator. The high capture run demonstrated average accelerating gradients of 78 MeV/m competitive with high-gradient RF accelerators. Furthermore the accelerator achieved relatively low energy spread of less than 2% and about 1% output energy stability despite  $\sim 30\%$  laser energy fluctuations. The quality and stability of the resulting electron beam's longitudinal phase space compares very favorably with other advanced accelerator schemes, and may be improved with techniques for better phase space matching presented in Chapter 3. Moreover, the fraction captured may be greatly improved with the aid of a prebuncher, and simulations show that GeV electron beams may be achieved with a 100 TW CO<sub>2</sub> laser and a 1 m long helical undulator [87] at the future ATF2 facility [88]. Thus the achievements of the high capture run demon-

strate the promise of the IFEL as a useful accelerator and pave the way for future experiments.

The performance of the experiment and its recent predecessors relied on powerful CO<sub>2</sub> laser systems, yet since only a couple such lasers in the world are capable of such performance, future IFEL accelerators may use more commercially available high power radiation sources such as TiSa lasers. Recent experiments have indeed successfully used TiSa lasers to drive IFELs [64] and even demonstrate  $\sim 200$  MeV/m accelerating gradients [27]. Our studies in Chapter 3 suggest that GeV acceleration in a meter is achievable with 20 TW of 800 nm radiation, and we show through simulations that many schemes are possible for improving the capture and properties of the accelerated beam. Furthermore, we demonstrated via self consistent simulations of the radiation and particle dynamics that the IFEL accelerator may be designed to perform well even when heavily loaded and transfer up to 80% of the laser power to the electron beam with sufficient current. This shows that the IFEL is capable of high efficiencies in addition to high gradients and motivated the design of a dynamic undulator tapering code GITS to algorithmically design the undulator taper.

The potential for extremely high energy transfer efficiency suggested the possibility of efficiently producing radiation with strongly tapered undulators by essentially reversing the IFEL. This approach to radiation production which we refer to as tapering enhanced stimulated superradiant amplification (TESSA) in Chapter 6 is unique in that it pairs a tightly prebunched electron beam with a strongly focused seed laser as one would do in the design of an IFEL to decelerate electrons with gradients far exceeding those of FELs. Using this IFEL deceleration approach to radiation generation offers the capability of producing lasers of far higher efficiencies and average and peak powers than existing 4<sup>th</sup> generation light sources. Maintaining high conversion efficiencies from wall to e-beam to radiation may allow the production of ultra high average power visible light sources with a

wide range of applications including fusion science, defense and optically-driven accelerators for high luminosity colliders [20]. Application of TESSA to 13.5 nm radiation production could enable nearly 50% single-pass electro-optical energy conversion which in turn may be used to address the challenges of EUV lithography currently faced by the semiconductor industry. Applying the TESSA design principles to 1  $\mu\text{m}$  light generation, which the atmosphere is nearly transparent to, offers highly efficient power beaming to Earth's satellites, which may enable the aerospace industry to beat the limits imposed by the Tsiolkovsky rocket equation.

Finally, we applied the GITS tapering code to the challenge of maximizing x-ray production at future FEL facilities. Since the decelerating gradients are reduced by the  $1/\gamma$  dependence of the ponderomotive force, the undulator must be made many synchrotron oscillations long for significant power production, giving radiation sidebands time to grow which ultimately halt power production. We show that these sidebands may be suppressed by introducing periodic phase delays. Resulting simulations suggest the possibility of 10 TW power extraction (nearly 20% of the beam power) from a 4 kA, 14.35 GeV electron beam in 120 m. Such radiation could be useful for single-shot diffraction measurements. Improvements in x-ray mirrors may allow focusing high power x-ray lasers, thereby increasing accelerating gradients and achieving even larger efficiencies. Since the laser emittance decreases with decreasing wavelength, x-rays may in principle be focused to much smaller areas than near infrared lasers so production of increasingly large x-ray laser powers could one day help push the frontiers of extremely high field physics.

# APPENDIX A

## Laser accelerator energy fluctuations

Compared to other laser-driven advanced accelerators, the IFEL has an advantage in terms of achievable gradient for a given laser intensity. The rate of change in energy for an IFEL is proportional to the product of the laser and undulator normalized vector potential amplitudes defined as the momentum carried by each field divided by  $mc$  and given by  $K_1 = eA_1/mc = eE_1/kmc^2$  and  $K = eA_w/mc = eB_w/k_w mc$  where  $E_1$  and  $B_w$  are the laser electric and undulator magnetic field amplitudes, and  $k$  and  $k_w$  are the laser and undulator wavenumbers. We make the assumption that  $K_1 \ll K$  which is typical for existing IFELs. Since the undulator parameter  $K$  can be easily made larger than unity using few-cm long periods and 0.5 T-level fields, impressive gradients can be sustained even at non-relativistic laser intensities. To draw a comparison, laser wake field accelerators (LWFA) present a characteristic dependence of the accelerating wave amplitude as  $K_1^2$  and have only demonstrated significant energy gain with relativistic (i.e.  $K_1 > 1$ ) laser intensities [20].

The IFEL's reduced reliance on laser intensity becomes even more attractive considering the effect of fluctuations of laser parameters on accelerator performance. Laser driven accelerators either accelerate via direct coupling of the laser electric fields to the injected particles' velocities or via a ponderomotive interaction whereby a field-induced transverse motion couples to the laser's transverse fields. The former requires abruptly extracting the electrons from the laser field after a short interaction distance about  $\gamma^2\lambda$  before dephasing (here,  $\gamma$  is the par-

ticle energy and  $\lambda$  is the laser wavelength) [89] or slowing the phase velocity of light in a gas (inverse Cherenkov acceleration), optical fiber. Each of these has corresponding drawbacks or complications making them unattractive: damaged optics, low laser ionization thresholds, and induced wakefields. Dielectric laser accelerators directly couple the laser's electric field to the longitudinal motion of the electrons by propagating lasers through dielectric structures perpendicular to the electron motion, but present challenging limits on beam charge and emittance as the apertures of these structures tend to be roughly the size of the laser wavelength.

The nonlinear laser ponderomotive force depends on the square of the laser field  $F \sim \frac{1}{\gamma} \nabla E_1^2$  resulting from the interaction of the fast laser-induced transverse motion  $v_\perp \sim E_1/\gamma$  with the laser electric field. The force's dependence on the laser intensity  $E_1^2$  necessitates large peak intensities and results in a one-to-one dependence of driving force variations on input intensity fluctuations  $\delta F/F = \delta I_0/I_0$ ; if the input laser intensity fluctuates by 10%, the accelerated particle energy does too. Time of arrival and pointing jitter only exacerbates this problem. This ponderomotive force may be used to drive wakes in plasma for plasma wakefield acceleration resulting in net energy gains linearly varying by the intensity divided by the plasma density  $\gamma_f \sim E_1^2/n_0$  [20]. The use of the wakes circumvents the undesirable  $1/\gamma$  suppression in the ponderomotive force, but at the expense of substantially increased output energy fluctuations due to the addition of significant plasma density fluctuations  $\delta\gamma_f/\gamma_f = \sqrt{(\delta I_0/I_0)^2 + (\delta n_0/n_0)^2}$ . Consequentially, typical shot to variations in output parameters for laser wake field accelerators are 1-5% for energy, 1-10% for relative energy spread, and 5-50% for charge despite their impressive accomplishments [21]. Laser beat wave acceleration utilizes two lasers with appropriate focusing to control the ponderomotive phase [89]. Assuming that the lasers are synchronized but with similar but uncorrelated intensity fluctuations, the resulting force is expected to fluctuate by  $\delta F/F = \frac{1}{\sqrt{2}} \delta I_0/I_0$ .

Fluctuations in input laser parameters are a critical limiting factor in laser driven particle accelerators, and until they are made about as stable as klystrons, laser accelerators will remain less stable than conventional RF accelerators.

<b>Accelerator</b>	<b>Energy fluctuations <math>\delta\gamma/\gamma</math></b>
Direct laser	$\frac{1}{2} \delta I_0/I_0$
Dielectric laser	$\frac{1}{2} \delta I_0/I_0$
Pondermotive	$\delta I_0/I_0$
LWFA	$\sqrt{(\delta I_0/I_0)^2 + (\delta n_0/n_0)^2}$
Beat wave	$\frac{1}{\sqrt{2}} \delta I_0/I_0$
IFEL	$< 2\sqrt{(\cos \psi_r + (1 - \pi/2 \psi_r )\psi_r \sin \psi_r)K_l K/(1 + K^2)}$

Table A.1: Laser accelerator stability characteristics

The IFEL accelerating gradient is on par with the direct laser accelerators as the most immune to laser fluctuations. It accomplishes this feat by essentially replacing one of the lasers in the beat wave accelerator scheme with a static undulator magnetic field, yielding a force linearly proportional to the laser field  $F \propto E_l$ . This force yields fluctuations of  $\delta F/F = \frac{1}{2}\delta I_0/I_0$  which are 30% less than laser beat wave accelerators and better than 50% less than LWFA. Furthermore since the ponderomotive phase velocity does not involve the laser amplitude, the IFEL output energy is largely immune to laser fluctuations. At worst, it may slosh around within the relative resonant energy bandwidth  $|\eta_{\text{sep}}(\psi_r = -\pi/4)| < 0.78\sqrt{K_l K/(1 + K^2)}$  if injected slightly off resonance (see Equation 2.35). In our experiment, the energy of the accelerated beam varied by a mere 1.3% rms while the laser power fluctuated by 27% (see Section 5.4).

The IFEL may be designed to accommodate laser parameter tolerances in order to accelerate any desired fraction of input beam to a fixed final energy producing beams with relative energy spreads scaling as  $\sigma_\gamma/\gamma \sim \sqrt{E_l}$  which varies with laser intensity fluctuations as  $\delta\sigma_\gamma/\sigma_\gamma = \frac{1}{4}\delta I_0/I_0$ . With insignificant final energy

fluctuations and very modest  $\frac{1}{4}\delta I_0/I_0$  energy spread fluctuations, the IFEL is the most stable laser accelerator capable of significant energy gain for conventional electron beams.

## APPENDIX B

### IFEL simulation tools

Several simulation programs are useful in the design of an IFEL accelerator, and the ones we will use are listed in Table B. The undulator taper design calculated from the tapering equations and design parameters is a good starting point since it determines properties such as the resonant energy and ponderomotive bucket dimensions. Still, particles slightly detuned from resonance may not maintain their quasi-resonance if the acceleration is violent—that is, if the resonant energy changes significantly within one synchrotron period. In order to assess their behavior, it is useful to solve the 1D equations of motion for a collection of particles with the designed undulator taper. The combination of taper design and 1D simulations provide quick estimates of the accelerator performance for a given parameter set and enable studies of the effects of varying the input parameters in order to optimize the design.

<b>Code</b>	<b>Longitudinal dynamics</b>	<b>Transverse dynamics</b>	<b>Radiation feedback</b>
1D equations	Yes	No	No
Genesis	Yes	Approximate	Yes
Tredi	Yes	Yes	No
GPT	Yes	Yes	No

Table B.1: Capabilities of various IFEL simulation tools

The 1D simulations aid fast prototyping but ignore two important effects: the transverse dependence in the accelerator dynamics and the evolution of the radi-

ation field. In this case, the well known FEL simulation code Genesis 1.3 [48], is useful for studying these effects on accelerator performance. The code simulates the particle motion in three dimensions and solves the radiation evolution on a transverse grid. This is useful for studying the effects of beam loading on the accelerator's performance when electrons absorb a significant fraction of energy from the laser, a topic which will be discussed in detail later in this chapter. For computational efficiency, Genesis calculates the longitudinal motion by solving the FEL period averaged equations of motion, glossing over the fast oscillations resulting from the direct action of the laser on the particles which generally averages to zero in standard FEL and IFEL interactions [59]. Despite this approximation, Genesis is well suited for modeling the FEL interaction and has been used to guide the design of successful FEL experiments such as the LCLS [61, 60].

Since Genesis does not allow for arbitrary period tapering, we chained together Genesis simulations for each undulator period using the measured period and  $K$  parameter from measurements [62]. As an insurance policy for this unorthodox approach, we verified that the results of our IFEL simulations agreed with Tredi, a code successfully used in the design of the Neptune IFEL experiment [24]. The use of the period averaged equations limits Genesis' applicability in certain situations. Since the transverse dynamics of FELs are nearly completely determined by the undulator field, the transverse motion is calculated by applying an undulator transport matrix to the electron beam parameters. Consequently, Genesis cannot simulate electron trajectories in an optical deflector mode using a  $TEM_{10}$  such as [30]. Another consequence is that it can only approximate intraperiod undulator field modulations from strong tapering as constant or linearly or quadratically increasing. A magnetic field map is needed to better account for these effects.

The particle tracking code General Particle Tracer (GPT) [66] is useful for more accurately modeling the transverse particle dynamics. GPT solves the particle trajectories in three dimensions using the Lorentz force equations. The fields are

specified either by functions within modules or imported field maps. An immediate benefit to supporting functional field definitions is the ability to model laser fields with various transverse modes such as  $\text{TEM}_{10}$ . 3D undulator field maps generated with a magnetostatic code Radia [57] and imported to GPT offer an even closer approximation to realistic transverse dynamics including focusing. When first modeling IFELs with GPT, we found agreement between GPT and another 3D simulation code, Tredi [63], which was previously bench-marked against IFEL experimental results in planar undulators [24]. Furthermore, GPT has now been shown useful for modeling both the Rubicon IFEL as well as a 800 nm laser driven IFEL experiment at the Lawrence Livermore National Laboratory [27]. With this complete suite of simulation tools we can realistically model the experiment.

## APPENDIX C

### Laser induced emittance growth

Up until now, we have investigated the particle dynamics within a combination of undulator and laser fields. When electrons interact with intense lasers, non-linear effects may occur. We therefore, investigate the effect of a laser field on a copropagating electron beam.

Consider a free electron with energy  $\gamma mc^2$  copropagating with a linearly  $y$ -polarized planar EM-wave. We opt for a plane wave rather than a Gaussian pulse to simplify the dynamics. The Hamiltonian for the system is given by the invariant magnitude of the four-momentum vector.

$$\begin{aligned} (H - q\Phi)^2 - (\vec{p} - q\vec{A})^2 c^2 &= m^2 c^4 \\ \Rightarrow H &= \sqrt{(\vec{p} - q\vec{A})^2 c^2 + m^2 c^4} + q\Phi \end{aligned} \tag{C.1}$$

Here, the externally applied electrostatic potential  $\Phi$  is zero while the vector potential supplied by the plane wave is given by

$$\vec{A} = \hat{x} \frac{E_0}{ck} \sin k\zeta \tag{C.2}$$

where  $\zeta \equiv z - ct$ ,  $k$  is the laser wavenumber, and  $E_0$  is the laser electric field. The mechanical momentum can be found by taking the partial with respect to the canonical momentum. For the time component, this yields the result that the Hamiltonian equals the total particle energy:  $H = \gamma mc^2$ . For the spatial components, we have

$$\begin{aligned}
\frac{d\vec{x}}{dt} &= \frac{\partial H}{\partial \vec{p}} = \frac{\vec{p} - q\vec{A}}{\gamma m} \\
\Rightarrow \gamma m \dot{\vec{x}} &= \vec{p} - \hat{x} \frac{qE_0}{ck} \sin k\zeta \\
\Rightarrow &\begin{cases} \gamma m \dot{x} = p_x - \text{sgn}(q) mcK_l \sin k\zeta \\ \gamma m \dot{y} = p_y \\ \gamma m \dot{z} = p_z \end{cases} \tag{C.3}
\end{aligned}$$

Here, as before with the IFEL treatment, we define the normalized laser vector potential amplitude as  $K_l = |q|E_0/mc^2k$ . We now have to determine the evolution of the particle's  $z$ ,  $\gamma$ , and  $p_x$  coordinates to make sense of the evolution of  $x$ . We will assume that particles are uniformly distributed over the initial position  $z_0$ .

First, let's examine the evolution of  $p_x$ . The absence of the  $x$  and  $y$  coordinates in the Hamiltonian implies that the canonical momentum conjugate to those coordinates is conserved. Since  $dp_x/dt = 0$ , we can determine  $p_x$  by requiring that the initial normalized velocity be equal to  $x'_0$  at  $t = 0$  and  $z = z(t = 0) \equiv z_0$ .

$$\begin{aligned}
x'_0 &= \frac{p_x}{\gamma mc} - \text{sgn}(q) \frac{K_l}{\gamma} \sin k\zeta \\
\Rightarrow x' &= x'_0 - \text{sgn}(q) \frac{K_l}{\gamma} (\sin k\zeta - \sin kz_0) \tag{C.4}
\end{aligned}$$

Recall the definition of the longitudinal coordinate  $\zeta = \Delta z(t) + z_0 - ct$ . Using Equation C.3, the time dependence of  $\zeta$  can be determined using  $\Delta z(t) = \int_0^t dp_z/\gamma m$ . The time evolution of  $p_z$  is given by the variation in the Hamiltonian with respect to  $z$ .

$$\begin{aligned}
\frac{dp_z}{dt} &= -\frac{\partial H}{\partial z} = q \frac{\vec{p} - q\vec{A}}{\gamma m} \cdot \frac{\partial \vec{A}}{\partial z} \\
&= \frac{p_x - \text{sgn}(q) mcK_l \sin k\zeta}{\gamma m} \cdot \frac{qE_0}{c} \cos k\zeta \\
&= \text{sgn}(q) x'_0 mc^2 k K_l \cos k\zeta + \frac{kmc^2 K_l^2}{\gamma} \left( \sin(kz_0) \cos(k\zeta) - \frac{1}{2} \sin 2k\zeta \right) \tag{C.5}
\end{aligned}$$

For sub-relativistic laser fields such as that used in the Rubicon IFEL experiment where  $K \ll 1$ , these terms are largely ignorable since the relative laser-induced momentum fluctuations within one period of oscillation  $|\Delta p|/k p_z \approx x'_0 K_l/\gamma$  are incredibly small. Since the longitudinal velocity is constant and close to  $c$ , we can approximate  $v_z - c \approx -c/2\gamma^2$  in the phase evolution of the wave  $k\zeta \approx kz_0 - k'ct$  where we've defined  $k' \equiv k/2\gamma^2$ . Since the energy is  $\gamma mc^2 \approx p_z c$  to a good approximation, it too is relatively constant. Integrating the transverse velocity in Equation C.4 and requiring that  $x = x_0$  at  $t = 0$  yields the position as a function of  $z$ .

$$x = x_0 + x'_0 ct + \text{sgn}(q) \frac{K_l}{k'\gamma} (\cos kz_0 - \cos(k'ct - kz_0) + ck't \sin kz_0) \quad (\text{C.6})$$

In order to calculate the normalized emittance, we need the variance in  $x$  and its normalized velocity  $x'$ . Squaring each of these terms and averaging over these initial coordinates yields expressions for each. We will assume that the initial coordinates  $x_0$  and  $z_0$  and the velocity  $x'_0$  each average to zero while the energy averages to  $\gamma$ .

$$\epsilon_{x,n} = \gamma \sqrt{\sigma_x^2 \sigma_{x'}^2 - \sigma_{x,x'}^2} \quad (\text{C.7a})$$

$$\sigma_x^2 = \sigma_{x,0}^2 + 2ct \sigma_{xx',0} + (ct)^2 \sigma_{x',0}^2 + \frac{K_l^2}{k'^2 \gamma^2} \left( 1 + \frac{1}{2} (k'ct)^2 - \cos k'ct - k'ct \sin k'ct \right) \quad (\text{C.7b})$$

$$\sigma_{x'}^2 = \sigma_{x',0}^2 + \frac{K_l^2}{\gamma^2} (1 - \cos k'ct) \quad (\text{C.7c})$$

$$\sigma_{xx'} = \sigma_{xx',0} + ct \left( \sigma_{x',0}^2 + \frac{K_l^2}{2\gamma^2} (1 - \cos k'ct) \right) \quad (\text{C.7d})$$

The first thing to note is that there are two harmonic frequencies:  $k'$  and  $2k'$ . In addition to harmonic components there are terms linear and others quadratic in time which cause irreversible emittance growth. The growth itself comes from

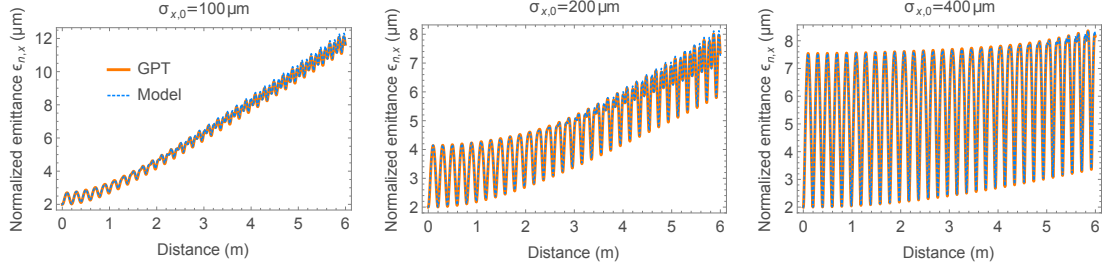


Figure C.1: Laser heater model and GPT simulations for three different beam waists: 100, 200, and 400  $\mu\text{m}$ .

the random initial positions of the particles which are born in the laser field. In experiments with intense lasers where electrons are swiftly kicked into a laser field, this emittance growth may become significant and irreversible if enough coaxial propagation is allowed. Another point is that the sign of the charge dropped out in Equation C.7 so positrons may be expected to behave in the same way.

In order to investigate the validity of the model, we compared prediction with GPT, introduced at the beginning of this chapter. We used a functional form of the plane wave laser field with a wavelength of 10.3  $\mu\text{m}$  and a peak field strength 4 GV/m. The 50 MeV beam is started from a waist of 200  $\mu\text{m}$  with a 2  $\mu\text{m}$  normalized emittance and allowed to propagate 6 m.

Figure C.1 shows the normalized emittance as a function of position. The model and simulation are in reasonable agreement for these parameters. As predicted, there are two oscillation frequencies. The first has a period of 19.7 cm as predicted by  $\lambda' = 2\gamma^2\lambda$  while the second is half that. Larger spreads in angles associated with smaller beam waists for constant emittance clearly increase the irreversible emittance growth rate. On the other hand, keeping the beam large so that the angular spread is small keeps the irreversible emittance growth small but increases the emittance oscillation amplitude. This suggests that emittance growth can be mitigated somewhat during injection to and extraction from the laser and expanding during copropagation with the laser. There are clear minima

of the oscillations where if the beam is extracted, which would could reduce some of the emittance growth. Since the emittance oscillation periods scale with energy, after acceleration the increased period may allow easier extraction.

While the discussion has been limited to a linearly polarized plane wave laser, the results are somewhat general. For example, a circularly polarized laser can be treated as two orthogonally polarized lasers. Since the motion in the plane perpendicular to the polarization is unaffected by the laser, the analysis for the emittance growth in each planes is independent. The difference with respect to a fundamental Gaussian mode laser is primarily the transverse field strength variation and a variation in the laser phase from the Guoy phase shift on-axis and due to the curved phase fronts off-axis. Nevertheless, the plane wave may be a reasonable approximation in many cases of interest. Understanding these contributions to the electron beam's emittance growth can assist in out understanding of limitations on laser accelerator accelerators and guide experimental design.

## REFERENCES

- [1] Walter Henning, Charles Shank, et al. Accelerators for Americas future. *Department of Energys Office of Science*, 2010.
- [2] Keith A Olive, Particle Data Group, et al. Review of particle physics. *Chinese Physics C*, 38(9):090001, 2014.
- [3] J T Seeman. The stanford linear collider. *Annual Review of Nuclear and Particle Science*, 41(1):389–428, 1991.
- [4] Kurt Hbner. Designing and building {LEP}. *Physics Reports*, 403404(0):177 – 188, 2004. {CERN} - the second 25 years.
- [5] Robert Rathbun Wilson. The Tevatron. *Phys.Today*, 30N10:23–30, 1977.
- [6] Lyndon Evans and Philip Bryant. Lhc machine. *Journal of Instrumentation*, 3(08):S08001, 2008.
- [7] Donald H Bilderback, Pascal Elleaume, and Edgar Weckert. Review of third and next generation synchrotron light sources. *Journal of Physics B: Atomic, Molecular and Optical Physics*, 38(9):S773, 2005.
- [8] John MJ Madey. Stimulated emission of bremsstrahlung in a periodic magnetic field. *Journal of Applied Physics*, 42(5):1906–1913, 1971.
- [9] R. Bonifacio, C. Pellegrini, and L.M. Narducci. Collective instabilities and high-gain regime in a free electron laser. *Optics Communications*, 50(6):373 – 378, 1984.
- [10] Brian WJ McNeil and Neil R Thompson. X-ray free-electron lasers. *Nature photonics*, 4(12):814–821, 2010.
- [11] Emma P., Akre R., Arthur J., Bionta R., Bostedt C., Bozek J., Brachmann A., Bucksbaum P., Coffee R., Decker F.-J., Ding Y., Dowell D., Edstrom S., Fisher A., Frisch J., Gilevich S., Hastings J., Hays G., Hering Ph., Huang Z., Iverson R., Loos H., Messerschmidt M., Miahnahri A., Moeller S., Nuhn H.-D., Pile G., Ratner D., Rzepiela J., Schultz D., Smith T., Stefan P., Tompkins H., Turner J., Welch J., White W., Wu J., Yocky G., and Galayda J. First lasing and operation of an angstrom-wavelength free-electron laser. *Nature Photonics*, 4(9):641 – 647, 2010.
- [12] Tetsuya Ishikawa, Hideki Aoyagi, Takao Asaka, Yoshihiro Asano, Noriyoshi Azumi, Teruhiko Bizen, Hiroyasu Ego, Kenji Fukami, Toru Fukui, Yukito Furukawa, et al. A compact x-ray free-electron laser emitting in the sub-angstrom region. *Nature Photonics*, 6(8):540–544, 2012.

- [13] Robert B. Palmer. Interaction of relativistic particles and free electromagnetic waves in the presence of a static helical magnet. *Journal of Applied Physics*, 43(7):3014–3023, 1972.
- [14] E. D. Courant, C. Pellegrini, and W. Zakowicz. High-energy inverse free-electron-laser accelerator. *Phys. Rev. A*, 32:2813–2823, Nov 1985.
- [15] WD Kimura, P Musumeci, DC Quimby, SC Gottschalk, and C Pellegrini. Conceptual design for a 1-gev ifel accelerator. *Advanced Accelerator Concepts*, 737:251–257, 2004.
- [16] P Musumeci. Inverse free electron laser acceleration for advanced light sources. In *Proc. 2006 FEL Conference, Berlin, Germany*, 2006.
- [17] J. P. Duris, P. Musumeci, and R. K. Li. Inverse free electron laser accelerator for advanced light sources. *Phys. Rev. ST Accel. Beams*, 15:061301, Jun 2012.
- [18] P. Sprangle, A. Ting, E. Esarey, and A. Fisher. Tunable, short pulse hard xrays from a compact laser synchrotron source. *Journal of Applied Physics*, 72(11):5032–5038, 1992.
- [19] Alexander Wu Chao. *Physics of collective beam instabilities in high energy accelerators*. Wiley, 1993.
- [20] E. Esarey, C. B. Schroeder, and W. P. Leemans. Physics of laser-driven plasma-based electron accelerators. *Rev. Mod. Phys.*, 81:1229–1285, Aug 2009.
- [21] Simon Martin Hooker. Developments in laser-driven plasma accelerators. *Nature Photonics*, 7(10):775–782, 2013.
- [22] Iddo Wernick and TC Marshall. Experimental test of the inverse free-electron-laser accelerator principle. *Physical Review A*, 46(6):3566, 1992.
- [23] W. D. Kimura, M. Babzien, I. Ben-Zvi, L. P. Campbell, D. B. Cline, C. E. Dille, J. C. Gallardo, S. C. Gottschalk, K. P. Kusche, R. H. Pantell, I. V. Pogorelsky, D. C. Quimby, J. Skaritka, L. C. Steinhauer, V. Yakimenko, and F. Zhou. Demonstration of high-trapping efficiency and narrow energy spread in a laser-driven accelerator. *Phys. Rev. Lett.*, 92:054801, Feb 2004.
- [24] P. Musumeci, S. Ya. Tochitsky, S. Boucher, C. E. Clayton, A. Doyuran, R. J. England, C. Joshi, C. Pellegrini, J. E. Ralph, J. B. Rosenzweig, C. Sung, S. Tolmachev, G. Travish, A. A. Varfolomeev, A. A. Varfolomeev, T. Yarovoi, and R. B. Yoder. High energy gain of trapped electrons in a tapered, diffraction-dominated inverse-free-electron laser. *Phys. Rev. Lett.*, 94:154801, Apr 2005.

- [25] P. Musumeci, C. Pellegrini, and J. B. Rosenzweig. Higher harmonic inverse free-electron laser interaction. *Phys. Rev. E*, 72:016501, Jul 2005.
- [26] Pietro Musumeci. *Acceleration of electrons by inverse free electron laser interaction*. PhD thesis, University of California, Los Angeles, 2004.
- [27] Joshua Moody. *Inverse Free Electron Laser Interactions with Sub-Picosecond High Brightness Electron Beams*. PhD thesis, University of California, Los Angeles, 2014.
- [28] Norman M Kroll, Philip L Morton, and Marshall N Rosenbluth. Free-electron lasers with variable parameter wigglers. *Quantum Electronics, IEEE Journal of*, 17(8):1436–1468, 1981.
- [29] Erik Hemsing. *Generation and Amplification of Coherent Radiation with Optical Orbital Angular Momentum in a Free-Electron Laser*. PhD thesis, University of California, Los Angeles, 2011.
- [30] G. Andonian, E. Hemsing, D. Xiang, P. Musumeci, A. Murokh, S. Tochitsky, and J. B. Rosenzweig. Longitudinal profile diagnostic scheme with subfemtosecond resolution for high-brightness electron beams. *Phys. Rev. ST Accel. Beams*, 14:072802, Jul 2011.
- [31] F. Ciocci, G. Dattoli, L. Giannessi, C. Mari, and A. Torre. Optical properties of helical undulators. *Nuclear Instruments and Methods in Physics Research Section B: Beam Interactions with Materials and Atoms*, 63(3):319 – 325, 1992.
- [32] Jamie Rosenzweig. *Fundamentals of beam physics*. Oxford University Press England, 2003.
- [33] Erik Hemsing and Dao Xiang. Cascaded modulator-chicane modules for optical manipulation of relativistic electron beams. *Physical Review Special Topics-Accelerators and Beams*, 16(1):010706, 2013.
- [34] James A Clarke. *The science and technology of undulators and wigglers*. Oxford series on synchrotron radiation. Oxford Univ. Press, Oxford, 2004.
- [35] W. Zakowicz. *Journal of Applied Physics*, 55(3421), 1984.
- [36] R. Tikhoplav et al. *Proceedings of the 8th European Particle Accelerator Conference, Paris, France, 2002*.
- [37] B. Debord, M. Alharbi, L. Vincetti, A. Husakou, C. Fourcade-Dutin, C. Hoenninger, E. Mottay, F. Gérôme, and F. Benabid. Multi-meter fiber-delivery and pulse self-compression of milli-joule femtosecond laser and fiber-aided laser-micromachining. *Opt. Express*, 22(9):10735–10746, May 2014.

- [38] D. J. Richardson, J. Nilsson, and W. A. Clarkson. High power fiber lasers: current status and future perspectives. *J. Opt. Soc. Am. B*, 27(11):B63–B92, Nov 2010.
- [39] M.N. Zervas and C.A. Codemard. High power fiber lasers: A review. *Selected Topics in Quantum Electronics, IEEE Journal of*, 20(5):219–241, Sept 2014.
- [40] A. van Steenbergen, J. Gallardo, J. Sandweiss, and J.-M. Fang. Observation of energy gain at the bnl inverse free-electron-laser accelerator. *Phys. Rev. Lett.*, 77:2690–2693, Sep 1996.
- [41] Amplitude Technologies. 2-4 rue du bois chaland, ce 2926, 91029 evry, france. <http://www.amplitudetechnologies.com/>.
- [42] F. H. O’Shea, G. Marcus, J. B. Rosenzweig, M. Scheer, J. Bahrtdt, R. Weingartner, A. Gaupp, and F. Grüner. Short period, high field cryogenic undulator for extreme performance x-ray free electron lasers. *Phys. Rev. ST Accel. Beams*, 13:070702, Jul 2010.
- [43] K.Uestuener et al. *Proceedings of the 20th Workshop on Rare Earth Permanent Magnets and Applications, Knossos, Greece*, 2008.
- [44] A Mikhailichenko and T Moore. First test of short period helical sc undulator prototype. *Cornell CBN*, pages 02–6, 2002.
- [45] FH OShea, G Marcus, JB Rosenzweig, M Scheer, J Bahrtdt, R Weingartner, A Gaupp, and F Grüner. Short period, high field cryogenic undulator for extreme performance x-ray free electron lasers. *Physical Review Special Topics-Accelerators and Beams*, 13(7):070702, 2010.
- [46] Jere Harrison, Abhijeet Joshi, Jonathan Lake, Rob Candler, and Pietro Musumeci. Surface-micromachined magnetic undulator with period length between 10  $\mu\text{m}$  and 1 mm for advanced light sources. *Phys. Rev. ST Accel. Beams*, 15:070703, Jul 2012.
- [47] B.A. Peterson, O.D. Oniku, W.C. Patterson, D. Le Roy, A. Garraud, F. Herrault, N.M. Dempsey, D.P. Arnold, and M.G. Allen. Technology development for short-period magnetic undulators. *Physics Procedia*, 52(0):36 – 45, 2014. Proceedings of the workshop Physics and Applications of High Brightness Beams:Towards a Fifth Generation Light Source.
- [48] S. Reiche. {GENESIS} 1.3: a fully 3d time-dependent {FEL} simulation code. *Nuclear Instruments and Methods in Physics Research Section A: Accelerators, Spectrometers, Detectors and Associated Equipment*, 429(13):243 – 248, 1999.

- [49] A. Tremaine, S. Boucher, A. Murokh, S. Anderson, W. Brown, J. Duris, P. Musumeci, J. Rosenzweig, I. Jovanovic, I. Pogorelsky, M. Polyanskiy, and V. Yakimenko. Inverse free electron laser accelerators for driving compact light sources and detection applications. *Proceedings PAC 2011, on JACOW*, page MOOBN2, 2011.
- [50] Mikhail N Polyanskiy, Igor V Pogorelsky, and Vitaly Yakimenko. Picosecond pulse amplification in isotopic co<sub>j</sub> sub<sub>j</sub> 2<sub>i</sub>/sub<sub>j</sub> active medium. *Optics express*, 19(8):7717–7725, 2011.
- [51] Klaus Halbach. Permanent magnet undulators. *Le Journal de Physique Colloques*, 44(C1):C1–211, 1983.
- [52] Joseph Duris, P Musumeci, M Babzien, M Fedurin, K Kusche, RK Li, J Moody, I Pogorelsky, M Polyanskiy, JB Rosenzweig, et al. High-quality electron beams from a helical inverse free-electron laser accelerator. *Nature communications*, 5, 2014.
- [53] E. Hemsing, A. Knyazik, F. OShea, A. Marinelli, P. Musumeci, O. Williams, S. Tochitsky, and J. B. Rosenzweig. Experimental observation of helical microbunching of a relativistic electron beam. *Applied Physics Letters*, 100(9):–, 2012.
- [54] Erik Hemsing, Andrey Knyazik, Michael Dunning, Dao Xiang, Agostino Marinelli, Carsten Hast, and James B Rosenzweig. Coherent optical vortices from relativistic electron beams. *Nature Physics*, 9(9):549–553, 2013.
- [55] Loctite Corporation USA. *Product Description Sheet, Hysol Product 608*, 8 2001.
- [56] T. Bizen, Y. Asano, T. Hara, X. Marechal, T. Seike, T. Tanaka, H. Kitamura, H. S. Lee, D. E. Kim, and C. W. Chung. Improvement of radiation resistance of ndfeb magnets by thermal treatment. *AIP Conference Proceedings*, 705(1):171–174, 2004.
- [57] Oleg Chubar, Pascal Elleaume, and Joel Chavanne. A three-dimensional magnetostatics computer code for insertion devices. *Journal of synchrotron radiation*, 5(3):481–484, 1998.
- [58] S Reiche, P Musumeci, and K Goldammer. Recent upgrade to the free-electron laser code genesis 1.3. *Proceedings PAC 2007, on JACOW*, pages 1269–12712007, 2007.
- [59] Sven Reiche. *Numerical Studies for a Single Pass High Gain Free-Electron Laser*. PhD thesis, University of Hamburg, 2004.

- [60] S. Reiche, C. Pellegrini, J. Rosenzweig, P. Emma, and P. Krejcik. Start-to-end simulation for the {LCLS} x-ray {FEL}. *Nuclear Instruments and Methods in Physics Research Section A: Accelerators, Spectrometers, Detectors and Associated Equipment*, 483(12):70 – 74, 2002. Proceedings of the 23rd International Free Electron Laser Conference and 8th {FEL} Users Workshop.
- [61] M. Borland, Y.C. Chae, P. Emma, J.W. Lewellen, V. Bharadwaj, W.M. Fawley, P. Krejcik, C. Limborg, S.V. Milton, H.-D. Nuhn, R. Soliday, and M. Woodley. Start-to-end simulation of self-amplified spontaneous emission free electron lasers from the gun through the undulator. *Nuclear Instruments and Methods in Physics Research Section A: Accelerators, Spectrometers, Detectors and Associated Equipment*, 483(12):268 – 272, 2002. Proceedings of the 23rd International Free Electron Laser Conference and 8th {FEL} Users Workshop.
- [62] J.P. Duris, R.K. Li, P. Musumeci, E.W. Threlkeld, and M.T. Westfall. High-gradient high-energy-gain inverse free electron laser experiment using a helical undulator. *Proceedings PAC 2011, on JACOW*, page MOP102, 2011.
- [63] L Giannessi, P Musumeci, and M Quattromini. Tredi: fully 3d beam dynamics simulation of {RF} guns, bendings and {FELs}. *Nuclear Instruments and Methods in Physics Research Section A: Accelerators, Spectrometers, Detectors and Associated Equipment*, 436(3):443 – 444, 1999.
- [64] Christopher MS Sears, Eric Colby, RJ England, Rasmus Ischebeck, Christopher McGuinness, Janice Nelson, Robert Noble, Robert H Siemann, James Spencer, Dieter Walz, et al. Phase stable net acceleration of electrons from a two-stage optical accelerator. *Physical Review Special Topics-Accelerators and Beams*, 11(10):101301, 2008.
- [65] Mike Dunning, E Hemsing, C Hast, TO Raubenheimer, S Weathersby, D Xiang, and F Fu. Demonstration of cascaded optical inverse free-electron laser accelerator. *Physical review letters*, 110(24):244801, 2013.
- [66] MJ De Loos and SB Van der Geer. General particle tracer: A new 3d code for accelerator and beamline design. In *5th European Particle Accelerator Conference*, page 1241, 1996.
- [67] Yusuke Sakai, Igor Pogorelsky, Mikhail Fedurin, Pietro Musumeci, Joseph Duris, Oliver Williams, and James Rosenzweig. 3rd order harmonic in inverse Compton scattering. In *CLEO: 2014*, page JTh3L.3. Optical Society of America, 2014.
- [68] Ilan Ben-Zvi. The bnl accelerator test facility and experimental program. Technical report, Brookhaven National Lab., Upton, NY (United States). Funding organization: USDOE, Washington, DC (United States), 1992.

- [69] TC Marshall. Experimental research on the laser cyclotron auto-resonance accelerator lacara. Technical report, Columbia University, 2008.
- [70] M. Borland. *ELEGANT: A flexible SDDS-compliant code for accelerator simulation*. Aug 2000.
- [71] Anthony E Siegman. Lasers university science books. *Mill Valley, CA*, 37, 1986.
- [72] P. B. Corkum, A. J. Alcock, and K. E. Leopold. Electron-beam-controlled transmission of 10-m radiation in semiconductors. *Journal of Applied Physics*, 50(5):3079–3082, 1979.
- [73] D. Cesar et al. Submitted to Journal of Applied Physics 2015.
- [74] M. N. Polyanskiy. Refractive index database. Available at <http://refractiveindex.info>. Accessed: Sept. 24 2015.
- [75] J. Duris, P. Musumeci, M. Babzien, S. Custodio, M. Fedurin, K. Kusche, R. K. Li, J. Moody, I. Pogorelsky, M. Polyanskiy, J. B. Rosenzweig, Y. Sakai, N. Sudar, C. Swinson, E. Threlkeld, O. Williams, and V. Yakimenko. Helical inverse free electron laser accelerator for efficient production of high quality electron beams. *Advanced Accelerator Concepts*, 2014.
- [76] Helmut Wiedemann. *Particle accelerator physics*, volume 1. Springer, 2003.
- [77] Avi Gover. Superradiant and stimulated-superradiant emission in pre-bunched electron-beam radiators. i. formulation. *Physical Review Special Topics-Accelerators and Beams*, 8(3):030701, 2005.
- [78] T. J. Orzechowski, B. R. Anderson, J. C. Clark, W. M. Fawley, A. C. Paul, D. Prosnitz, E. T. Scharlemann, S. M. Yarema, D. B. Hopkins, A. M. Sessler, and J. S. Wurtele. High-efficiency extraction of microwave radiation from a tapered-wiggler free-electron laser. *Phys. Rev. Lett.*, 57:2172–2175, Oct 1986.
- [79] Y. Jiao, J. Wu, Y. Cai, A. W. Chao, W. M. Fawley, J. Frisch, Z. Huang, H.-D. Nuhn, C. Pellegrini, and S. Reiche. Modeling and multidimensional optimization of a tapered free electron laser. *Phys. Rev. ST Accel. Beams*, 15:050704, May 2012.
- [80] C. Emma, J. Wu, K. Fang, S. Chen, S. Serkez, and C. Pellegrini. Terawatt x-ray free-electron-laser optimization by transverse electron distribution shaping. *Phys. Rev. ST Accel. Beams*, 17:110701, Nov 2014.
- [81] B. Hafizi, A. Ting, P. Sprangle, and C. M. Tang. Development of sidebands in tapered and untapered free-electron lasers. *Phys. Rev. A*, 38:197–203, Jul 1988.

- [82] P. Musumeci, J. Duris, and A. Murokh. US Patent (pending), 61/982623.
- [83] A Gover, E Dyunin, Y Lurie, Y Pinhasi, and MV Krongauz. Superradiant and stimulated-superradiant emission in prebunched electron-beam radiators. ii. radiation enhancement schemes. *Physical Review Special Topics-Accelerators and Beams*, 8(3):030702, 2005.
- [84] D Chapman, W Thomlinson, R E Johnston, D Washburn, E Pisano, N Gmr, Z Zhong, R Menk, F Arfelli, and D Sayers. Diffraction enhanced x-ray imaging. *Physics in Medicine and Biology*, 42(11):2015, 1997.
- [85] J Amann, W Berg, V Blank, F-J Decker, Y Ding, P Emma, Y Feng, J Frisch, D Fritz, J Hastings, et al. Demonstration of self-seeding in a hard-x-ray free-electron laser. *Nature photonics*, 6(10):693–698, 2012.
- [86] N. R. Thompson and B. W. J. McNeil. Mode locking in a free-electron laser amplifier. *Phys. Rev. Lett.*, 100:203901, May 2008.
- [87] P Musumeci and J Duris. GeV/m ifel at atf2, 2014.
- [88] I Pogorelsky. Review of atf ii upgrade plan and spectrum of science trusts, 2014.
- [89] Eric Esarey, Phillip Sprangle, and Jonathan Krall. Laser acceleration of electrons in vacuum. *Phys. Rev. E*, 52:5443–5453, Nov 1995.